

DISSERTATION

Modeling of Emerging Resistive Switching Based Memory Cells

ausgeführt zum Zwecke der Erlangung des akademischen Grades
eines Doktors der technischen Wissenschaften

eingereicht an der Technischen Universität Wien
Fakultät für Elektrotechnik und Informationstechnik
von

Alexander Makarov



Wien, im März 2014

Kurzfassung

Viele Jahrzehnte wurden ladungsbasierte Speichertechnologien (z.Bsp. DRAM, Flashspeicher etc.) erfolgreich verkleinert, um höhere Geschwindigkeit und größere Integrationsdichte bei gleichzeitig geringeren Kosten per Bit zu erzielen. Allerdings nähern sich Speicher, die ladungsbasiert sind, den physikalischen Grenzen der Skalierbarkeit. Im Gegensatz zu DRAM und Flashspeicher sollte ein zukünftiger universeller Speicher keine Speicherung elektrischer Ladung benötigen und auf alternativen Prinzipien zur Informationsspeicherung beruhen. Für den erfolgreichen Einsatz eines neuen universellen Speichers muss dieser auch eine niedrige Arbeitsspannung, geringen Energieverbrauch, hohe Arbeitsgeschwindigkeit, lange Speicherzeit, lange Lebensdauer und eine simple Struktur aufweisen. Alternative Prinzipien zur Informationsspeicherung umfassen den Widerstandswechseleffekt in Isolatoren, den magnetoresistiven Effekt, die Domänenwandbewegung in Racetrack-Speichern, den ferroelektrischen Effekt und weitere. Unter den Technologien, die diese neuen Speicherprinzipien verwenden, sind STT-MRAM und RRAM die vielversprechendsten Kandidaten für zukünftige universelle Speicher.

Hierbei erscheint die Uneinheitlichkeit der Bauteileigenschaften die größte Herausforderung bei der Herstellung von RRAM in grossem Maßstab zu sein. Um dieses Problem zu lösen, wird in erster Linie ein besseres Verständnis der Widerstandswechselphänomene benötigt. Die Entwicklung von genauen und flexiblen Schaltmodellen ist unverzichtbar für den zukünftigen Fortschritt in der RRAM-Technologie. In der Doktorarbeit wird ein neues stochastisches Modell des resistiven Schaltens präsentiert. Die mit dem stochastischen Modell erhaltenen Simulationsergebnisse decken sich gut mit den experimentellen Ergebnissen.

Hingegen stellt die größte Herausforderung für STT-MRAM die Reduktion der Schaltstromdichte dar, ohne den thermischen Stabilitätsfaktor zu verschlechtern. Mikromagnetische Simulationen tragen durch die Optimierung der STT-MRAM Speicherzellen erheblich dazu bei, dieses Problem für STT-MRAM zu lösen. In dieser Arbeit wird das neue Konzept einer STT-MRAM Struktur mit freier Kompositlage vorgeschlagen, simuliert und optimiert. Zusätzlich werden Zuverlässigkeitsprobleme studiert. Ein neuer Mechanismus für Schaltversagen eines MTJ-basierenden STT-MRAM durch die Formierung einer transversen Domänenwand in der freien Schicht wird präsentiert. Eine Methode wird gezeigt, um diesen parasitären Effekt für einen effizienten Spin-Torque-Oszillator zu nutzen. Mittels umfangreicher mikromagnetischer Modellierung kann gezeigt werden, dass diese Struktur über eine breite Abstimmbarkeit der Oszillationsfrequenz verfügt, beginnend mit ein paar GHz bis hin zu mehreren 10 GHz.

Abstract

For many decades charge-based memory (e.g. dynamic random access memory (DRAM), flash memory, etc.) technologies have been successfully scaled down to achieve higher speed and increased density of memory chips at lower bit cost. However, memories based on charge storage are gradually approaching the physical limits of scalability. Unlike DRAM and flash memories a future universal memory should not require electric charge storing and can be based on alternative principles of information storage. For the successful application a new universal memory must also exhibit low operating voltage, low power consumption, high operation speed, long retention time, high endurance, and a simple structure. Alternative principles of information storage include the resistive switching phenomenon in insulators, the effect of changing the magnetoresistance, the domain wall motion along magnetic racetracks, the ferroelectric effect, and others. From technologies which utilize new storage principles the most promising candidates for future universal memory are spin transfer torque MRAM (STT-MRAM) and resistive/redox RAM (RRAM).

Non-uniformity of device characteristics appears a major challenge for large-scale manufacturing of RRAM. First and foremost, one needs a better understanding of the resistive switching phenomena to solve this problem. Development of accurate and flexible models of switching is paramount for future progress in RRAM technology. In the thesis a new stochastic model of resistive switching is presented. Simulation results obtained with the stochastic model are in good agreement with experimental results.

For STT-MRAM the main challenge is to reduce the switching current density without compromising the thermal stability factor. Micromagnetic simulations significantly contribute to solving this problem through the optimization of STT-MRAM memory cells. In the thesis, a new concept of a STT-MRAM structure with a composite free layer is proposed, simulated, and optimized. In addition, reliability issues of STT-MRAM are studied. A new mechanism for switching failure in a MTJ-based STT-MRAM through transverse domain wall formation in a free layer is discovered. A method of utilizing this parasitic switching effect for constructing an efficient spin-torque oscillator is shown. By performing extensive micromagnetic modeling it is proved that the structure exhibits a wide tunability range of oscillation frequencies from a few GHz to several tens of GHz.

Аннотация

Технологии памяти, основанные на хранении заряда (например, динамическая память с произвольным доступом (DRAM), флэш-память и т.д.), успешно уменьшались в размерах на протяжении последних десятилетий, достигая более высокой скорости и плотности записи при сохранении низкой стоимости. Однако память на основе хранения заряда постепенно приближается к физическому пределу масштабирования. В отличие от DRAM и флэш-памяти, будущая универсальная память должна быть основана на альтернативных к зарядовому принципам хранения информации. Для успешного применения новая универсальная память должна обладать низким рабочим напряжением, низким энергопотреблением, высокой скоростью работы, долгим временем хранения информации, высокой надежностью и иметь простую структуру. К альтернативным принципам хранения информации относятся: феномен резистивного переключения в изоляторах, эффект изменения магнитосопротивления, движение доменной стенки вдоль ферромагнитных нанопроволок, сегнетоэлектрический эффект и другие. Из технологий, использующих новые принципы хранения информации, наиболее перспективными кандидатами для создания будущей универсальной памяти являются магниторезистивная память с передачей спинового вращательного момента (STT-MRAM) и резистивная/окислительно-восстановительная память (RRAM).

Главная проблема для массового производства RRAM – неравномерность ее характеристик. В первую очередь, для решения этой проблемы необходимо более глубокое понимание феномена резистивного переключения. Создание моделей, описывающих резистивное переключение, имеет первостепенное значение для будущего прогресса в технологии RRAM. В диссертации представлена новая стохастическая модель резистивного переключения. Результаты моделирования, полученные на основе этой модели, хорошо согласуются с экспериментальными результатами.

Для STT-MRAM основной задачей является уменьшение плотности тока переключения без ущерба для термической стабильности структуры. Микромагнитное моделирование вносит значительный вклад в решение этой проблемы за счет оптимизации структуры STT-MRAM ячеек. В диссертации предлагается новая структура STT-MRAM с составным свободным слоем, проводится ее моделирование и оптимизация. Кроме того, изучаются проблемы надежности STT-MRAM. В диссертации описан новый механизм отказа в переключении STT-MRAM, основанной на магнитном туннельном переходе (MTJ), через формирование поперечной доменной стенки в свободном слое. Продемонстрирован способ использования

этого паразитного эффекта для построения эффективного нано осциллятора на основе спин-вращательного момента. Используя микромагнитное моделирование, было показано, что структура имеет широкий диапазон перестройки частот колебаний от нескольких ГГц до нескольких десятков ГГц.

Acknowledgement

First and foremost, I would like to thank my supervisors Prof. Siegfried Selberherr and Privatdoz. Dr. Viktor Sverdlov for the opportunity to join the scientific group of the Institute for Microelectronics and introducing me to an interesting research area, where I was able to invent, develop, and implement my ideas.

Additional thanks to Privatdoz. Dr. Viktor Sverdlov for introducing me to microelectronics simulations and a very interesting course of lectures “Introduction to silicon spintronics”.

I am very grateful to all my co-authors and colleagues, in particular to Dr. Stanislav Tyaginov, Dr. Thomas Windbacher, Dr. Karl Rupp, Dr. Lado Filipovic and MSc. Dmitry Osintsev.

To all my family, and my parents, who always support me in any of my undertaking.

Contents

Kurzfassung	ii
Abstract	iii
Аннотация	iv
Acknowledgement	vi
Contents	vii
List of Abbreviations	x
List of Symbols	xi
1 Introduction	1
1.1 Charge-based Memory Technology	1
1.2 Outline of the Thesis	3
2 Resistive Change Based Memory	4
2.1 RRAM Basics	4
2.1.1 Resistive-switchable oxides	5
2.1.2 Unipolar and bipolar behavior	5
2.1.3 Challenges of the RRAM	7
2.2 Mechanisms and Models of Resistive Switching	7
2.2.1 First attempts of explanation and early models	7
2.2.2 Current research progress	10
2.3 Conclusions	15
3 Stochastic Model of the Resistive Switching	16
3.1 Switching Mechanism	16
3.2 Model Systems Description	17
3.3 Electron Hopping and Ion Motion	17
3.4 Applications of Stochastic Based Method	20
3.4.1 Electron motion simulation	20
3.4.2 Modeling of the SET/RESET process	24
3.4.3 Hysteresis cycle modeling	27

4	Magnetoresistive Memory	29
4.1	MRAM and STT-MRAM Basics	29
4.1.1	Magnetoresistance phenomenon	30
4.1.2	Magnetic pillar switching	33
4.2	In-Plane and Perpendicular Free Layer Magnetization	34
4.2.1	Thermal stability factor	35
4.2.2	Switching current	36
4.3	Magnetic Cell Architecture	37
4.3.1	Single MTJ with one tunnel barrier	37
4.3.2	Dual MTJ with two barriers and ultra-thin dual MTJ cell	38
4.3.3	Cell utilizing thermally assisted switching mechanism	38
4.3.4	Cell utilizing precessional switching mechanism	39
4.3.5	Three-terminal MTJ cell	39
4.4	Conclusions	40
5	Macro- and Micromagnetic Approach	41
5.1	Landau-Lifshitz-Gilbert Equation	41
5.2	Landau-Lifshitz-Gilbert-Slonczewski Equation	43
5.2.1	Single reference layer structure	43
5.2.2	Two reference layers structure	44
5.3	Effective Magnetic Field	46
5.3.1	Exchange field	46
5.3.2	Anisotropy field	47
5.3.3	Demagnetization and magnetostatic field	48
5.3.4	Ampere field	50
5.3.5	Thermal field	50
6	Numerical Implementation of Micromagnetic Approach	52
6.1	Space Discretization	52
6.2	Magnetic Field Discretization	53
6.2.1	External field	53
6.2.2	Exchange field	53
6.2.3	Magnetocrystalline anisotropy field	54
6.2.4	Demagnetization and magnetostatic field	55
6.2.5	Ampere field	57
6.2.6	Thermal field	59
6.3	Time Discretization	59
6.4	Energy Calculation	60
7	STT-MRAM Cells Structure Optimization	64
7.1	Influence of the Reference Layers	64
7.2	Composite Free Layer	67
7.2.1	Switching time reduction	70
7.2.2	Thermal stability factor calculation	71

7.2.3	Switching energy reduction	73
7.2.4	Acceleration switching effect	75
7.2.5	Standard deviation of the switching time distribution	77
7.3	Structure Optimization of the Composite Free Layer	78
7.3.1	Switching time and standard deviation	79
7.3.2	Thermal stability factor	81
7.3.3	Switching energy	82
8	Magnetization Oscillations in MTJ-based Structures	84
8.1	Switching Failure in a MTJ-based STT-MRAM	84
8.2	MTJ-based Bias-Field-Free Spin-Torque Oscillator	88
8.2.1	MTJ with half-elliptic reference layer	88
8.2.2	Two MTJs with shared free layer	90
9	Summary	98
	Bibliography	101
	List of Publications	126
	Curriculum Vitae	134

List of Abbreviations

1T0C	one-transistor-zero-capacitor
1T1C	one-transistor-one-capacitor
1T1R	one-transistor-one-resistor
CBRAM	conductive bridge RAM
CMOS	complementary metal-oxide-semiconductor
DMTJ	dual MTJ with two barriers
DRAM	dynamic random access memory
FET	field-effect transistor
GAAFET	gate-all-around FET
GMR	giant magnetoresistance
HRS	high resistance state
LL	Landau-Lifshitz
LLG	Landau-Lifshitz-Gilbert
LLGS	Landau-Lifshitz-Gilbert-Slonczewski
LRS	low resistance state
MIM	metal-insulator-metal
MOSFET	metal-oxide-semiconductor FET
MRAM	magnetoresistive RAM
MTJ	magnetic tunnel junction
MuGFET	multiple gate FET
PCRAM	phase change RAM
Pr-MTJ	cell utilizing precessional switching mechanism
RAM	random access memory
RRAM	resistive/redox RAM
SAF	synthetic antiferromagnet
SMTJ	single MTJ with one tunnel barrier
SONOS	semiconductor-oxide-nitride-oxide-semiconductor
SRAM	static RAM
STT-MRAM	spin transfer torque MRAM
TAS-MTJ	cell utilizing thermally assisted switching mechanism
TAT	trap-assisted tunneling
TMO	transition metal oxide
TMR	tunnel magnetoresistance
TT-MTJ	three-terminal MTJ cell
UT-DMTJ	ultra-thin dual MTJ

List of Symbols

Chapter 3: Stochastic Model of the Resistive Switching

A_e	dimensionless coefficient for electrons
A_i	dimensionless coefficient for ions
a	localization radius
E_a	annihilation energy of the m th vacancy V_o
E_f	threshold energy for the m th vacancy V_o
ΔE	difference between the energies of an electron positioned at sites n and m
$\Delta E'$	difference in energy of an ion after and before hopping
d	x -dimension of system
\hbar	reduced Planck constant
I	current generated by hopping
k_B	Boltzmann constant
q_e	electron charge
R_{nm}	hopping distance for electrons
T	local temperature
t	the time spent for moving a single particle (electron or ion)
U	applied voltage
Δx	difference between the x coordinate of the sites (vacancies) m and n
α	coefficients of the boundary conditions on the cathode
β	coefficients of the boundary conditions on the anode
Γ_{nm}	hopping rates from site n to site m for electrons
Γ_{0m}^{iC}	hopping rates from an electrode site 0 to an oxygen vacancy m
Γ_{m0}^{oC}	hopping rates from an oxygen vacancy m to an electrode site 0
$\Gamma_{(2N)m}^{iA}$	hopping rates from an electrode site $2N$ to an oxygen vacancy m
$\Gamma_{m(2N)}^{oA}$	hopping rates from an oxygen vacancy m to an electrode site $2N$
Γ'_n	hopping rates for ions

Chapter 4: Magnetoresistive Memory

E_b	energy barrier that separates the two magnetization state
e	electron charge
A_{cs}	cross-section area of the free layer
H_K	effective anisotropy field
$H_K^{in-plane}$	effective anisotropy field for in-plane MTJ
H_K^{perp}	effective anisotropy field for perpendicular MTJ
\hbar	reduced Planck constant
I_c	switching (critical) current
$I_c^{in-plane}$	critical currents for in-plane MTJ
I_c^{perp}	critical currents for perpendicular MTJ
k_B	Boltzmann constant
M_S	saturation magnetization of the free layer
R_{AP}, R_P	resistances in HRS and LRS, respectively
T	temperature
V	volume of the free layer
α	Gilbert damping parameter
Δ	thermal stability factor
$\Delta_{in-plane}$	thermal stability factor for in-plane MTJ
Δ_{perp}	thermal stability factor for perpendicular MTJ
η	polarizing factor
μ_0	magnetic constant
ρ_{AP}, ρ_P	resistivities in HRS and LRS, respectively
σ_{AP}, σ_P	conductivities in HRS and LRS, respectively

Chapter 5: Macro- and Micromagnetic Approach

A	material exchange constant
$a(j)$	time-dependent current-proportional function for the in-plane torque
$b(j)$	time-dependent current-proportional function for the perpendicular torque
d	thickness of the free layer
E_{ani}	magnetocrystalline anisotropy energy
$E_{current}$	energy associated with Ampere field
E_{demag}	demagnetization energy
E_{exch}	exchange energy
E_{ext}	energy associated with external magnetic field
E_{ms}	energy associated with magnetostatic coupling between the reference layer and the free layer
E_{th}	energy thermal field
e	electron charge
g	g-factor
$g(\Theta)$	Slonczewski's expression for spin-torque
\mathbf{H}_{ani}	magnetocrystalline anisotropy field
$\mathbf{H}_{current}$	Ampere field
\mathbf{H}_{demag}	demagnetization field
\mathbf{H}_{eff}	effective magnetic field
\mathbf{H}_{exch}	exchange field
\mathbf{H}_{ext}	external magnetic field
\mathbf{H}_{ms}	magnetostatic coupling between the reference layer and the free layer
\mathbf{H}_{th}	thermal field
\hbar	reduced Planck constant
\mathbf{J}	current density vector
j	current density
K_1, K_2	material anisotropy coefficient
\mathbf{M}	magnetization of the free layer
M_S	saturation magnetization of the free layer
M_{Sp}	saturation magnetization of the reference layer
\mathbf{m}	magnetization unit vector of the free layer
m_e	electron mass
m_x, m_y, m_z	projection of \mathbf{m} on x , y , and z axes, respectively
\mathbf{p}	magnetization unit vector of the reference layer
T	temperature
V	volume of the free layer
α	Gilbert damping parameter
β	coefficient of the perpendicular torque

γ	gyromagnetic ratio
δ	Dirac delta function
ε	energy density
η	polarizing factor
Θ	angle between direction of magnetization of the free and fixed layer
λ	phenomenological damping parameter
μ_0	magnetic constant
μ_B	Bohr magneton
ρ	volume magnetic charge
σ	surface magnetic charge
τ	spin transfer torque term
Φ_d	scalar potential of the stray field

Chapter 6: Numerical Implementation of Micromagnetic Approach

A	material exchange constant
$E_{ani}(i, j, k)$	magnetocrystalline anisotropy energy of the cell (i, j, k)
$E_{cell}(i, j, k)$	full energy of the cell (i, j, k)
$E_{current}(i, j, k)$	energy of the cell (i, j, k) associated with Ampere field
$E_{demag}(i, j, k)$	demagnetization energy of the cell (i, j, k)
$E_{exch}(i, j, k)$	exchange energy of the cell (i, j, k)
$E_{ext}(i, j, k)$	energy of the cell (i, j, k) associated with external magnetic field
$E_{ms}(i, j, k)$	energy associated with magnetostatic coupling between the reference layer and the cell (i, j, k)
$E_{th}(i, j, k)$	energy of the cell (i, j, k) associated with thermal field
E_{tot}	total energy of the free layer
$\mathbf{H}_{ani}(i, j, k)$	magnetocrystalline anisotropy field of the cell (i, j, k)
$\mathbf{H}_{current}(i, j, k)$	Ampere field of the cell (i, j, k)
$\mathbf{H}_{demag}(i, j, k)$	demagnetization field of the cell (i, j, k)
$\mathbf{H}_{eff}(i, j, k)$	effective magnetic field of the cell (i, j, k)
$\mathbf{H}_{exch}(i, j, k)$	exchange field of the cell (i, j, k)
$\mathbf{H}_{ext}(i, j, k)$	external magnetic field influences on the cell (i, j, k)
$\mathbf{H}_{ms}(i, j, k)$	magnetostatic coupling between the reference layer and the cell (i, j, k)
$\mathbf{H}_{th}(i, j, k)$	thermal field influences on the cell (i, j, k)
$\mathbf{J}(i, j, k)$	current density vector, current flows through the cell (i, j, k)
K_1, K_2	material anisotropy coefficient
k_B	Boltzmann constant
\mathbf{M}	magnetization of the free layer
M_S	saturation magnetization of the free layer
M_{Sp}	saturation magnetization of the reference layer
$\mathbf{m}(i, j, k)$	magnetization unit vector of the cell (i, j, k)
m_x, m_y, m_z	projection of \mathbf{m} on $x, y,$ and z axes, respectively
N_x, N_y, N_z	grid dimension in x, y, z direction, respectively
\mathbf{p}	magnetization unit vector of the reference layer
T	temperature
Δt	time step
ΔV	volume of the cell
$\Delta x, \Delta y, \Delta z$	x, y, z dimensions of the cell
μ_0	magnetic constant
$\sigma(i, j, k)$	Gaussian random uncorrelated function with standard deviation equal 1

1 Introduction

In modern microelectronic devices the dominant memory types are dynamic random access memory (DRAM), static RAM (SRAM), and flash memory. These types of memory store data as a charge state. For many decades these memory technologies have been successfully scaled down to achieve higher speed and increased density of memory chips at lower bit cost [86]. However, memories based on charge storage are gradually approaching the physical limits of scalability.

1.1 Charge-based Memory Technology

Although a new cell structure for DRAM has been developed by industry to overcome the scaling challenges at 30nm, a future size reduction below 20nm is facing physical limitations and elevated process complexity resulting in high manufacturing cost. DRAM with vertical gate type transistors was introduced in order to resolve the critical scaling problems, but it is not easy to reduce the size of the cell capacitor for the 20nm technology node [86]. A DRAM memory cell based on a transistor alone technology could solve this problem. The ultimate advantage of this new concept is that it does not require a capacitor, and, in contrast to traditional 1T1C DRAM cells, it thus represents a 1T0C cell named zero-capacitance RAM (ZRAM).

The concept of a DRAM memory cell based on a transistor alone was introduced already a decade ago [5],[9],[10],[62],[81],[176],[210],[255]. The functionality of the first generation ZRAM is based on the possibility to store majority carriers in the floating body of a silicon on insulator (SOI) transistor. The carriers are generated by impact ionization caused by the minority carriers close to the drain. The threshold voltage is modified because of the charge accumulated in the body thus guaranteeing the two states of a MOSFET channel, open and close, for a gate voltage chosen between the two thresholds.

The idea of the second generation ZRAM is to exploit the properties of the parasitic bipolar transistor [175], allowing to expand the ZRAM applicability to such advanced non-planar devices as FinFETs, multiple gate FETs, and gate-all-around FETs. Contrary to the first generation ZRAM, the current is flowing through the body of the structure. This increases the value of current by roughly the ratio of the fin radius to the surface layer thickness. The majority carriers are generated due to impact ionization. They are stored under the gate at the silicon/silicon dioxide interface. The

stored charge provides good control over the bipolar current, in contrast to the first generation ZRAM, where the charge is stored in the area close to the buried oxide.

While keeping all advantages of the first ZRAM generation, the most recent generation of ZRAM cells [175] is characterized by a significantly enlarged programming window and much longer retention times. In [223] it is demonstrated that the programming window, which is formed by the two current values and the two gate voltage values when switching appears, is sufficiently large for stable ZRAM operation on 50nm double-gate transistors. In 2008, a 128Mb floating body RAM was designed and developed [81].

The meta-stable dip RAM (MSDRAM) is based on the MSD hysteresis effect [11] in fully depleted (FD) transistors [12],[13]. State 1 differs from State 0 by the presence of majority carriers in the gate-to-drain/source regions, which in turn determines the current flow at the back channel. Majority carriers are generated by band-to-band tunneling [94].

To reduce the operating voltage, a new concept of a 1T0C cell for advanced RAM (ARAM) was proposed [183],[184],[186]. The ARAM structure is represented in a form of a FD SOI transistor with two ultrathin semibodies physically isolated by a middle oxide but sharing the source and drain regions [186]. Two separate semibodies allow to store the population of majority (holes) and minority (electrons) charges separately without triggering their recombination. The transition between State 1 and State 0, and vice versa, occurs due to charging and discharging the top (between gate and middle oxide) semibody by holes. The memory cell is programmed via impact ionization or band-to-band tunneling.

The physical separation of the channels leads to substantial operation flexibility and improved performance, but introduces additional complexity in the cell architecture [185]. To overcome this drawback, a second generation ARAM (A2RAM) was proposed [185],[187],[188],[189]. The new cell architecture used the electrical isolation of the two types of carriers by a vertical p-n junction.

Most of 1T0C memories use impact ionization or band-to-band tunneling for writing, leading to slow write speeds and requiring high operating voltage [237]. Recently, the zero subthreshold swing and zero impact ionization RAM (Z^2 RAM) was proposed and studied in details [235],[236],[237],[238],[239]. The Z^2 RAM is a forward-biased PIN diode, where the FD body is only partially covered by the gate [235].

Based on a 1T0C memory cell the concept of the unified memory (URAM) was proposed. The URAM combines a non-volatile memory and 1T0C memory cell [45]. Non-volatility is achieved through the integration of the charge trapping layer (tunneling oxide/nitride/blocking oxide). Electrons are injected and trapped in the silicon nitride layer like in a standard SONOS memory [45].

The next step in the evolution of memory concepts involves the development of universal memory. Future universal memory should combine not only the high density of DRAM with non-volatility (flash memory), but also possess the main advantages of

other charge based memory types, i.e. include the high speed of SRAM [44]. Therefore development of conceptually new types of memories based on a different storage principle are gaining momentum. Apart from good scalability, high operation speed, long retention time, and non-volatility the new type of memory must also exhibit low operating voltage, low power consumption, high endurance, and a simple structure [137].

1.2 Outline of the Thesis

This thesis is devoted to the concepts of the emerging resistive memory technology. Modeling of the two classes of resistive memory, namely, based on the change of the ohmic resistance (RRAM) and on the change of the magnetoresistance (STT-MRAM) is especially considered. Thus, the document can be divided into two parts: Chapter 2 and 3 are devoted to the memory concepts based on the ohmic resistance, Chapters 4 through 8 are devoted to magnetoresistive memory.

Chapter 2 introduces ohmic resistive switching memory, describes the basic operation principles of this memory concept, the materials used, and identifies the main problems impeding its large-scale integration. In addition, Chapter 2 describes the mechanisms of resistive switching and the models representing them. Due to the high interest in this type of memory and the rapid development of modeling techniques, the modeling methods are divided into three stages: (i) first suggestions and early models; (ii) current research status; (iii) a proposal of a new stochastic model of resistive switching (Chapter 3).

Chapter 4 introduces the concept of magnetic memory, describes the current magnetoresistive memory technology, and focuses on the basic principles of operation and the nature of the phenomena of magnetoresistance changes (GMR and TMR). Furthermore, the basic architecture of the magnetoresistance memory cells are presented and the major problems are identified.

Chapter 5 describes the theoretical background of micromagnetic simulations. The discretization of the magnetic field and the solution of the magnetodynamic equations by the finite difference method are shown in Chapter 6.

Chapter 7 describes the main results of the magnetoresistive memory simulations and presents methods of memory cell structure optimization. Furthermore, Chapter 8 discusses the reliability issues and two concepts of spin-torque oscillators based on the found parasitic effect for the switching memory process are proposed.

Finally, in Chapter 9, the main results of the thesis are summarized.

2 Resistive Change Based Memory

First intensive studies of conductivity in metal-insulator-metal (MIM) structures were made in the 1960s and 1970s. At that time different phenomena, such as negative differential resistance [83], memory switching [82], threshold switching [177] were discovered and first extensive physical analysis of these effects was performed [47],[48],[49],[50],[76],[84],[216],[221]. The use of these phenomena for memory devices was proposed [55],[178]. But the early observations of resistive switching were not robust enough for real memory applications and these reports remained mostly in the domain of scientific studies [244].

Nowadays resistive switching memory is represented by RRAM, phase change RAM (PCRAM), and conductive bridge RAM (CBRAM) types.

CBRAM, also called in the literature as memory with an electrochemical metallization (ECM) [241] cell or a programmable metallization cell (PMC) [135], is based on a solid state electrolyte in which mobile metal ions can create a conductive bridge between the two electrodes under the influence of an electric field. The source of mobile metal ions is one of the electrodes, which is made from an electrochemically active metal, such as Ag, Cu, or Ni. Electrochemically inert metals, such as Pt, Ir, W, or Au are used for the second electrode [242].

PCRAM employs the difference in resistivity between crystalline and amorphous phases of a chalcogenide compound [143]. After the fabrication of devices a chalcogenide compound is in a crystalline phase. For a transition to an amorphous phase, a chalcogenide compound should be melted and rapidly quenched, for which a large electric current pulse is applied. For a transition back from the amorphous to the crystalline phase, a chalcogenide compound (operation region) must be annealed at a temperature between the crystallization temperature and the melting temperature, which is done by applying a medium electrical current pulse with time period sufficient for crystallization [245].

RRAM, also called in the literature as valence change memory (VCM) [242], exploits the phenomenon of the resistive switching in oxides.

2.1 RRAM Basics

Resistive switching is toggling the electrical conductance of the insulator in a MIM structure from the high resistance state (HRS) to the low resistance state (LRS) and

vice versa by applying the electric field. The HRS can mean logical 1 and the LRS can mean logical 0, or vice versa, depending on the technology.

2.1.1 Resistive-switchable oxides

In 2000 Beck *et al.* and in 2001 Watanabe *et al.* reported an electrical resistive switching in Cr-doped SrZrO₃ [14] and Cr-doped SrTiO₃ [243], respectively. In 2004, Baek *et al.* [6] have demonstrated NiO memory cells integrated with the conventional complementary metal-oxide-semiconductor (CMOS) transistor in a one-transistor-one-resistor (1T1R) device structure. After that, the new phase of studying the resistive switching phenomenon and RRAM began. Resistive switching was shown in different materials/structures (Table 2.1).

material	ref.	material	ref.
metal oxide			
NiO	[42],[132],[205], [206],[207]	Cu _x O	[59]
Nb ₂ O ₅	[213],[214]	CoO	[208]
TiO _x	[41],[63],[107], [109],[138],[139], [190],[209],[254]	ZnO	[34],[149],[250]
ZrO ₂	[144],[156]	HfO ₂	[37],[38],[78], [131],[146]
MgO _x	[110]	SnO ₂	[172]
Al ₂ O ₃	[155]	Ga ₂ O ₃	[29]
		WO _x	[22],[85]
heterostructure of metal oxides			
AlO _x /TiO _x	[122],[127]		
perovskite oxides			
Pr _{1-x} Ca _x MnO ₃	[202]	V-doped SrZrO ₃	[154]
Nb-doped SrTiO ₃	[215]	Fe-doped SrTiO ₃	[170]

Table 2.1: Resistive-switchable oxides.

The concepts of RRAM proposed in 2010 by Ho *et al.* (NDL) [85] and Kim *et al.* (Samsung) [127] have already surpassed the scaling limit of charge-based storage memories [39]. In 2013, RRAM has been demonstrated on a 32Gb test chip [160]. Despite the obvious progress in the last years, details about the physics of the switching mechanism remain an area of active research.

2.1.2 Unipolar and bipolar behavior

The switching event from LRS to HRS is called the RESET process and, conversely, the switching event from HRS to LRS is called the SET process. Usually, for fresh samples in its initial resistance state, a voltage larger than the SET voltage is needed to

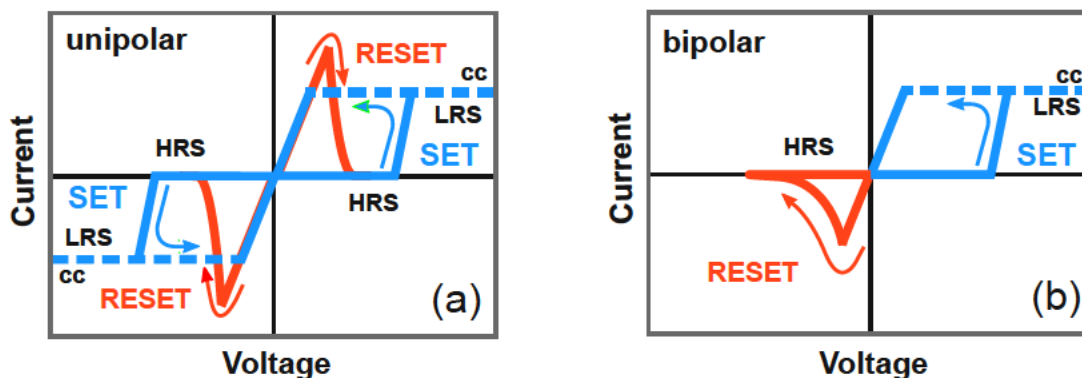


Figure 2.1: Schematic illustration of $I - V$ curves during different type of resistive switching: (a) unipolar; (b) bipolar [242].

trigger the transition from HRS to LRS than during the subsequent cycles. This event is called the FORMING process. The FORMING/SET process is completed when the current in the system becomes equal to the compliance current (cc) level.

Depending on the relative polarities of the SET and RESET voltage, the resistive switching phenomenon is called either unipolar or bipolar (Figure 2.1). The switching operation is called bipolar, when the SET to LRS occurs at one voltage polarity and the RESET to the HRS at the opposite voltage polarity. The switching operation is called unipolar, when the switching procedure does not depend on the polarity of the write voltage [242].

unipolar	bipolar
Pt/NiO/Pt [207]	Pt/NiO/SrRuO ₃ [42]
Pt/TiO ₂ /TiN [254]	Pt/TiO ₂ /TiN [68],[254]
Pt/TiO ₂ /Pt [107],[190]	Pt/TiO ₂ /Pt [107]
Pt/ZrO ₂ /Pt [156]	Ti/ZrO ₂ /Pt [156]
Al/ZrO ₂ /Pt [156]	
TiN/HfO ₂ /Pt [78]	TiN/HfO ₂ /Pt [78]
Pt/HfO ₂ /Pt [131]	
Ni/HfO ₂ /TiN [38]	
Pt/ZnO/Pt [34]	TiN/ZnO/Pt [250]

Table 2.2: Dependence of the switching behavior on the insulator materials.

The switching behavior is not only dependent on the insulator material (Table 2.2) but also depends on the choice of the metal electrodes and their interfacial properties [125],[244]: Both switching types could coexist in one system. For example, Pt/TiO₂/Pt shows both types of switching and the factor determining the switching type is the level of the cc (low cc (<0.1mA) activates bipolar switching; rather high cc (>1mA) activates unipolar switching).

2.1.3 Challenges of the RRAM

Non-uniformity of device characteristics appears a major challenge for to large-scale manufacturing of RRAM. Significant parameter fluctuations exist in term of variations of the switching voltage as well as the resistances in HRS and LRS (R_{LRS}/R_{HRS} distribution). The variation of the resistive switching includes temporal fluctuations (cycle to cycle) and spatial fluctuation (device to device) [244]. The LRS resistance variation comes from the variation of the number or the size of conductive filaments, thus the reduction of possible filament paths effectively confines the active switching area and thereby may reduce the LRS variation. The HRS resistance variation comes from the variation of the ruptured conductive filaments length, thus any variation of the tunneling gap distance results in an exponential dependence of the tunneling current on the tunneling distance. Resistance variation could lead to a SET failure and re-RESET during SET process [8].

One of the potential methods to stabilize the characteristics of the resistive switching is the oxide doping. In 2012, Syu *et al.* [225] proposed the Si interdiffusion method to enhance the resistive switching characteristic of the WO_x . Before Si enrichment the diverse oxidation states in the WO_x film were providing the stochastic conduction paths, which lead to the irregular resistance switching behavior. The Si interdiffusion in WO_x resistance switching layer can effectively localize the filament conduction paths to improve the resistance switching property.

To solve the problem of RRAM variability, first and foremost, one needs a better understanding and control of the SET/RESET processes. Development of accurate and flexible models of switching is paramount for future progress in RRAM technology [104].

2.2 Mechanisms and Models of Resistive Switching

Most switching materials show filamentary-type switching behavior. Filamentary-type switching involves the formation of a conductive path through an insulator layer, which leads to a transition to a LRS. The disruption of this path leads to a transition to a HRS. Non-filamentary-type switching has also been observed in several systems [22],[170],[215]. This type is also known as an interface-type switching [201]: it does not involve electroforming, and both SET and RESET switching appear as a rather gradual than abrupt process. Another distinct feature of the non-filamentary switching is that the system resistance depends on the cell size [108].

2.2.1 First attempts of explanation and early models

In the literature several physical mechanisms/models have already been suggested for the explanation of SET/RESET processes (Table 2.3).

macroscopic level	microscopic level
[28],[32],[33],[67],[124], [126],[128],[151],[173],[194], [195],[196],[200],[226]	[72],[73],[174],[192],[249]

Table 2.3: First suggestions and early models of resistive switching.

Unipolar switching

The first suggestion about filamentary conduction and switching for unipolar behavior was made by Dearnaley [47] in 1967. Dearnaley did not specify conductive filaments at the atomic level, although he suggested some possible models such as Si-O-Si chains in SiO_x [47] and, more generally, M^{z+} - M^{z+} chains [48]. In this model, the RESET switching is a result of the rupture of the conductive filaments in the insulating matrix by Joule heat, while a mechanism for SET switching is assumed to be a recovery of the ruptured conductive filaments. The mechanism based on these processes is called the fuse-antifuse type [242] and is most commonly used to describe unipolar switching. Dearnaley's ideas were further developed in the macroscopic SET and/or RESET models proposed by Sato *et al.* [200], Russo *et al.* [194],[195],[196], Cagli *et al.* [28], Lee *et al.* [151], Ielmini *et al.* [99], and Bocquet *et al.* [25] for describing the resistive switching behavior in NiO and/or TiO₂. In these publications the RESET switching is explained by dissolution of conductive filaments owing to Joule heat. According to the results of simulations the conductive filament rupture/recombination should occur in the middle of the filament. However, several experimental works have shown that the switching-determining region is rather located at the interface between anode/NiO [132], anode/TiO₂ [123], and cathode/NiO [121]. Thus the conductive filament breaking should occur in this region. Kim *et al.* [124],[126] have solved the problem by assuming a cone-shaped conductive filament for TiO₂, NiO. This form of the conductive filament involves heating in a tight spot and a formation of the hottest place at the interface, where, according to the experimental results [121],[123],[132], the rupture occurs. The existence of more than one filament in a single memory cell was suggested [1],[120],[145],[150], and several aspects of such a switching in NiO were modeled by Kinoshita *et al.* [133].

Attempts to explain resistive switching phenomenon at the atomistic level were undertaken by Chudnovskii *et al.*, in 1996 [43]. Their predictions were based on a simple free energy calculation of a lower oxide (with lower stoichiometric oxygen concentration) formation reaction. They presupposed that the resistive switching behavior is due to the phase transition from a highest oxide (HRS) to a lower oxide (LRS), e.g. $\text{TiO}_2 \rightleftharpoons \text{Ti}_n\text{O}_{2n-1}$ ($n = 4..9$). This reaction is spontaneous and could be accelerated by Joule heating during FORMING/SET processes. Note that this calculation is only valid for a transition metal oxide (TMO) film on an metal electrode. In 2010, Kwon *et al.* [139] directly observed the nanoscale conductive filaments in a Pt/TiO_x/Pt memory cell by high-resolution transmission electron microscopy (HR-TEM), and identified

the cone-shaped conductive filaments composed of the oxygen-deficient Magnéli phase, e.g. Ti_4O_7 .

A non-thermal approach to a unipolar switching was proposed by Chae *et al.* [32]. In this model the SET/RESET switching is based on a random circuit breaker network. Simulation results can mimic the experimental behavior, but the model lacks the detailed physics of the circuit breakers [108].

Bipolar switching

The first attempts to explain the bipolar switching were made by the pioneers in the field in the 1960s and 1970s. In 2000, Beck *et al.* [14] suggested that charge-transfer processes via donor and acceptor levels (Cr^{3+} and Cr^{4+}) appear to be the mechanism for carrier creation and transport within the Cr-doped insulator SrZrO_3 . Then in 2001, Rossel *et al.* [191] concluded that the current flows through localized channels/filaments rather than homogeneously across the bulk of the film. This current is mainly due to the hopping or tunneling of charges between the adjacent sites or traps localized in the gap of the insulator. The conductive filament formation and rupture should be coupled with structural change. Tsui *et al.* [231] proposed a conduction mechanism via crystalline defects generated by the applied electric field. Later, the change in the conductivity of conductive filaments in Cr-doped SrZrO_3 was explained as the oxygen vacancy drift along the applied electric field [106]. Then, Jeong *et al.* [109] proposed a mechanism for bipolar switching in TiO_2 based on oxygen vacancies (V_o) migration.

A non-filamentary approach to bipolar switching was suggested by Sawa *et al.* [202] in 2004. They concluded that the resistive switching in $\text{Ti}/\text{Pr}_{0.7}\text{Ca}_{0.3}\text{MnO}_3/\text{SrRuO}_3$ can be explained by an interface model of $\text{Ti}/\text{Pr}_{0.7}\text{Ca}_{0.3}\text{MnO}_3$ which has a sufficiently [145] high density of traps to form a Schottky-like barrier. This mechanism of resistive switching was adopted by Fujii *et al.* [67] to interpret the switching in $\text{Au}/\text{SrRuO}_3/\text{SrTi}_{0.99}\text{Nb}_{0.01}\text{O}_3$.

A phenomenological model which may explain several particular aspects of the bipolar switching phenomenon was proposed by Rozenberg *et al.* [192],[193]. The insulating medium contains metallic domains, which in explicitly correspond to charge traps in the real system such as dopants, vacancies, metallic clusters, and nanodomains. It is assumed in this model that there are just three types of domains. The top and bottom domains are taken to be smaller than the middle one. This domain differentiation might be justified by the different properties of the electronic states close to the interfaces of the metal electrodes. Electric current is carried by electrons hopping between the domains as well as between a domain and an electrode, when an external voltage is applied. Resistive switching is explained on the basis of filling and desolating these domains.

One of the first microscopic SET/RESET mechanism for bipolar switching was proposed by Xu et al. [249], and termed the “unified physical model”. It is based on the following assumptions:

- the conduction of LRS and HRS is due to the electron hopping transport along localized oxygen vacancies V_o^+ in the conductive filaments;
- the switching between LRS and HRS is due to the formation and rupture of the conductive filaments made of V_o^+ ;
- SET is due to the creation of V_o^+ ;
- RESET is due to depletion of electrons in some V_o^+ along the conductive filament and recombination of the electron-depleted V_o^+ with the ions O^{2-} thus rupturing the conductive filament.

In [73], Gao *et al.* presented an extension of “unified physical model” as follows: O^{2-} are mainly accumulated at the interface between the electrode and the resistive layer and can jump over the interface barrier under an applied electric field. In [72] authors investigated the system in its LRS and showed, that the switching-determining region is formed near the cathode in the case of bipolar switching and near the anode in the case of unipolar switching.

Summary

At this stage of the investigation of resistive switching first explanations of phenomena were proposed. First macroscopic and phenomenological models, that could explain one or another experimental observation, were developed. The first experimental observation of a conductive filament was provided. Despite the fact that some ingredients of microscopic mechanisms have also been suggested the microscopic model capable of reproducing a resistive switching behavior in oxides (FORMING/SET and RESET process) was not provided.

2.2.2 Current research progress

Lately the number of papers devoted modeling the resistive switching phenomena has rapidly increased (Table 2.4).

Resistive switching in oxides

By extending the main assumptions of the “unified physical model” a microscopic stochastic model of the resistive switching was developed (Chapter 3). The improvement of the “unified physical model” is continuously ongoing:

macroscopic level	microscopic level
[21],[25],[96],[97],[99],[133],[147],[152],[161],[251]	[18],[19],[20],[38],[51],[52],[70],[71],[74],[91],[92],[98],[142],[162],[193],[197],[232],[233],[234],[256],[257],[258],[259],[266]

Table 2.4: Macroscopic and microscopic models of resistive switching.

- Gao *et al.* introduced the transport of O^{2-} through the interface between an electrode and oxygen layer [71];
- Gao *et al.* modeled the retention failure behavior [74];
- Gao *et al.* attempted to extend the model to unipolar behavior and added the Joule heating induced thermal creation of O^{2-} [70];
- Lu *et al.* proposed new modeling methods for the RESET process [162];
- Huang *et al.* [91] proposed a new stochastic approach with rates slightly different to those used here (see below);
- Chen *et al.*, Huang *et al.* investigated the device degradation and carried switching optimization [36, 90];
- Huang *et al.* presented a physics-based analytic model of RRAM operation for circuit simulation [92];
- Yu *et al.* [258] concluded that a more favorable conduction mechanism for TiN/HfO_x/Pt is the trap-assisted tunneling (TAT).

In [257, 256] the TAT was added to the “unified physical model”.

In 2010, Yoo *et al.* [252] and Hwang *et al.* [95] observed a dendrite-like conductive filament in NiO layer (Figure 2.2). In this case the resistive switching occurs as follows [125]:

- during the FORMING process, the oxygen ions O^{2-} migrate from NiO to the electrode;
- holes are the major injected carriers, the hole injection occurs at the anode interface, therefore the Joule heating effect is most serious in this region, that leads to migration of O^{2-} ions to the anode;
- the dendrite-like conductive filament is formed from percolated metallic Ni material with Ni atoms being diffused away from their more point-like source at a location near the anode toward the cathode;

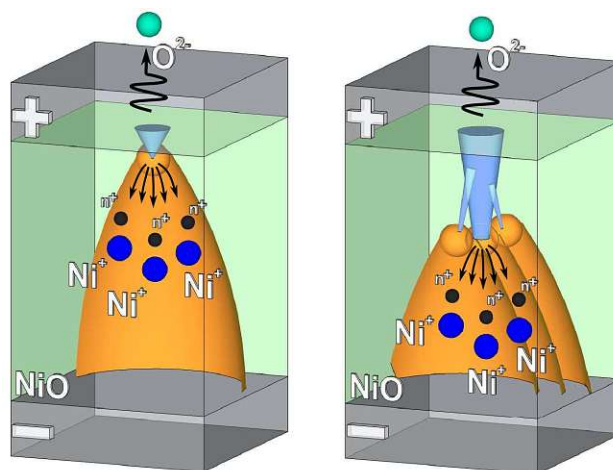


Figure 2.2: Schematic illustration of the conductive filament growth process in NiO [125].

- rupture of the conduction filament during switching from the LRS to the HRS is taking place near the anode [95].

Phenomenological models which explain several particular aspects of the bipolar switching phenomenon were also proposed by Bertin *et al.* [21], Liu *et al.* [161], Yu *et al.* [259], Sasaki [197], etc. Non-filamentary models for unipolar switching were also reported in the literature, e.g. Xue *et al.* have suggested a model based on the Mott-Hubbard metal-insulator transition picture [251].

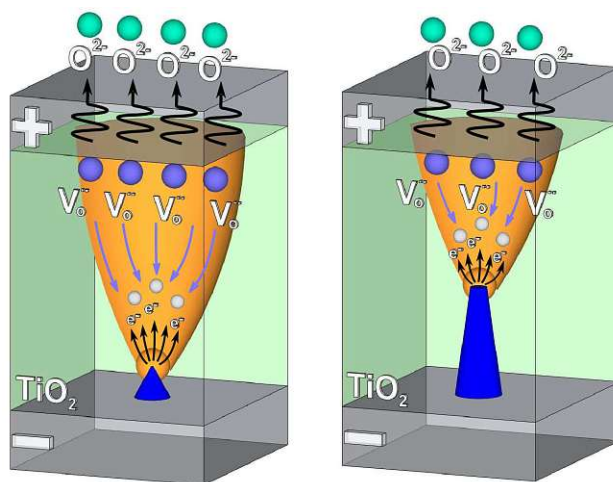


Figure 2.3: Schematic illustration of the conductive filament growth process in TiO₂ [125].

A fully microscopic study of SET/RESET process in the case of unipolar switching in Pt/TiO_x/Pt (Figure 2.3) was presented in [266]. The authors concluded that:

- during the FORMING process, oxygen vacancies (V_o) and neutral oxygen atoms are generated near the anode [109];
- under a high electric field, these V_o drift toward the cathode and contribute into the growth of a cone-shaped Ti_4O_7 filament [139];
- the oxygen atoms are removed from the oxide and chemisorbed at Pt grain boundaries near the anode interface;
- the filament is established to be disrupted only near the anode [123];
- because the matrix TiO_x is in LRS, the applied voltage pulse causes high current density and intense Joule heating in the filament region. The temperature could become sufficiently high to melt Ti_4O_7 and release V_o frozen in the Magnéli phase;
- conductance in LRS is mediated by the Poole-Frenkel mechanism.

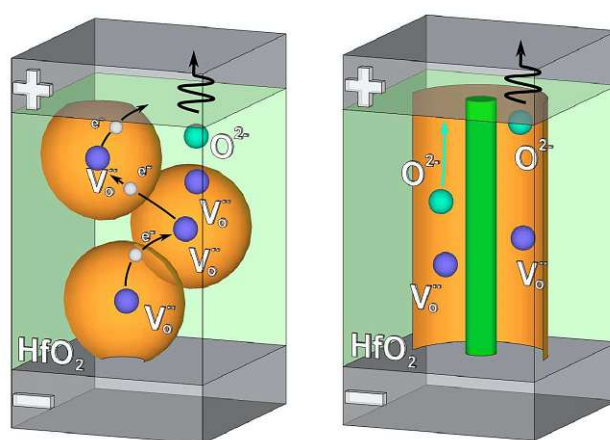


Figure 2.4: Schematic illustration of the conductive filament growth process in HfO_2 .

Bersuker *et al.* [18] proposed a microscopic filamentary-type model of resistive switching for $TiN/HfO_2/TiN$ (Figure 2.4). They claimed that:

- the defects assisting the electron transport are positively charged V_o located at the grain boundaries (GBs);
- oxygen dissociations are driven by the applied electric field and become more mobile at elevated temperatures;
- O^{2-} ions released during the filament formation are stored near the interface between anode and oxygen layer;
- the rupture of the conductive filament occurs near this interface;
- the conductivity is due to the multiphonon TAT and direct tunneling, through the $V_o^+ + e \rightarrow V_o^0 \rightarrow V_o^+ + e$ process.

Thus the population of electrically active V_o^+ traps decreases closer to the anode. Several aspects of this model were also discussed in the earlier work by the same group [19],[20],[232],[233],[234]. In a macroscopic approximation model based on a practically similar mechanism for HfO_2 was done by Ielmini [96],[97]. Lerantis *et al.* [142] and Ielmini *et al.* [98] have presented an alternative numerical RESET microscopic model for HfO_2 . In 2013, Kalantarian *et al.* [113] showed the mechanism of the RESET process in HfO_2 , where the RESET process occurs due to the migration of O^{2-} ions stored in the bulk of the oxide layer.

Degraeve *et al.* [51],[52] have suggested a conductive filament in an “hour glass” form for $\text{TiN}/\text{HfO}_2/\text{Hf}/\text{TiN}$. In this model the conductive filament never breaks but only narrows. A potential barrier is raised in the constriction due to quantum mechanical confinement, which blocks the current. Another distinctive feature of this model is the absence of V_o generation/recombination and the whole resistive switching process is due to the V_o flow from one part of the “hour glass” to another, and vice versa. In [182], an extension of the “hour glass” model was presented, which considers the event of conductive filament breaking.

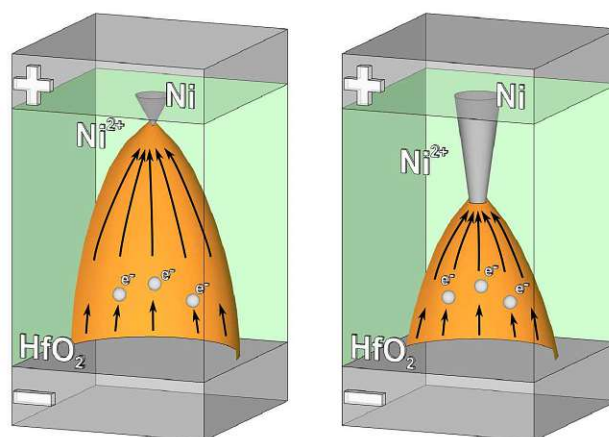


Figure 2.5: Schematic illustration of the conductive filament growth process in HfO_2 with Ni electrode.

In 2012, Chen *et al.* [38] have observed unipolar resistive switching in $\text{Ni}/\text{HfO}_2/\text{TiN}$ and proposed the resistive switching mechanism (Figure 2.5) as follows:

- the diffusion of Ni during the FORMING, leads to the creation of a Ni filament in HfO_2 and hence to a LRS;
- RESET happens due to the thermal dissipation process coupled with the drift of oxygen interstitials under the electrical field which could re-oxidize and disrupt the Ni filament close to the Ni/HfO_2 interface;
- SET again due to injection of Ni. The formation of Ni conductive filament in HfO_2 is fully consistent with other experimental work [157] for $\text{Si}/\text{HfO}_2/\text{Ni}$.

Resistive switching in stacked oxide

Recent experiments have shown that use of a stacked oxide RRAM structure is one of the most promising methods to improve the properties of this type of memory [40],[79],[87],[129],[152],[246]. In [79] the authors used a quantum-point contact model [53] for modeling of filament-resistance states.

In Oct. 2013, Kamiya *et al.* [115],[116] has proposed a possible mechanism, the vacancy “Cohesion-Isolation” phase transition, for explanation of resistive switching in stacked oxides $\text{Al}_2\text{O}_3/\text{HfO}_2/\text{Hf}$ [79] in microscopic level. Several aspects of this mechanism were also discussed in the earlier work of this group [114],[211].

2.3 Conclusions

Resistive memory has come a long way from the early works to prototyping of the RRAM arrays. Currently, oxide-based resistive memory is widely accepted as a potential candidate of the future universal memory. One of the main advantages of a RRAM is its simple structure. The RRAM prototypes have already surpassed the scaling limits of charge-based storage memories. However, the main challenge of this type of memory is the non-uniformity of device characteristics. To solve these problems one needs a better understanding and control of the SET/RESET processes. Development of accurate and flexible models of switching is paramount for future progress in RRAM technology.

In early works macroscopic and phenomenological models, which could explain one or another experimental observation were proposed. The first experimental observation of a conductive filament was provided. Despite the fact that some microscopic mechanisms have been suggested, a microscopic model capable of reproducing the resistive switching behavior in oxides (FORMING/SET and RESET process) was not provided.

Work on the description and clarification of the resistive switching phenomenon continues today. The mechanisms for filamentary-type switching phenomena are not completely understood, although up to now experimental evidence supporting one or another hypotheses have been revealed. The current state-of-the-art understanding of the problem lies in the fact that the resistive switching is associated with the structural changes within the oxide, i.e. the formation/annihilation/migration of the defects, and an electron transport through these defects.

The first full stochastic model of the oxide resistive switching, based on some variation of the “unified physical” mechanism was developed. The main advantage of this stochastic model is that for the first time movement of oxygen ions and electron hopping were taken at equal footing, which allowed us to describe the full cycle of resistive switching, as will be shown in Chapter 3.

3 Stochastic Model of the Resistive Switching

3.1 Switching Mechanism

The resistive switching behavior in the oxide-based memory is associated with the formation and rupture of a conductive filament. The conductive filament is formed by localized oxygen vacancies V_o [72] or domains of V_o . The conduction is due to electron hopping between these V_o . Figure 3.1 shows schematic illustration of the resistive switching mechanism in bipolar oxide-based memory. Formation and rupture of the conductive filament is due to a redox reaction in the oxide layer under a voltage bias. If a positive voltage is applied, the formation of a conductive filament begins, when the voltage reaches a critical value sufficient to create V_o by moving an oxygen ion (O^{2-}) to an interstitial position. This leads to a sharp increase in the current signifying a transition to a state with low resistance.

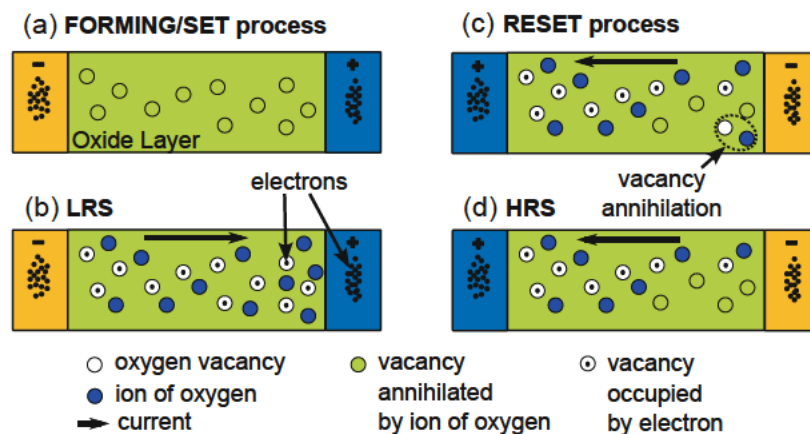


Figure 3.1: Illustration of the resistive switching mechanism in bipolar oxide-based memory cell: (a) schematic illustration of the FORMING/SET process, (b) schematic view of the conducting filament in the low resistance state (on state), (c) schematic illustration of the RESET process, and (d) schematic view of the conducting filament in the high resistance state (off state). Only the oxygen vacancies and ions, which impact the resistive switching, are shown.

If a reverse negative voltage is applied, the current increases linearly, until the applied voltage reaches the value at which annihilation of V_o is triggered by means of moving

O^{2-} to V_o . The conductive filament is ruptured and so the current decreases. This is the transition to a state with high resistance.

3.2 Model Systems Description

Figure 3.2 shows the unit cell of the two-dimensional (2D) model system. Columns with numbers 0 and $2N$ are reserved for the electrodes (there are generators and receivers of electrons in a model system). Places in odd-numbered columns at the intersections of the solid lines are reserved for oxygen vacancies V_o . An oxygen vacancy is formed, when an oxygen ion O^{2-} moves to a nearest empty interstitial position located at the intersections of the dotted lines (Figure 3.2). An oxygen vacancy can be occupied by an electron hopping from another oxygen vacancy or from an electrode. Alternatively, an oxygen vacancy can be annihilated by an oxygen ion O^{2-} coming from a nearest interstitial position provided the vacancy is not occupied by an electron.

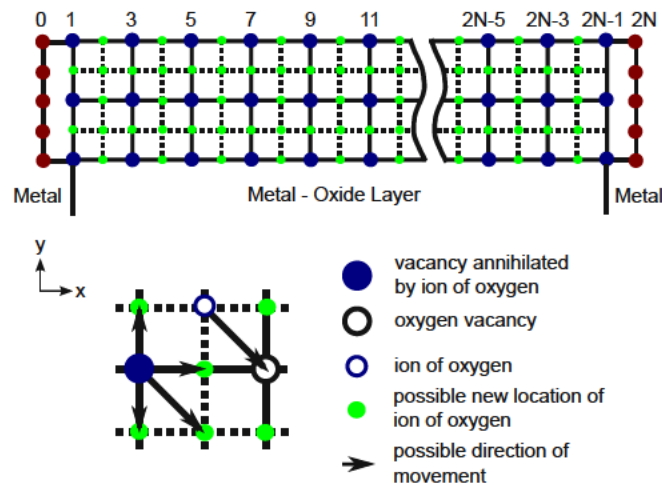


Figure 3.2: Schematic picture of the unit cell of the model system.

3.3 Electron Hopping and Ion Motion

For modeling electrical conductivity in the low resistance state (i.e., when conductive filament is formed) by a Monte Carlo technique [134],[153], the following events are allowed:

- an electron hop into V_o from an electrode;
- an electron hop from V_o to an electrode;
- an electron hop between two V_o s.

In order to model the dependences of transport on the applied voltage and temperature the hopping rates for electrons are chosen as [224]:

$$\Gamma_{nm} = A_e \cdot \frac{\Delta E}{\hbar \cdot (1 - \exp(-\Delta E/k_B T))} \cdot \exp(-R_{nm}/a). \quad (3.1)$$

Here, \hbar is the reduced Planck constant, A_e is a dimensionless coefficient, ΔE is the difference between the energies of an electron positioned at sites n and m , R_{nm} is the hopping distance, a is the localization radius, T is the temperature, k_B is the Boltzmann constant. When an external voltage U is applied, the energy difference ΔE includes the corresponding voltage dependent term.

$$\Delta E = \frac{U}{d} \Delta x. \quad (3.2)$$

Here, d is the x -dimension of system, and $\Delta x = x_m - x_n$ is the difference between the x coordinate of the sites (vacancies) m and n .

Rates (Equation 3.1) are similar to those used in a single-electron transport theory [153]. An exponential in the denominator guarantees an exponentially small equilibrium occupation of a site m as compared to the occupation of a site n , if the condition $E_m - E_n \gg k_B T$ is satisfied. When the opposite condition $E_n - E_m \ll k_B T$ is fulfilled, the rate is proportional to the external field U/d . Therefore, rates (Equation 3.1) can mimic an Ohmic (linear in external field) transport in a system of equivalent sites having the same energy.

To further specify the electron dynamics, an electron is assumed to hop from the site n to the site m may occur only, if the site n was occupied and the site m was empty before the hopping event. This is a manifestation of the fact that the energy gap separating the vacancies with one and two electrons is assumed large enough that the double occupancy of a vacancy becomes prohibitively small.

The hopping rates between an electrode (0 or $2N$) and an oxygen vacancy m are described by [72]

$$\Gamma_{0m}^{iC} = \alpha \cdot \Gamma_{0m}, \Gamma_{m0}^{oC} = \alpha \cdot \Gamma_{m0}, \quad (3.3)$$

$$\Gamma_{(2N)m}^{iA} = \beta \cdot \Gamma_{(2N)m}, \Gamma_{m(2N)}^{oA} = \beta \cdot \Gamma_{m(2N)}. \quad (3.4)$$

Here, α and β are the coefficients of the boundary conditions on the cathode and anode, respectively, A and C stand for cathode and anode, respectively, and i and o for hopping on the site and out from the site. Contrary to an oxygen vacancy, an electrode is assumed to have enough electrons so that hopping from an electrode to a vacancy is always allowed, provided the vacancy was empty before the event.

Complimentary, an electrode has always a place to accept a carrier, so an electron can always hop at an electrode provided this event is allowed.

The current generated by hopping is calculated as

$$I = q_e \frac{\sum \Delta x}{d \sum t}. \quad (3.5)$$

Here, q_e is the electron charge, $t = \left(\sum_{m,n=0}^{2N} \Gamma_{mn} f_m (1 - f_n) \right)^{-1}$ is the time spent for moving an electron at a distance Δx , $f_n = 1(0)$, if the site n is occupied (empty), $f_0 = \alpha$ and $f_{2N} = \beta$, if an electron hops from an electrode, and $(1 - f_0) = \alpha$ and $(1 - f_{2N}) = \beta$, if a hop to an electrode occurs. Thus, $q_e \Delta x / d$ is a charge passing through an external circuit during a single hopping event [134]. The summation in Equation 3.5 is over all hopping events. Therefore, Equation 3.5 gives the current as the total charge passing through the external circuit during the total time $\sum t$ divided by the total time.

For modeling the resistive switching in oxide-based memory, in addition to the possible events of moving an electron, the dynamics of oxygen ions (O^{2-}) is introduced as follows:

- formation of V_o by O^{2-} moving to an interstitial position;
- annihilation of V_o by moving O^{2-} to V_o .

To describe the field-induced ion dynamics the ion rates are chosen similarly to Equation 3.1 as follows:

$$\Gamma'_n = A_i \cdot \frac{\Delta E'}{\hbar \cdot (1 - \exp(-\Delta E' / k_B T))}. \quad (3.6)$$

Here it is assumed that O^{2-} can move from the lattice site to the nearest interstitial provided the interstitial is empty. Alternatively, O^{2-} can move back from the interstitial to the nearest vacancy, provided it is not occupied by an electron. Because moving an ion is allowed only at the nearest sites, a distance-dependent term is incorporated in A_i . When the external voltage is applied, the difference in energy of an ion after and before hopping is computed as

$$\Delta E' = \frac{U}{d} \Delta x - E_c. \quad (3.7)$$

Here, E_c is a threshold energy for the m th vacancy V_o (E_f) or annihilation energy of the m th vacancy V_o (E_a), when O^{2-} is moving to an interstitial or back to V_o , respectively. The values of these energies depend on the insulating material.

3.4 Applications of Stochastic Based Method

All calculations are carried out on one or/and two-dimensional lattices, and the distances between two nearest neighboring V_o in all directions are equal, if no voltage or temperature is applied. Despite the fact that in the binary metal oxides oxygen vacancies can have three different charge states with charges 0, +1, and +2, to simplify the model, it is assumed that the oxygen vacancy is either empty or occupied by one electron [72]. This assumption is not a limitation, however, since, due to an energy separation between the three charge states, only two of them will be relevant for hopping and significantly contribute to transport.

Flowchart of the microscopic simulation of the resistive switching is presented in Figure 3.3.

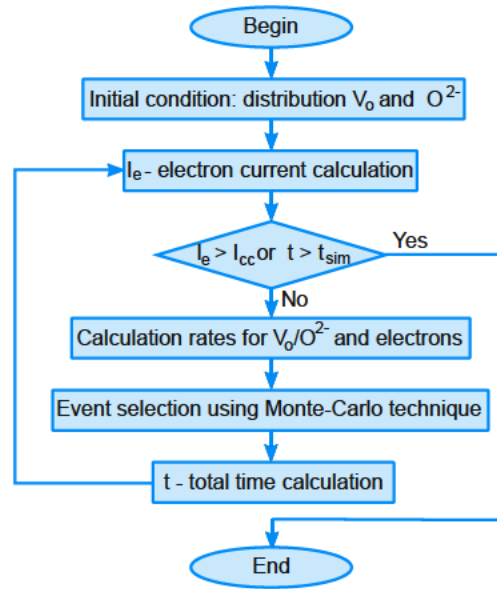


Figure 3.3: Flowchart of the microscopic simulation of the resistive switching.

3.4.1 Electron motion simulation

Calculation of electron occupation probability

Following [54], hopping is only allowed in one direction and only to/from the closest V_o . Each site i of a one-dimensional lattice of N sites is either occupied by an electron or empty; during a time interval dt , each electron has a probability Γ_{nm} of hopping to its right, provided the target site is empty; moreover, during the time interval dt , an electron may enter the lattice at Site 1 with probability $\alpha \cdot \Gamma_{01}$ (if this site is empty) and an electron at Site N may leave the lattice with probability $\beta \cdot \Gamma_{N(N+1)}$ (if this

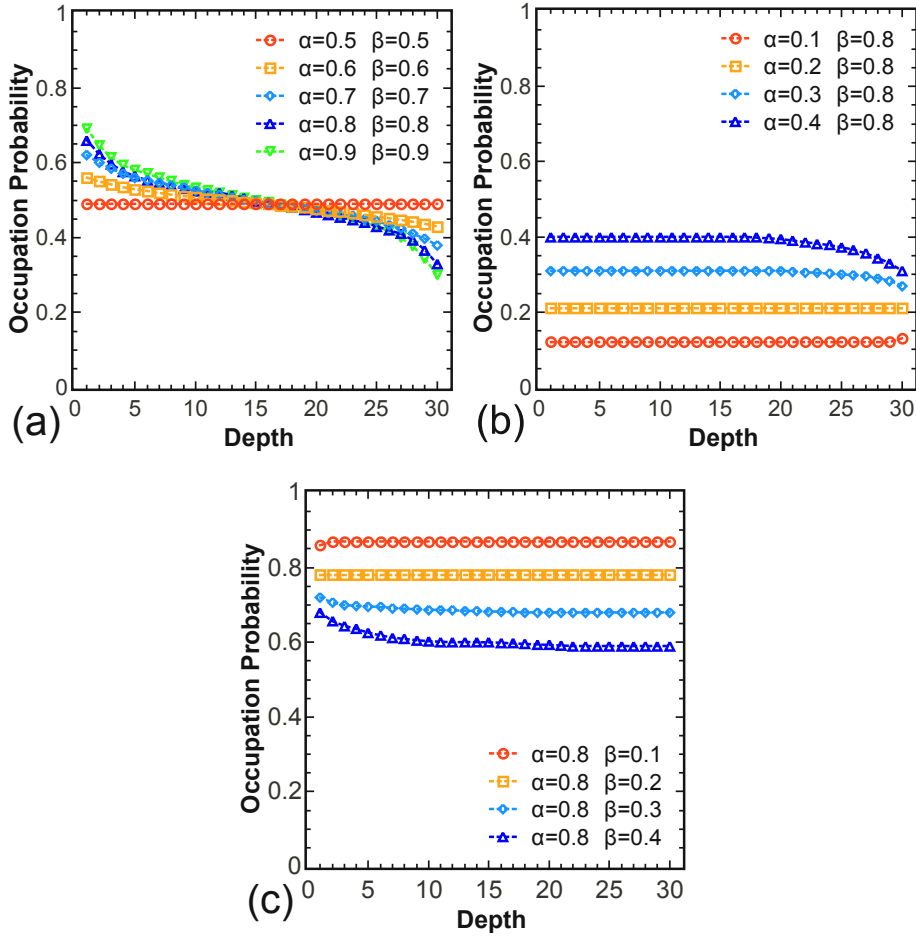


Figure 3.4: Calculated distribution of electron occupation probabilities for unidirectional next nearest neighbor hopping between the V_o (the 1st V_o is near the cathode, the last V_o is near the anode): (a) $\alpha > 0.5$ and $\beta > 0.5$, $p_c = 0.5$; (b) $\alpha < 0.5$ and $\alpha < \beta$, $p_c = \alpha$; (c) $\beta < 0.5$ and $\beta < \alpha$, $p_c = 1 - \beta$.

site is occupied). For calibration the exact results [54] were used. The occupation probability of a central V_o (p_c) is described, depending on the boundary conditions, as follows [54]: 1) for $\alpha > 0.5$ and $\beta > 0.5$, $p_c = 0.5$; 2) $\alpha < 0.5$ and $\alpha < \beta$, $p_c = \alpha$; 3) $\beta < 0.5$ and $\beta < \alpha$, $p_c = 1 - \beta$. Figure 3.4 shows simulation results of the stochastic model, which fully coincide with theoretical calculations [54].

To move from the model system [54] to more realistic systems, the distribution of electron occupations for a chain is calculated, where hopping is allowed not only to/from the nearest V_o (Figure 3.5, left), and for systems with $T > 0$, where hopping is allowed in both directions (Figure 3.5, right). Note that for $\alpha > 0.5$ and $\beta > 0.5$ one still has $p_c = 0.5$ in the center, while for other values α, β one observes a decrease in p_c for $\alpha < \beta$ and an increase in p_c for $\beta < \alpha$.

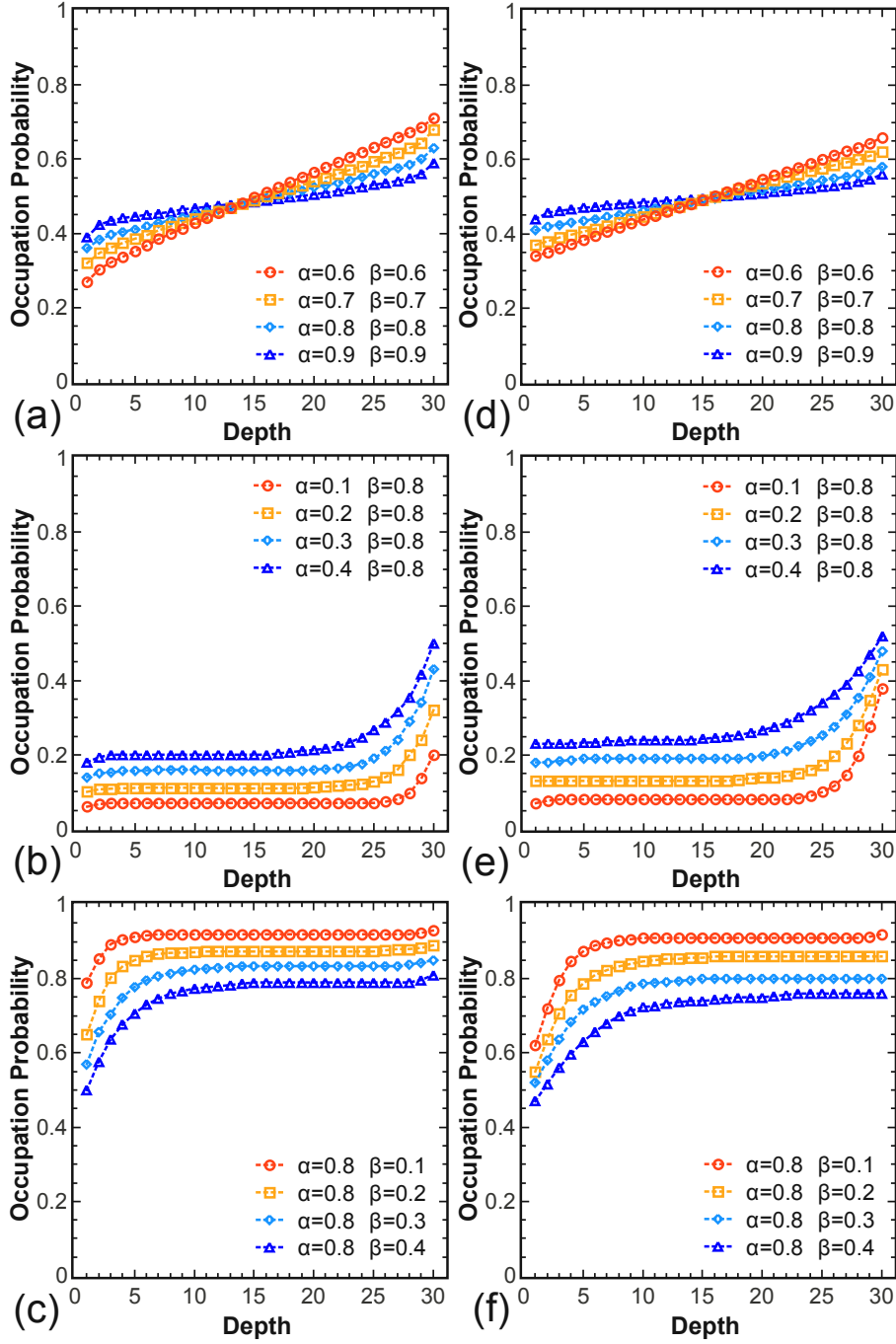


Figure 3.5: Calculated distribution of electron occupation probabilities (a,b,c) if unidirectional hopping is allowed not only to/from the closest V_o and (d,e,f) for hopping according to Equations 3.1-3.4 for $T > 0$: (a,d) $\alpha > 0.5$ and $\beta > 0.5$; (b,e) $\alpha < 0.5$ and $\alpha < \beta$; (c,f) $\beta < 0.5$ and $\beta < \alpha$.

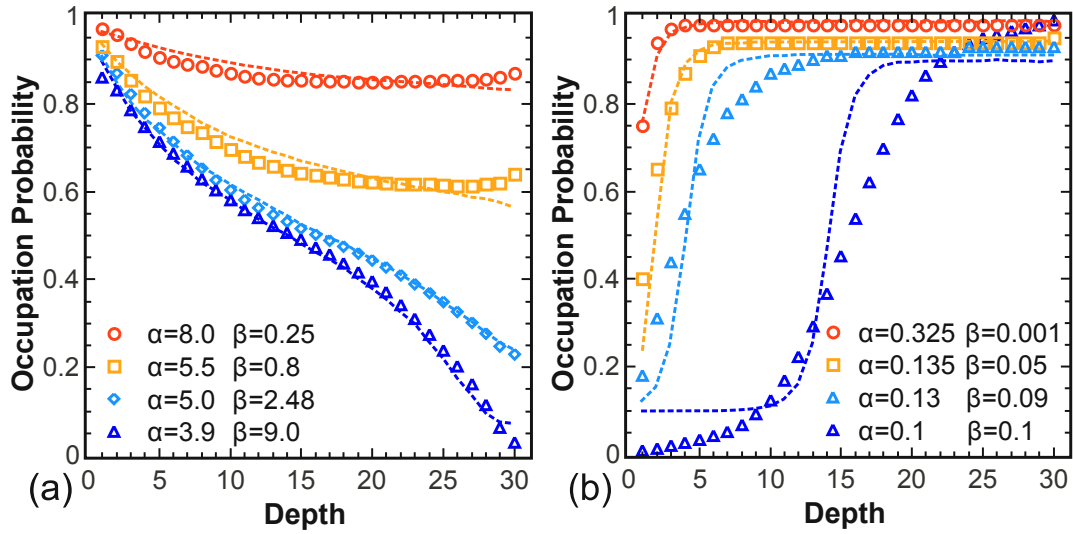


Figure 3.6: Calculated distribution of electron occupation probabilities under different biasing voltages. Lines are from [72], symbols are obtained from our stochastic model.

Next, the model is calibrated in a manner to reproduce the results reported in [72], for $V=0.4V$ to $V=1.6V$. Figure 3.6a shows a case, where the hopping rate between the electrodes and V_o is larger than the rate between the two V_o (i.e. $\alpha, \beta > 1$). In this case the low occupation region is formed near the anode, which according to [72] would correspond to an unipolar behavior. Figure 3.6b shows a case, where the hopping rate between the two V_o is larger than the rate between the electrodes and V_o (i.e. $\alpha, \beta < 1$). In this case the low occupation region is formed near the cathode, which would correspond to bipolar behavior [72].

In practice, the coefficients of the boundary conditions are determined by the material properties from which the electrode and the oxide-layer are made. The dependence of resistive switching on the electrode material was recently reported in research for TiO_2 [130] and ZrO_2 [156].

Modeling the temperature dependence

Following [72], the rupture of the conductive filament is possible only in the low electron occupation region. In order to simulate failures in switching from a state with low resistance to a state with high resistance for an elevated temperature, the dependence of the electron occupation distribution near the anode and the cathode for a system with $\alpha, \beta > 1$ (Figure 3.7a) and $\alpha, \beta < 1$ (Figure 3.7b) was calculated. In both types of systems the change is marginal amounting to less than 10% for a temperature increase from 300K to 475K. This result indicates high robustness of failure-free RRAM

switching from a state with low resistance to a state with high resistance for elevated temperature. At the same time it has been found that the measured decrease of switching time with increasing temperature reported in [72] stems from the increased mobility of oxide ions rather than from reduced occupations of V_o in the low occupation region.

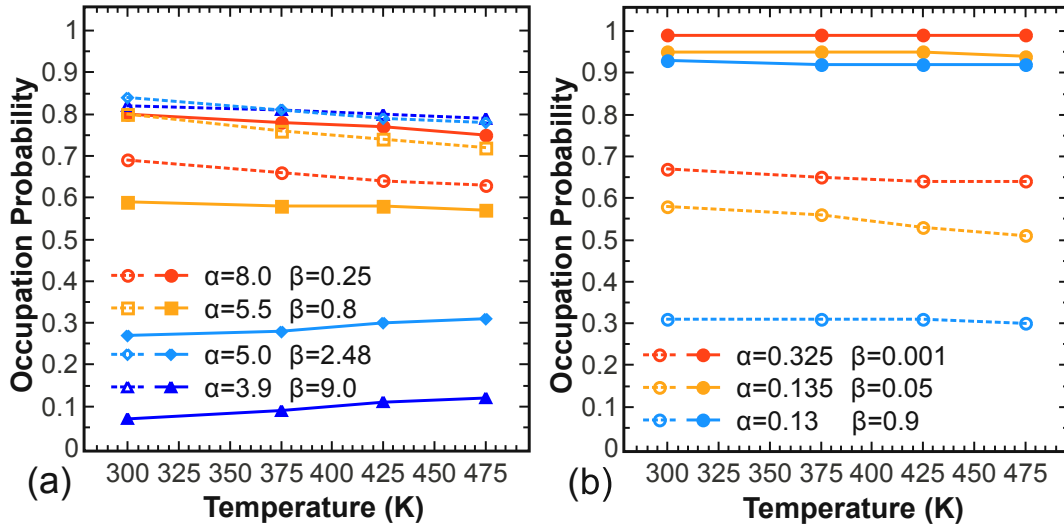


Figure 3.7: Temperature dependence of electron occupation probability near the anode (filled symbols) and the cathode (open symbols): (a) $\alpha, \beta > 1$; (b) $\alpha, \beta < 1$.

3.4.2 Modeling of the SET/RESET process

Single conductive filament devices

For the simulations a one-dimensional lattice consisting of thirty equivalent, equidistantly positioned hopping sites has been used. To simplify calculations the coefficients of the boundary conditions are assumed to be constant and equal to 0.1, independent of the applied voltage. In both simulations (SET and RESET process) the same formation/annihilation energy for V_o was used. For simulations the ratio A_i/A_e is equal to 10^{-3} . The result of the simulation of the SET process is shown in Figure 3.8.

To further demonstrate the capabilities of the model, the RESET $I-V$ characteristics for a single-CF device [72] was also simulated. For this purpose the conductive filament was modified in such a way that for each V_o an oxygen ion is placed nearby, to provide a possibility for the vacancies to annihilate. In the first moment of time all V_o are formed and assumed to be unoccupied by electrons. Electrons can enter/leave the system and hop from/to an electrode, respectively, or hop between two V_o according to the rules described above (Equations 3.1-3.4) Each O^{2-} has a probability Γ'_n (Equation 3.6) of annihilation with the nearest V_o if this V_o is not occupied by an electron. Figure 3.9

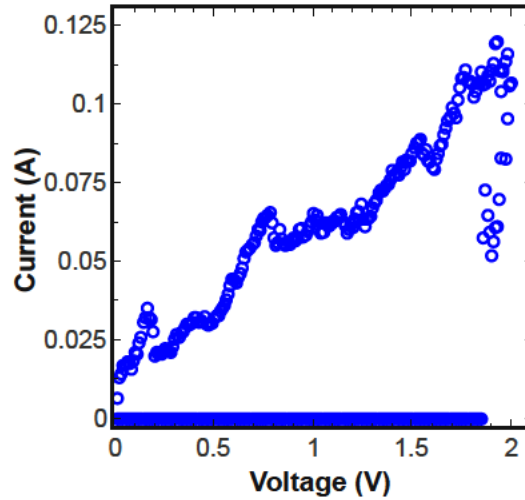


Figure 3.8: SET $I - V$ characteristics for a single-CF device are obtained from stochastic model.

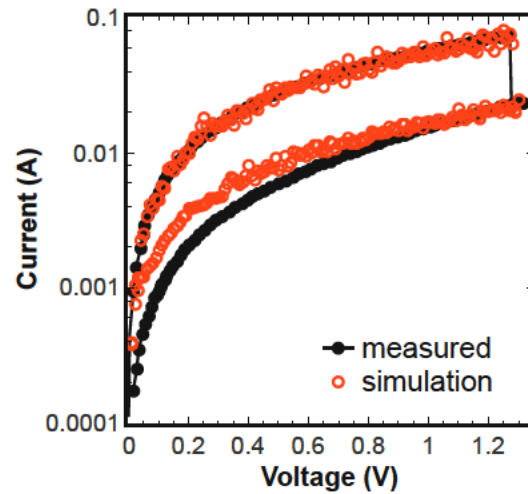


Figure 3.9: RESET $I - V$ characteristics for a single-CF device are obtained from stochastic model and measured results from [72].

shows the simulation result of the stochastic model, which is in good agreement with measurements from [72].

Multiple conductive filament devices

In real systems formation of several conductive filaments is possible. To allow this formation a two-dimensional lattice (2×30) is used now and the process of the resistive switching by applying a voltage V with a saw-tooth like time dependence is

investigated. The coefficients of the boundary conditions are constant and taken to be equal to 0.1.

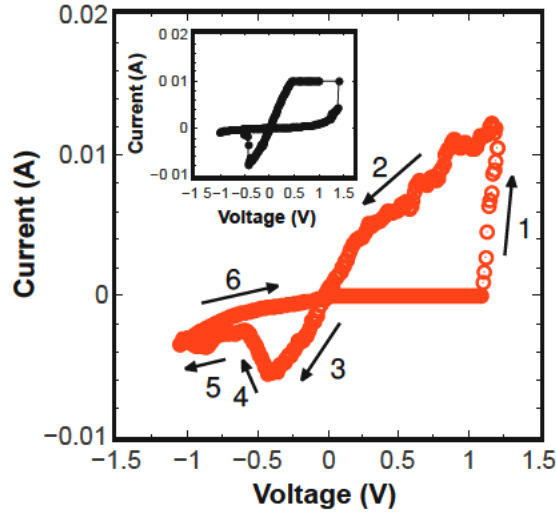


Figure 3.10: $I - V$ characteristics showing the hysteresis cycle obtained from our stochastic model ($\alpha = 0.1$ and $\beta = 0.1$). The inset shows the hysteresis cycle for M-ZnO-M from [149].

Figure 3.10 shows the $I - V$ obtained with the model system during a full cycle of switching from HRS to LRS and back. In the first moment of time it is assumed that there are no vacancies V_o in the system. If a positive voltage is applied, the formation of a conductive filament begins, when the voltage reaches a critical value sufficient to create V_o by moving O^{2-} to an interstitial position. During the SET and the RESET process each O^{2-} has a probability Γ'_n of moving to the nearest interstitial position (if this position is empty); moreover, each O^{2-} has a probability Γ'_n of annihilation with the nearest V_o , provided this V_o is not occupied by an electron. In addition, the dynamics of electrons according to (Equations 3.1-3.4) on the vacancies V_o already formed is taken into account giving rise to the electron current in the system. The formation of the conductive filament leads to a sharp increase in the current signifying a transition to a state with low resistance (Section 1 of the $I - V$ in Figure 3.10). If one continues applying the positive voltage, the number of V_o will continue to grow which in model can cause an unrecoverable breakdown of the insulator and further denial of switching to a state with high resistance. When a reverse negative voltage is applied, the current increases linearly, until the applied voltage reaches the value at which an annihilation of V_o is triggered by means of moving O^{2-} to V_o . The conductive filament is ruptured and the current decreases. This is the transition to the state with high resistance (Section 3 in Figure 3.10).

The simulated cycle is in agreement with the experimental cycle from [149] shown in inset of Figure 3.10.

Interestingly, for parameters different from those in Figure 3.10 ($\alpha = 0.135$, $\beta = 0.05$

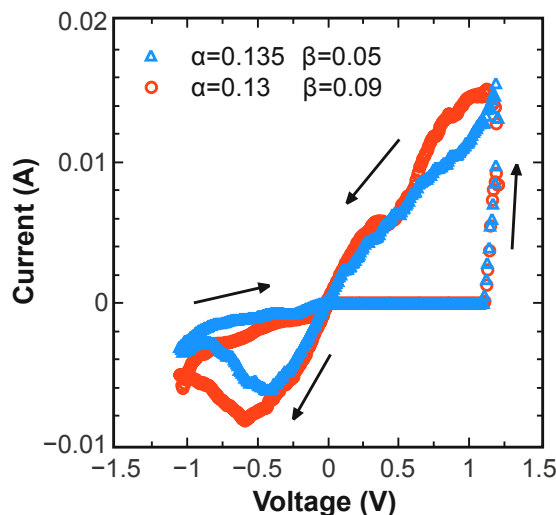


Figure 3.11: $I - V$ characteristics showing hysteresis cycles obtained from the stochastic model for different parameters α and β .

and $\alpha = 0.13$, $\beta = 0.09$) still sees a hysteresis cycle (Figure 3.11), although the region of low occupation which, according to [72], is responsible for the rupture of the conductive filament is almost absent. This result supports the observation that the ion dynamics is critical in describing the RRAM switching mechanism.

3.4.3 Hysteresis cycle modeling

Time dependence

Modeling of the resistive switching in this subsection and all calculations of RRAM $I - V$ characteristics are now performed on a 10×30 two-dimensional lattice. The modeling procedure is the same as described in the previous subsection 3.4.2. The coefficients of the boundary conditions are constant and taken to be equal to 0.1.

In order to investigate the dependence of the RESET process on time the same voltage amplitude V is applied but different time intervals are employed. A schematic illustration of the voltages V applied is shown in the inset in Figure 3.12. Results displayed in Figure 3.12 clearly indicate that the proper conductive filament rupture during the RESET process is achieved, when the product “voltage-time” is maximal.

Reproducible hysteresis in RRAM

For modeling multicycle $I - V$ characteristics a saw-tooth like voltage V has been used, where the product “voltage-time” is maximal from the previous subsection 3.4.3.

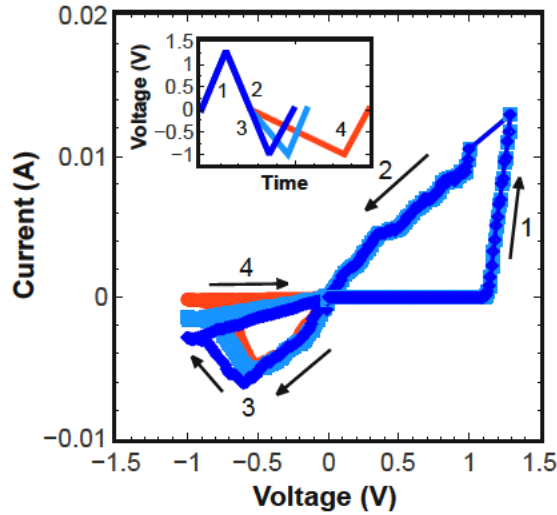


Figure 3.12: $I - V$ characteristics showing hysteresis cycles obtained from the stochastic model for different reset times ($\alpha = 0.1$ and $\beta = 0.1$). The inset shows a schematic illustration of voltage V applied.

Figure 3.13 shows the hysteresis cycle obtained from the generalized stochastic model after 5, 10, 15, and 20 cycles.

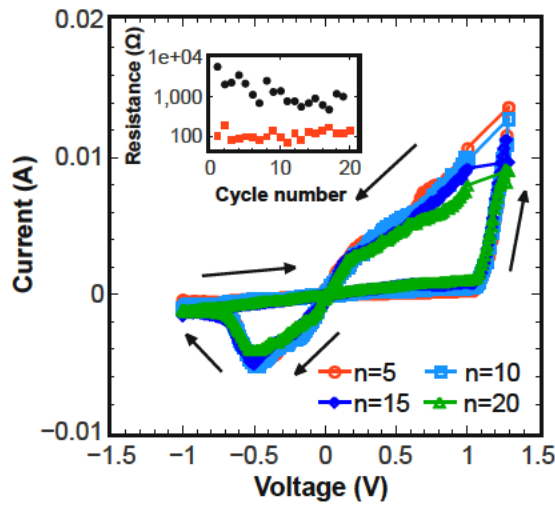


Figure 3.13: Multicycle $I - V$ characteristics showing the hysteresis cycle obtained from the stochastic model after 5, 10, 15, and 20 cycles. The inset shows the evolutions of resistance at HRS and LRS.

The generalized stochastic model allows enhancing RRAM endurance by properly tailoring the parameters of the cell. The mean attenuation of the hysteresis with the number of cycles indicates that the parameters used are close to optimal.

4 Magnetoresistive Memory

First suggestions for memory which uses magnetism for storage information were given in the 1950s. One of the first a so called magnetic core memory was proposed, where small magnetic toroids (ring of ferrite material) were used. Through these rings the wires for read and write information were threaded. Toroids can be magnetized either clockwise or anti-clockwise regarding the axis of rotation going through it. These two magnetization states are mapped to 0 and 1. This type of memory has been used as one of the first non-volatile methods for information storage. Magnetic core memory was widely used for almost 20 years until the advent of the semiconductor memory [204].

In 1969, Bobeck *et al.* [24] proposed a magnetic bubble memory, where information is stored in cylindrical domains or bubbles, each bubble storing one bit. The bubbles were created by a generator signal in a thin magnetic film, were pushed through the film in a racetrack by the external a magnetic field and detected by a sensor [222].

Nowadays, magnetic memory technology is represented by magnetoresistive RAM (MRAM) and spin transfer torque MRAM (STT-MRAM).

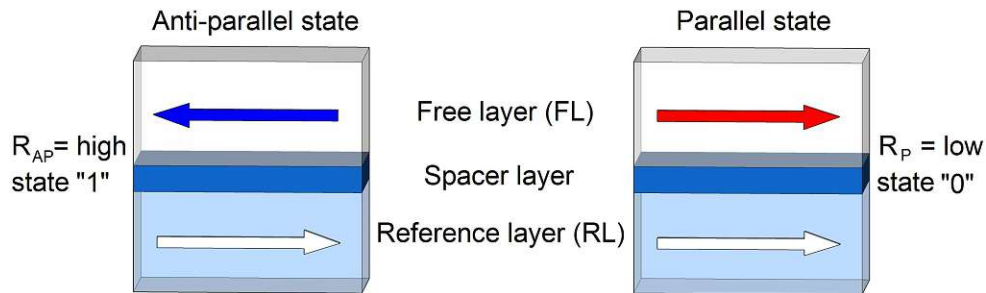


Figure 4.1: Schematic illustration of a magnetic pillar in a high resistance (left) and low resistance (right) state.

4.1 MRAM and STT-MRAM Basics

The basic element of a MRAM and STT-MRAM is a sandwich of two magnetic layers separated by a non-magnetic conducting spacer layer or a thin insulating layer. While the magnetization of the reference layer (RL) is fixed due to the fabrication process, the magnetization direction of the free layer (FL) can be switched between the two

states parallel and anti-parallel to the fixed magnetization direction. Anti-parallel and parallel states possess different magnetoresistances which are mapped to 0 and 1 (Figure 4.1).

4.1.1 Magnetoresistance phenomenon

The two most important magnetoresistance phenomena consists of the giant magnetoresistance (GMR) and the tunnel magnetoresistance (TMR) effect.

Giant magnetoresistance

In the late 1980s, Baibich *et al.* [7] and Binasch *et al.* [23] have independently observed GMR in Fe/Cr superlattices. GMR is detected in a pillar consisting from at least two ferromagnetic layers separated by a non-magnetic conducting spacer layer. The resistance of the pillar depends on the layers magnetization direction relative to each other.

To quantify the GMR effect the following ratio was introduced [262]:

$$GMR = \frac{R_{AP} - R_P}{R_P} = \frac{\rho_{AP} - \rho_P}{\rho_P} = \frac{\sigma_P}{\sigma_{AP}} - 1. \quad (4.1)$$

Here, R_{AP} and R_P are the resistances, ρ_{AP} and ρ_P are the resistivities, σ_{AP} and σ_P are conductivities in the high (anti-parallel) and low (parallel) resistance state, respectively. According to Equation 4.1 the GMR can be much larger than 1, if $\rho_{AP} > \rho_P$. An alternative definition the GMR less than 1 ($\rho_{AP} > \rho_P$) describes as [262]:

$$GMR' = \frac{\rho_{AP} - \rho_P}{\rho_{AP}} = 1 - \frac{\sigma_{AP}}{\sigma_P}. \quad (4.2)$$

In a first approximation one can assume that two independent channels of conductivity exist for electrons with “spin-up” and “spin-down” orientations [181]. The total current is the sum of the I_{\uparrow} current carriers with “spin-up” and the I_{\downarrow} current carriers with “spin-down”. If the currents I_{\uparrow} and I_{\downarrow} are flowing through the ferromagnetic layer with a fixed direction of magnetization (“up” or “down”), the resistance of the first and second groups of electrons differs.

The source of the GMR (Figure 4.2) is the unequal scattering of the two groups of electrons with different spin orientations with respect to the magnetization direction of the ferromagnetic layer [181]. If the magnetization direction of the ferromagnetic layers are the same (parallel state), the “spin-down” electrons (spin is anti-parallel to the magnetization) can propagate through the structure nearly unscattered, resulting - thereby in high electron conductivity and hence a low resistance. In contrast, in

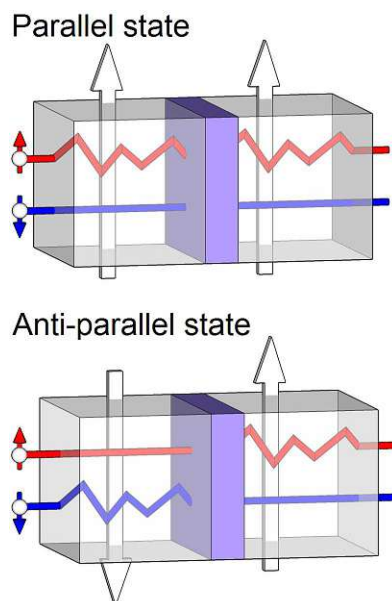


Figure 4.2: GMR effect in its simplest interpretation [35].

the anti-parallel state both “spin-up” and “spin-down” electrons undergo collisions in ferromagnetic layers, leading to a high resistance [35].

This technology was adopted for hard disk drive read heads and stimulated the new phase of research in magnetic memory, as GMR-based MRAM [227].

Tunnel magnetoresistance

In 1975, Julliere *et al.* discovered the phenomena of the tunnel magnetoresistance (TMR) in a Fe/Ge/Co junction at $T \leq 4.2\text{K}$ [111]. TMR is detected in a pillar consisting from two ferromagnetic layers separated by a thin insulating layer (magnetic tunnel junction (MTJ)). The resistance of the pillar, as in the GMR case, depends on the magnetization direction layers with respect to each other.

To quantify the TMR effect the following ratio is commonly used [102],[119]:

$$TMR = \frac{R_{AP} - R_P}{R_P}. \quad (4.3)$$

Here, R_{AP} and R_P are resistances in the high resistance state and the low resistance state, respectively.

The simplest interpretation of the TMR effect can be done as shown in Figure 4.3. The electrons with certain spin orientation (“spin-up” or “spin-down”) can tunnel from one ferromagnetic layer to another ferromagnetic layer through a non-conductive thin

insulating layer if there are available free states with the same spin orientation. In case of the parallel state, the majority spin (“spin-up”) electrons and minority spin (“spin-down”) electrons can easily tunnel to the second ferromagnetic layer and fill majority (“up”) and minority (“down”) states, respectively. This will result in the large conductance and corresponds to the low resistive state. In case of the anti-parallel state, the majority spin (“spin-down”) electrons and minority spin (“spin-up”) electrons from first ferromagnetic layer fill the minority (“down”) and majority (“up”) states in the second ferromagnetic layer, respectively. This will result in the low conductance and corresponds to the high resistive state.

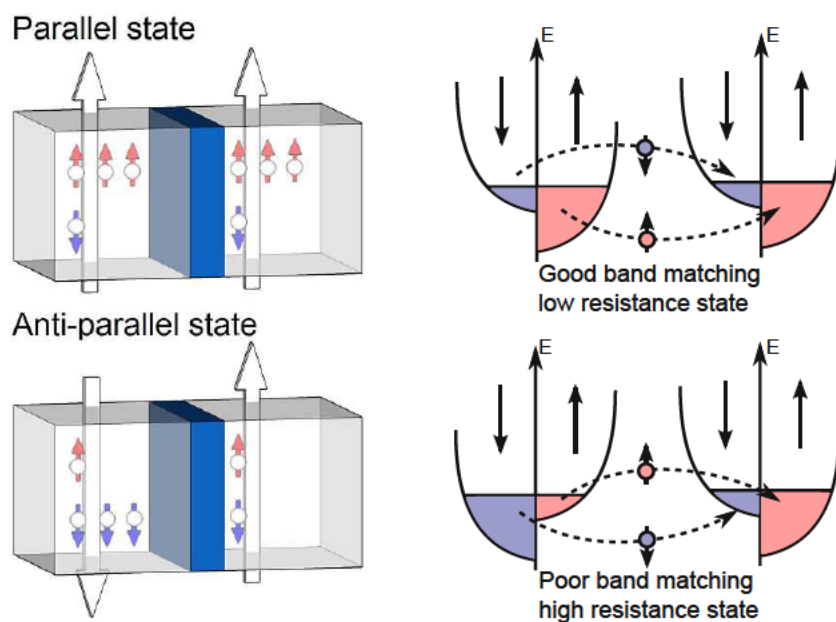


Figure 4.3: TMR effect in its simplest interpretation.

Despite the fact that the TMR effect was demonstrated earlier than GMR, its use in memory became possible only after observing large TMR in structures with amorphous Al_2O_3 tunnel barriers. First independent developments of structures with amorphous Al_2O_3 tunnel barriers were performed by Moodera *et al.* [169] and Miyazaki *et al.* [166]. The largest TMR ratio of an MTJ with amorphous Al_2O_3 is equal to 70.4% at room temperature and was demonstrated by Wang *et al.* [240], in 2004.

The next breakthrough in the development of magnetic memory was the discovery of a giant TMR in an epitaxially grown MTJ with MgO barrier. In 2001 a giant TMR in an MTJ with MgO barrier was independently predicted by Butler *et al.* [27] and Mathon *et al.* [164]. Mathon *et al.* [164] predicted the TMR ratio for an MgO barrier in excess of 1000%. By nature, this effect occurs from the symmetry-based spin filter effect in the MgO barrier [119]. The first experimental observation of TMR in Fe/MgO/FeCo(001) single-crystal epitaxial junctions was made by Bowen *et al.* [26]. The experiments showed a much smaller value of TMR (27% at 300K, 60% at 30K). In 2004 Parkin *et*

al. [179] and Yuasa *et al.* [261] demonstrated TMR in single-crystal Fe/MgO/Fe MTJs up to 220% and 180% at room temperature, respectively. The TMR of the epitaxial MTJ increased rapidly, thanks to the rapid progress in fabrication techniques [102]. In 2006, Yuasa *et al.* [260] have shown TMR up to 410%. In 2008, Ikeda *et al.* observed giant TMR effects up to 604% at room temperature and 1144% at 4.2K in junctions of Ta/Co₂₀Fe₆₀B₂₀/MgO/Co₂₀Fe₆₀B₂₀/Ta [100].

4.1.2 Magnetic pillar switching

In conventional field-induced MRAM the free layer magnetization switching is performed by applying a magnetic field (Figure 4.4). The writing operation is carried out by the current flowing through the wires. The currents generate a magnetic fields around the wires. Switching occurs in the cell only, if the magnetic fields from both currents are present at the magnetic pillar. This protects cells disposed along one of the wires from spontaneous switching. The current required for generating the magnetic field for the switching increases when the wire cross-section decreases, leading to the problem of scaling MRAM cells. Therefore, MRAM cells based on a magnetic field switching exhibit a scalability limit of about 90nm [204].

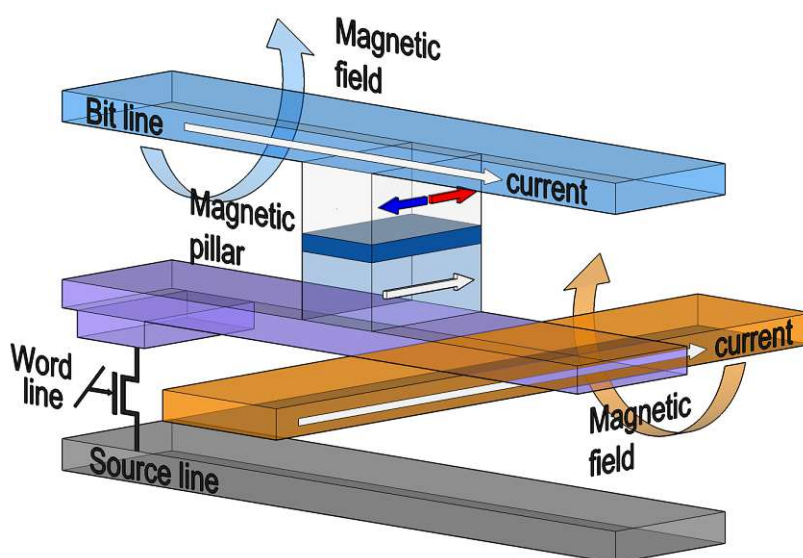


Figure 4.4: Schematic illustration of field-driven switching MRAM [204].

In contrast to field-induced MRAM, STT-MRAM does not require an external magnetic field. Switching between the two states occurs due to the spin transfer torque produced by the spin-polarized current flowing through the pillar (Figure 4.5). The theoretical prediction of the spin transfer torque effect was made independently by Slonczewski [217] and Berger [16]. In general, when electrons pass through the thick fixed magnetic layer, the spins of the electrons become aligned with the magnetization

of this layer. When these spin-polarized electrons enter the free layer, their spin orientations are getting aligned with the magnetization of the free layer within a transition layer of a few angstroms. Because of their spin orientation changed in the free layer, they exert a torque on the magnetization of the layer, which can cause magnetization switching, if the torque is large enough to overcome the damping. Smaller torque values result in magnetization precession around the effective magnetic field. By changing the current polarity the magnetization of the free layer can be switched from the anti-parallel to the parallel state and back with respect to the reference layer. In general, scalability is not a problem for the STT-MRAM cell, since reducing the size of the cell leads to a reduction in the current required for switching [204].

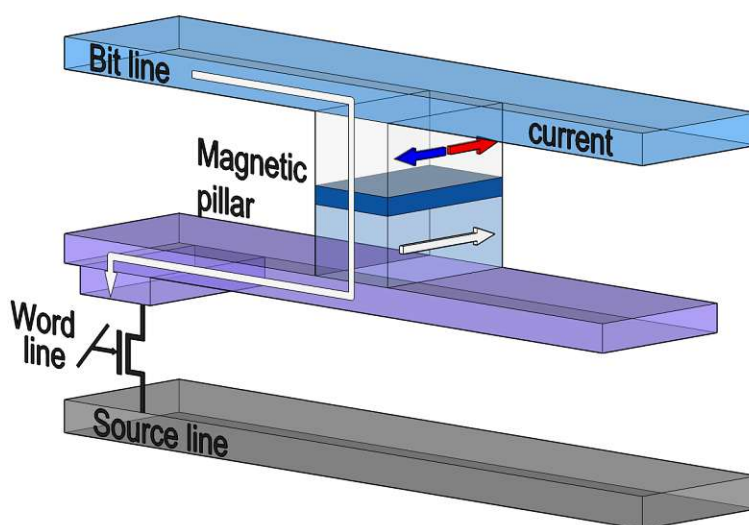


Figure 4.5: Schematic illustration of STT-MRAM switching [204].

The interest in MRAM has increased significantly after the observation of spin-torque induced switching on all-metallic stacks [204], which happened long after the theoretical prediction of this phenomena. GMR-based Co/Cu/Co was the first pillar where spin-torque induced switching [80],[117],[171],[219],[230] was shown. First AlO_x -based and MgO-based STT-MRAM cells were shown in 2004 [88] and 2005 [56], respectively.

4.2 In-Plane and Perpendicular Free Layer Magnetization

Depending on the orientation of the layer magnetizations the magnetic pillars can be divided into two categories (Figure 4.6): “perpendicular” with out-of-plane magnetization direction and “in-plane” with magnetization lying in the plane of the magnetic layer.

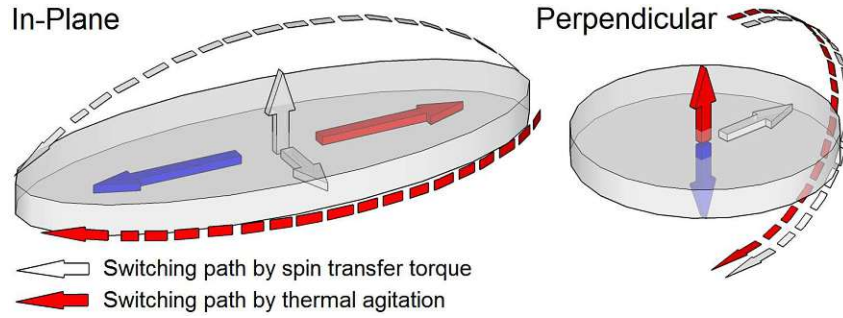


Figure 4.6: Schematic illustration of the free layer with a “perpendicular” magnetization (left) and “in-plane” magnetization direction (right).

4.2.1 Thermal stability factor

Switching of the magnetization can occur not only under the influence of the spin-polarized current, but also spontaneously due to thermal fluctuations (Figure 4.6). This is an unwanted event which leads to the loss of stored information. Thus, an important parameter of MRAM (STT-MRAM) is the thermal stability factor which is defined as the ratio of the thermal stability barrier to the operating temperature [101]:

$$\Delta = \frac{E_b}{k_B T}. \quad (4.4)$$

Here, E_b is the energy barrier that separates the two magnetization states, k_B is the Boltzmann constant, T is the temperature. The energy barrier is defined as $E_b = M_S H_K V / 2$ [101], where M_S is the saturation magnetization, H_K is effective anisotropy field, V is the volume of the free layer.

The thermal stability factor for perpendicular MTJs (p-MTJs) is given by the interface-induced perpendicular anisotropy field H_K^{perp} ($H_K = H_K^{perp} - 4\pi M_S$) as [3],[203]:

$$\Delta_{perp} = \frac{M_S \cdot (H_K^{perp} - 4\pi M_S) \cdot V}{2k_B T}. \quad (4.5)$$

To increase the thermal stability factor it is sufficient to increase the cross-section of p-MTJs, however, due to the domain formation, the cross-section is limited to approximately 70nm diameter, and, therefore, increasing the thermal stability factor of the single free layer p-MTJs above 40-50 is challenging [198],[199].

The thermal stability factor for in-plane MTJs is determined by the shape anisotropy field $H_K^{in-plane}$ ($H_K = H_K^{in-plane}$) [3],[203]:

$$\Delta_{in-plane} = \frac{M_S \cdot H_K^{in-plane} \cdot V}{2k_B T}. \quad (4.6)$$

Therefore, to increase the thermal stability factor it is sufficient to increase the thickness of the free layer and/or the aspect ratio between principal axes defining the elliptical cross-section.

4.2.2 Switching current

The (critical) switching current I_c is the current that is needed for switching the free layer from its actual magnetization direction to the opposite direction. However, it is not the switching current, but the switching current density counts, i.e. $J_c = I_c/A_{cs}$, where A_{cs} is the cross-section area of the free layer. The spin-polarized current is only a fraction of the total charge current flowing through the device. Therefore, high current densities from $\sim 10^7$ to $\sim 10^8$ A/cm² are required to switch the magnetization direction of the free layer, and the reduction of this required current density for switching is the most important engineering challenge for the STT-MRAM devices.

In p-MTJs the switching paths by spin transfer torque and thermal agitations (Figure 4.6, left) are the same. Thus, the critical switching current for p-MTJs is proportional to the thermal stability factor [3]:

$$I_c^{perp} = \frac{1}{\eta} \frac{2\alpha e \mu_0}{\hbar} \cdot M_S \cdot V \cdot (H_K^{perp} - 4\pi M_S) = \frac{1}{\eta} \frac{2\alpha e \mu_0}{\hbar} \cdot 2k_B T \Delta_{perp}. \quad (4.7)$$

Here, η is the polarizing factor [217],[30], α is the Gilbert damping parameter, e is the electron charge, μ_0 is the magnetic constant, \hbar is the reduced Planck constant.

In in-plane MTJs the switching under the influence of the spin current is following a different path than under the thermal agitations (Figure 4.6, right). Along this path the magnetization must get out of plane. This leads to an additional large term $2\pi M_S^2 V$ in the switching current [3]:

$$\begin{aligned} I_c^{in-plane} &= \frac{1}{\eta} \frac{2\alpha e \mu_0}{\hbar} \cdot M_S \cdot V \cdot (H_K^{in-plane} + 2\pi M_S) = \\ &= \frac{1}{\eta} \frac{2\alpha e \mu_0}{\hbar} \cdot (2k_B T \Delta_{in-plane} + 2\pi M_S^2 V), \end{aligned} \quad (4.8)$$

which results in a higher critical current compared to that in p-MTJs.

4.3 Magnetic Cell Architecture

Typical pillar designs for STT-MRAM cells are illustrated in Figure 4.7. In all the structures (except the Pr-MTJ (Figure 4.7e)) instead of layers with in-plane magnetization layers with perpendicular magnetization can be used. The spacer layer is made from a non-magnetic conducting material (in the case of the GMR-based devices) as well as insulating oxides.

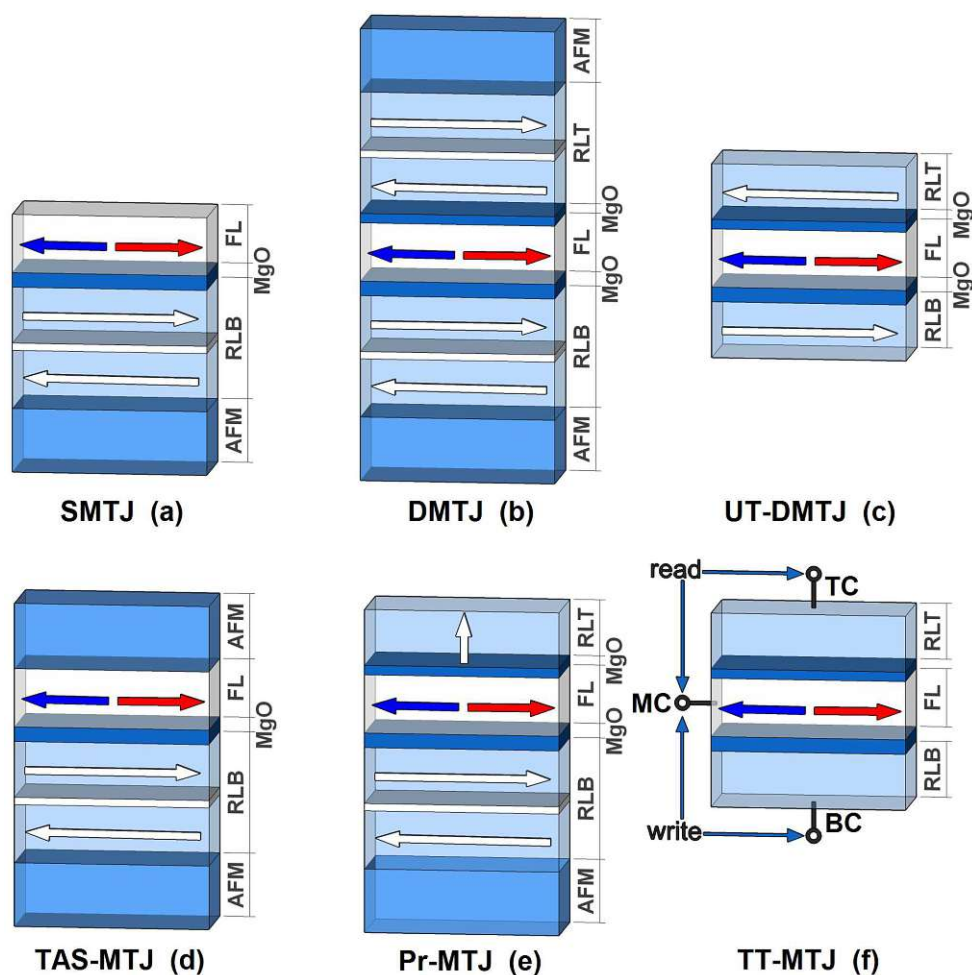


Figure 4.7: Magnetic memory cell designs: (a) SMTJ, (b) DMTJ, (c) UT-DMTJ, (d) TAS-MTJ, (e) Pr-MTJ, (f) TT-MTJ [119].

4.3.1 Single MTJ with one tunnel barrier

The single MTJ with one tunnel barrier (SMTJ) (Figure 4.7a) is the simplest structure. It consists of one reference layer, a spacer layer, and a free layer. The reference

layer should be more stable than the free layer in order to prevent the spontaneous switching of the reference layer during memory operations. The reference layer is made as a synthetic antiferromagnet (SAF). An SAF comprises two magnetic sublayers with opposite magnetizations separated by a thin ruthenium layer to provide a strong exchange coupling between the sublayers. At the same time, the opposing magnetizations of the sublayers allows to minimize the impact of magnetostatic influence of the reference layer onto the free layer. The reference layer is usually strengthened with direct exchange-bias coupling to an antiferromagnetic layer (AFM). The free layer can be formed as SAF, which leads to an increased thermal stability.

4.3.2 Dual MTJ with two barriers and ultra-thin dual MTJ cell

The dual MTJ with two barriers (DMTJ) (Figure 4.7b) is the structure consisting of the reference layer/spacer layer/free layer/spacer layer/reference layer [58],[66],[89]. During the switching process the second reference layer provides an extra spin-torque. In the anti-parallel configuration of the reference layers (the magnetizations of the two reference layers are anti-parallel), the spin currents from either of the reference layers exert torques in the same direction (full torque is the sum of the individual torques), while in the parallel configurations, the torques are in the opposite directions (full torque is the difference of the individual torques) [64]. Thus switching current can be reduced by almost 2 times [58] in the anti-parallel configuration.

A disadvantage of this structure is the reduced magnetoresistance. Since reference layers are in anti-parallel configuration, one part of the structure (a reference layer and the free layer) is always in a low resistance state while another part is in a high resistance state. This disadvantage can be easily solved by the use of different thicknesses of spacer layers or different materials for each of the spacer layers.

In order to reduce the overall thickness of the cell in ultra-thin dual MTJ (UT-DMTJ) (Figure 4.7c) each reference layer is not built as a SAF but as a single ferromagnetic layer. The magnetostatic interaction between them further strengthens the anti-parallel configuration of the reference layers.

4.3.3 Cell utilizing thermally assisted switching mechanism

Thermally assisted switching (TAS) mechanism is used in several designs of the magnetic cell [180]. In the first design of TAS cell a free layer composed from a ferromagnetic material with low Curie point was used [15],[46]. The free layer is heated close to the Curie temperature and after that is switched to a desired direction by applying a small magnetic field. In the second design an interface coupling between the antiferromagnetic layer and the ferromagnetic layer is used as the storage mechanism [46]. Both layers are heated above the Néel temperature and then cooled in the presence of a magnetic field in the write direction. The Néel temperature of the antiferromagnetic

material is lower than the Curie temperature of the ferromagnetic material. Thus, a relatively modest current is required to heat both layers above the Néel temperature. In principle, both these designs are covered by the structure shown in Figure 4.7d.

4.3.4 Cell utilizing precessional switching mechanism

The cell utilizing precessional switching mechanism (Pr-MTJ) (Figure 4.7e) is the structure in the form of the reference layer with the in-plane magnetization/spacer layer/free layer with the in-plane magnetization/spacer layer/reference layer with the perpendicular magnetization [118]. The reference layer with the in-plane magnetization is used for readout of the magnetic state of the free layer. The reference layer with the perpendicular magnetization is used for the switching operation. During the switching operation, the spin-torque from the reference layer with perpendicular magnetization affects the magnetization of the free layer causing the magnetization of the latter to tilt out of the plane. This leads to a large demagnetization field perpendicular to the plane of the free layer. This demagnetization field forces the magnetization of the free layer to precess about the direction normal to the free layer plane. Simulations of Pr-MTJ demonstrate that the switching time can be less than 50ps [118]. The switching time of 500ps [159] was demonstrated experimentally. Additional improvement of the design is still required to guarantee the necessary free layer final state [158].

4.3.5 Three-terminal MTJ cell

All of the above designs are made on two-terminal devices with writing based on the spin-polarized current and reading based on magnetoresistance (TMR or GMR). These two operations have different requirements for the device. For writing high spin-currents are needed. The memory cell is required to have the resistance around or below the CMOS field-effect transistor (FET) impedance to guarantee sufficient write current. However, for reading the memory cell resistance must be well above that of the FET impedance to improve the read signal [220].

For the solution of this difficulty a three-terminal MTJ cell (TT-MTJ) was proposed (Figure 4.7f) in which different paths are used for read and write operations [220]. As shown schematically in the Figure 4.7f additional terminal (middle contact (MC)) is connected to the free layer along with the usual terminals (top contact (TC) and bottom contact (BC)). The read operation is performed by applying a voltage between the TC and MC. Write operation is carried out by applying a voltage between the BC and MC [119].

4.4 Conclusions

MTJ-based STT-MRAM is widely recognized as the most promising candidate for future universal memory. There are two competing classes of MTJs with different directions of magnetization of the free layer: in-plane and perpendicular. Each of the classes has advantages, and disadvantages. Perpendicular MTJs with an interface-induced anisotropy show potential, but still require a reduction of damping and an increase of thermal stability. The in-plane MTJs exhibit a high thermal stability, but still require a reduction of the critical current density. Micromagnetic simulations significantly contribute to solving this problem through the optimization of STT-MRAM memory cells. In Chapter 7 a new design of the in-plane structure is presented.

5 Macro- and Micromagnetic Approach

5.1 Landau-Lifshitz-Gilbert Equation

In 1932, Bloch reported the first description of the time-dependent motion of uncoupled and undamped magnetic moments [136]. In 1935, Landau and Lifshitz [141] have proposed an equation describing the damped motion of the magnetization in a ferromagnet, known as the Landau-Lifshitz (LL) equation [17]:

$$\frac{d\mathbf{M}}{dt} = -\gamma [\mathbf{M} \times \mathbf{H}_{\text{eff}}] - \gamma \frac{\lambda}{M_S} [\mathbf{M} \times [\mathbf{M} \times \mathbf{H}_{\text{eff}}]]. \quad (5.1)$$

Here, \mathbf{M} is the magnetization, M_S is the saturation magnetization ($\mathbf{M} \cdot \mathbf{M} = M_S^2$), \mathbf{H}_{eff} is the effective magnetic field, λ is a phenomenological damping parameter, $\gamma = g|e|/2m_e$ is the gyromagnetic ratio, where g is the g-factor ($g=2$ for free electrons), e and m_e are the electron charge and mass, respectively.

The first term $-\gamma [\mathbf{M} \times \mathbf{H}_{\text{eff}}]$ in Equation 5.1 describes the magnetization precession around the effective magnetic field. This form of magnetic precession is easily obtained from the classical mechanical equation [136]

$$\frac{d\mathbf{P}}{dt} = \mathbf{L}, \quad (5.2)$$

which describes the rotation of a rigid body. Here, \mathbf{P} is the angular momentum and \mathbf{L} is the torque acting on the body. Then, using the magneto-mechanical ratio $\mathbf{J} = \gamma\mathbf{P}$ and substituting the magnetic torque $\mathbf{L} = [\mathbf{J} \times \mathbf{H}_{\text{eff}}]$ Equation 5.2 obtains the form:

$$\frac{d\mathbf{J}}{dt} = -\gamma [\mathbf{J} \times \mathbf{H}_{\text{eff}}]. \quad (5.3)$$

By dividing Equation 5.3 by magnetic constant μ_0 the equation is converted to the version of the Landau-Lifshitz equation for undamped rotation of the magnetization (Figure 5.1a):

$$\frac{d\mathbf{M}}{dt} = -\gamma [\mathbf{M} \times \mathbf{H}_{\text{eff}}]. \quad (5.4)$$

The second term in Equation 5.1 with the double vector product $-\frac{\gamma\lambda}{M_S} [\mathbf{M} \times [\mathbf{M} \times \mathbf{H}_{\text{eff}}]]$ was chosen based on purely phenomenological reasons that can be described as follows: (i) the damping process should lead the magnetization to the state with minimum energy (parallel to the effective field); (ii) the magnetization magnitude \mathbf{M} should remain constant (Figure 5.1b).

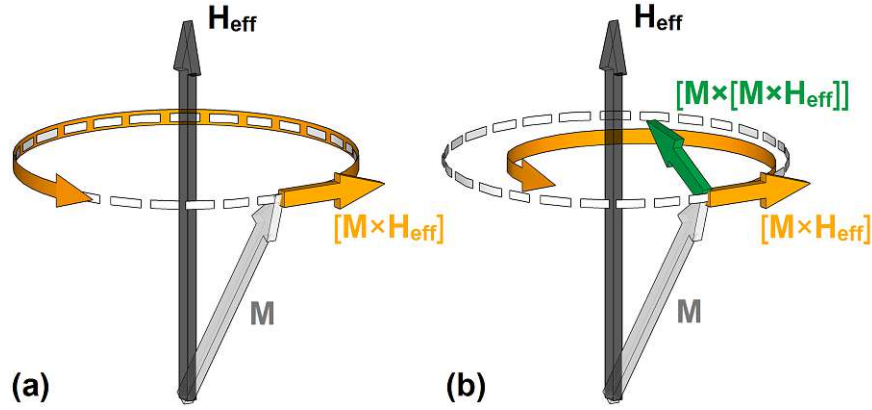


Figure 5.1: Illustration of the magnetization precession for (a) undamped motion and (b) motion with damping.

The Equation 5.1 could be used only in a case of small damping. In 1955, Gilbert proposed the equation which describes the strong damping in the thin films [77]:

$$\frac{d\mathbf{M}}{dt} = -\gamma \left[\mathbf{M} \times \left[\mathbf{H}_{\text{eff}} - \frac{\alpha}{\gamma M_S} \frac{d\mathbf{M}}{dt} \right] \right]. \quad (5.5)$$

Here, α is the Gilbert damping parameter. The Equation 5.5 is inconvenient to use, because it involves the time derivative of the magnetization $d\mathbf{M}/dt$ on both sides. By using algebraic manipulations, Equation 5.5 can be easily transformed into an explicit form

$$\frac{d\mathbf{M}}{dt} = -\frac{\gamma}{(1+\alpha^2)} [\mathbf{M} \times \mathbf{H}_{\text{eff}}] - \frac{\gamma}{(1+\alpha^2)} \frac{\alpha}{M_S} [\mathbf{M} \times [\mathbf{M} \times \mathbf{H}_{\text{eff}}]], \quad (5.6)$$

which gives us the Landau-Lifshitz-Gilbert (LLG) equation. LLG equation has the form of the LL equation if the gyromagnetic ratio γ in LL is replaced by $\gamma/(1+\alpha^2)$ and admit $\alpha = \lambda$. To get more numerically tractable version of the Equation 5.6, it is usually divided by M_S :

$$\frac{d\mathbf{m}}{dt} = -\frac{\gamma}{(1+\alpha^2)} [\mathbf{m} \times \mathbf{H}_{\text{eff}}] - \frac{\gamma}{(1+\alpha^2)} \alpha [\mathbf{m} \times [\mathbf{m} \times \mathbf{H}_{\text{eff}}]]. \quad (5.7)$$

Here, $\mathbf{m} = \mathbf{M}/M_S$ is the normalized vector of the magnetization.

5.2 Landau-Lifshitz-Gilbert-Slonczewski Equation

The LLG Equation 5.7 describes the MRAM switching by magnetic field. In order to be able to describe a switching in STT-MRAM, Equation 5.5 must be supplemented by an additional spin transfer torque term τ as follows [247],[267]:

$$\frac{d\mathbf{m}}{dt} = -\gamma [\mathbf{m} \times \mathbf{H}_{\text{eff}}] + \alpha \left[\mathbf{m} \times \frac{d\mathbf{m}}{dt} \right] + \frac{\gamma}{\mu_0 M_S} \tau, \quad (5.8)$$

which give us a more general version of the Landau-Lifshitz-Gilbert-Slonczewski (LLGS) equation. The Slonczewski's spin transfer torque term τ is [265]:

$$\tau = a(j) [\mathbf{m} \times [\mathbf{m} \times \mathbf{p}]] + b(j) [\mathbf{m} \times \mathbf{p}]. \quad (5.9)$$

Here, \mathbf{p} is the normalized vector of the fixed layer magnetization, $a(j)$ and $b(j)$ are the current-dependent functions for the in-plane and the perpendicular torque, respectively. Unlike TMR-based structures in GMR-based structure the perpendicular torque is insignificantly small in comparison to the in-plane torque, and can be neglected [247],[267].

5.2.1 Single reference layer structure

The numerically tractable version of LLGS Equation 5.8 is represented by [57],[105],[148]

$$\begin{aligned} \frac{d\mathbf{m}}{dt} = & -\frac{\gamma}{1+\alpha^2} ([\mathbf{m} \times \mathbf{H}_{\text{eff}}] + \alpha [\mathbf{m} \times [\mathbf{m} \times \mathbf{H}_{\text{eff}}]] - \\ & - \frac{\hbar j}{e M_S d} g(\Theta) (\beta [\mathbf{m} \times \mathbf{p}] - [\mathbf{m} \times [\mathbf{m} \times \mathbf{p}]])). \end{aligned} \quad (5.10)$$

Here, \hbar is the reduced Planck constant, j is the current density, d is the thickness of the free layer, $g(\Theta)$ is the Slonczewski's expression (Θ is the angle between the magnetization directions of the free and fixed layers), β is coefficient of the perpendicular torque which is usually taken to be equal α .

The LLGS Equation 5.10 is also often written in equivalent form [4],[30],[31],[64],[65],[163],[229],[248] as

$$\begin{aligned} \frac{d\mathbf{m}}{dt} = & -\frac{\gamma}{1+\alpha^2} ([\mathbf{m} \times \mathbf{H}_{\text{eff}}] + \alpha [\mathbf{m} \times [\mathbf{m} \times \mathbf{H}_{\text{eff}}]] + \\ & + \frac{g\mu_B j}{e\gamma M_S d} g(\Theta) (\beta [\mathbf{m} \times \mathbf{p}] - [\mathbf{m} \times [\mathbf{m} \times \mathbf{p}]])). \end{aligned} \quad (5.11)$$

Here, g is the g-factor, μ_B the Bohr magneton. Equivalence of the Equation 5.10 and Equation 5.11 is easily proven by expressing the gyromagnetic ratio for an isolated electron as $\gamma = -\frac{g\mu_B}{\hbar}$.

Figure 5.2 schematically illustrates the directions of the main terms of the LLGS equations. For switching the STT-MRAM the in-plane torque is the most important contribution and the perpendicular torque is neglected in Figure 5.2.

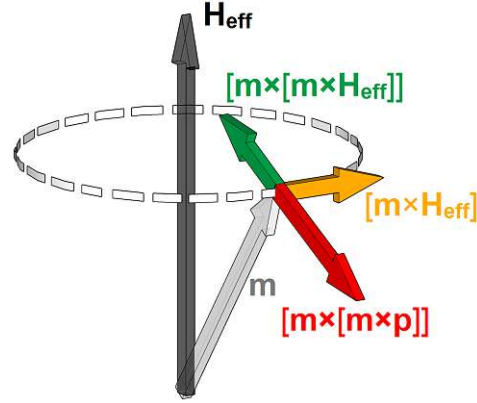


Figure 5.2: Illustration of the Landau-Lifshitz-Gilbert-Slonczewski equation for a structure with one reference layer.

The Slonczewski's expression $g(\Theta)$ depends on the spacer layer material, and for a non-magnetic conducting spacer layer it is expressed by [217]

$$g(\Theta) = [-4 + (1 + \eta)^3(3 + \cos(\Theta))/4\eta^{3/2}]^{-1}. \quad (5.12)$$

Here, η is the polarizing factor [217],[30]. For thin insulating spacer layer the Slonczewski's expression is represented by [218]

$$g(\Theta) = 0.5 \cdot \eta[1 + \eta^2 \cdot \cos(\Theta)]^{-1}. \quad (5.13)$$

5.2.2 Two reference layers structure

The structure with the two reference layer (penta-layer structure) was investigated theoretically [167],[168] by using the Green's function formalism combined with the free layer dynamics based on the LLG equation. A spin torque enhancement was found in the anti-parallel penta-layer (the magnetizations of the two reference layers are anti-parallel) as compared to the three-layer structure. However, this enhancement manifests itself only under dual barrier resonance tunneling conditions, when the current is high [167],[168]. At the same time, the aligned penta-layer configuration, when the magnetizations of the two reference layers are parallel to each other, was

found to have a fairly low spin torque efficiency and, as a consequence, it demands high switching currents [167],[168].

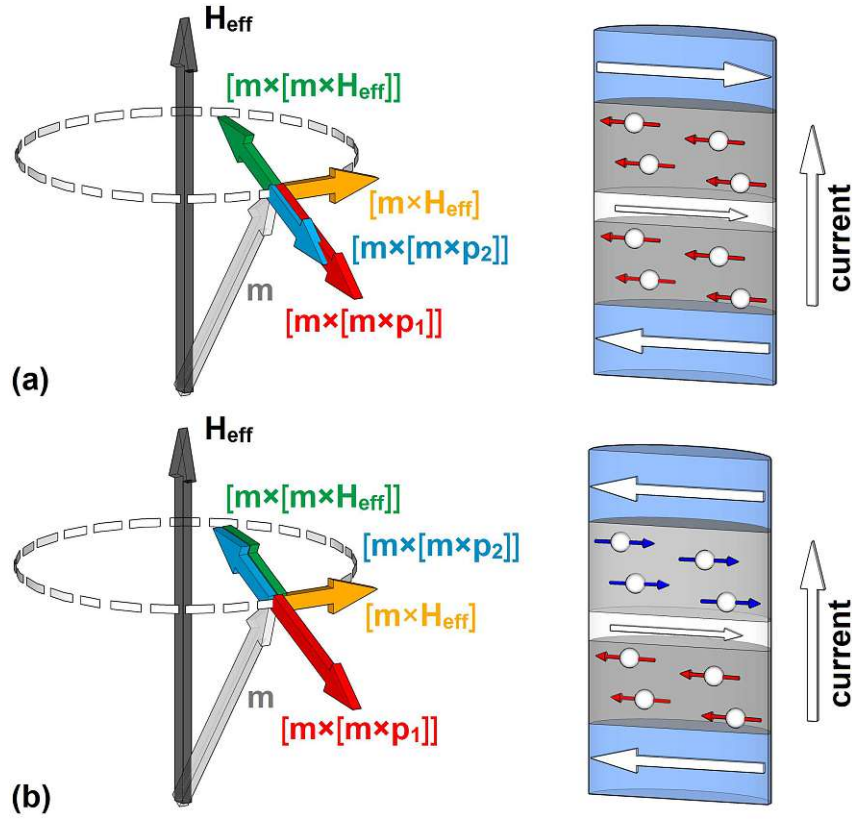


Figure 5.3: Illustration of the Landau-Lifshitz-Gilbert-Slonczewski equation for a structure with two reference layers in (a) anti-parallel configuration and (b) parallel configuration.

An alternative way of the penta-layer structure modeling (Figure 5.3) is an extension of the LLGS Equation 5.11 by adding a second spin transfer term:

$$\begin{aligned} \frac{d\mathbf{m}}{dt} = & -\frac{\gamma}{1+\alpha^2}([\mathbf{m} \times \mathbf{H}_{\text{eff}}] + \alpha [\mathbf{m} \times [\mathbf{m} \times \mathbf{H}_{\text{eff}}]]) + \\ & + \frac{g\mu_B j}{e\gamma M_S d} (g_1(\Theta_1) (\beta [\mathbf{m} \times \mathbf{p}_1] - [\mathbf{m} \times [\mathbf{m} \times \mathbf{p}_1]]) - \\ & - g_2(\Theta_2) (\beta [\mathbf{m} \times \mathbf{p}_2] - [\mathbf{m} \times [\mathbf{m} \times \mathbf{p}_2]])). \end{aligned} \quad (5.14)$$

Here, $g_1(\Theta_1)$ and $g_2(\Theta_2)$ are the Slonczewski's expressions defined by the first and the second spacer layer, respectively. Θ_1 (Θ_2) is the angle between direction of the magnetization of the free and the first (second) reference layer. The minus sign before the second spin transfer torque term is introduced because the direction of spin polarized

current is opposite with respect to two spacer layers. Indeed the penta-layer structure can be considered as combination of two three-layer structures with a shared free layer. Therefore, if one takes the current direction from the reference layer to the free layer as positive, then the current in the first three-layer structure and the current in the second three-layer structure flow always in opposite directions.

5.3 Effective Magnetic Field

The effective magnetic field is the functional derivative of the magnetic energy density ε , with respect to the magnetization \mathbf{m} [165]:

$$\mathbf{H}_{\text{eff}} = -\frac{1}{\mu_0 M_S} \frac{\delta \varepsilon}{\delta \mathbf{m}}. \quad (5.15)$$

The effective magnetic field contains the following contributions:

$$\mathbf{H}_{\text{eff}} = \mathbf{H}_{\text{ext}} + \mathbf{H}_{\text{exch}} + \mathbf{H}_{\text{ani}} + \mathbf{H}_{\text{demag}} + \mathbf{H}_{\text{ms}} + \mathbf{H}_{\text{current}} + \mathbf{H}_{\text{th}}. \quad (5.16)$$

Here, \mathbf{H}_{ext} is the external magnetic field, \mathbf{H}_{exch} is the exchange field, \mathbf{H}_{ani} is the magnetocrystalline anisotropy field, $\mathbf{H}_{\text{demag}}$ is the demagnetization field, \mathbf{H}_{ms} is the field due to magnetostatic coupling between the reference layer and the free layer, $\mathbf{H}_{\text{current}}$ is the Ampere field, and \mathbf{H}_{th} is the thermal field.

5.3.1 Exchange field

In magnetic materials the magnetic moments of the neighboring atoms are oriented in the same direction due to the exchange interaction. Relative deviations from the equilibrium orientations between neighboring moments causes an addition in exchange energy and are associated with non-parallel spin distributions. The expression for this energy can be written as [165]

$$E_{\text{exch}} = A \int_V [(\nabla \mathbf{m})^2] dV, \quad (5.17)$$

where A is the material dependent magnetic exchange constant. The magnetic exchange field associated with this energy can be calculated as [165]

$$\mathbf{H}_{\text{exch}} = \frac{2A}{\mu_0 M_S} \nabla^2 \mathbf{m}. \quad (5.18)$$

5.3.2 Anisotropy field

The magnetic anisotropy is a characteristic of a ferromagnetic material which describes the fact that the properties of the magnetic material are unequal in different directions, i.e. they depend on the direction in which the measurement is made.

The anisotropy has a number of possible sources such as the properties of the crystal lattice (magnetocrystalline anisotropy), the properties of the interface between two magnetic films (interface anisotropy), and the shape of the magnetic sample (shape anisotropy). The magnetocrystalline anisotropy can manifest itself in the form of a uniaxial or a cubic anisotropy, and it is described by the corresponding description of the anisotropy energy. The interface anisotropy, that is important for description of structures with perpendicular magnetization, is usually taken into account as a kind of uniaxial anisotropy. The shape anisotropy is defined by the energy of demagnetization.

Uniaxial anisotropy

The simplest case of magnetocrystalline anisotropy is the uniaxial anisotropy. The anisotropy energy in this case can be written as [165]

$$E_{ani} = - \int_V K_1 (\mathbf{m} \cdot \mathbf{n})^2 dV, \quad (5.19)$$

where K_1 is the material anisotropy coefficient, \mathbf{n} is the anisotropy axis. \mathbf{n} is the easy axis, if $K_1 > 0$ and \mathbf{n} is normal to the easy plane, if $K_1 < 0$.

The equation for calculating the anisotropy field [165] is

$$\mathbf{H}_{ani} = \frac{2K_1}{\mu_0 M_S} (\mathbf{m} \cdot \mathbf{n}) \mathbf{n}. \quad (5.20)$$

Cubic anisotropy

The anisotropy energy is described by the expression [165]

$$E_{ani} = \int_V [K_1 (m_x^2 m_y^2 + m_y^2 m_z^2 + m_z^2 m_x^2) + K_2 (m_x^2 m_y^2 m_z^2)] dV \quad (5.21)$$

for materials with cubic anisotropy in the case when the directions of the crystal axes coincide with the directions of the coordinate axes. Here, K_1 and K_2 are the material anisotropy coefficient.

The cubic anisotropy field in this case is calculated as

$$\mathbf{H}_{\text{ani}} = -\frac{2D}{\mu_0 M_S} \mathbf{m}, \quad (5.22)$$

where D is the matrix

$$D = \begin{bmatrix} K_1(m_y^2 + m_z^2) + K_2m_y^2m_z^2 & 0 & 0 \\ 0 & K_1(m_x^2 + m_z^2) + K_2m_x^2m_z^2 & 0 \\ 0 & 0 & K_1(m_x^2 + m_y^2) + K_2m_x^2m_y^2 \end{bmatrix}. \quad (5.23)$$

In cases when the crystal axes are rotated in space relative to the coordinate axes, then m_x , m_y , m_z in Equations 5.21–5.23 should be replaced by the projection of the magnetization vector \mathbf{m} to the corresponding axis of the crystal.

5.3.3 Demagnetization and magnetostatic field

The largest contribution to the effective magnetic field is provided by the demagnetization field $\mathbf{H}_{\text{demag}}$. The demagnetization force is responsible for the domain structure formation in the magnetic film, unlike the above-mentioned crystalline anisotropy and exchange interaction that are responsible for unidirectional magnetization of the magnetic film. In the case of crystalline anisotropy, the preferred direction for the magnetization is along the easy axes of the crystal. In the case of exchange interaction a single-domain state with an arbitrary orientation of magnetization is preferred.

The explicit expression for $\mathbf{H}_{\text{demag}}$ can be obtained from the Maxwell's equations through the definition of scalar auxiliary quantities, such as surface magnetic charge σ and volume magnetic charge ρ [2],[140],[165]:

$$\sigma = \mu_0 M_S (\mathbf{m} \cdot \mathbf{n}), \quad (5.24)$$

$$\rho = -\mu_0 M_S (\nabla \cdot \mathbf{m}). \quad (5.25)$$

Using such quantities the demagnetization field $\mathbf{H}_{\text{demag}}$ can be expressed from the scalar potential Φ_d of the stray field as

$$\mathbf{H}_{\text{demag}}(\mathbf{r}) = -\nabla \Phi_d(\mathbf{r}), \quad (5.26)$$

where $\Phi_d(\mathbf{r})$ is expressed as

$$\Phi_d(\mathbf{r}) = \frac{1}{4\pi\mu_0} \left[\int_V \frac{\rho(\mathbf{r}')}{|\mathbf{r} - \mathbf{r}'|} d^3r' + \int_S \frac{\sigma(\mathbf{r}')}{|\mathbf{r} - \mathbf{r}'|} d^2r' \right]. \quad (5.27)$$

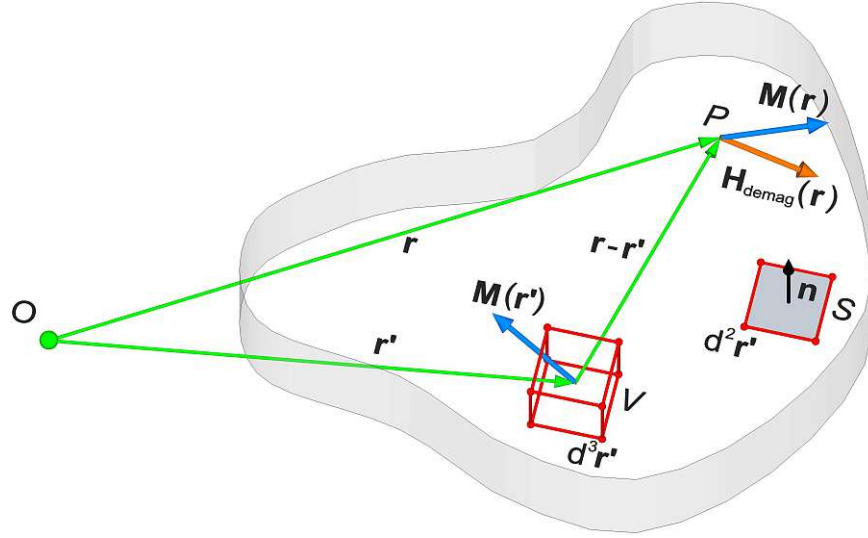


Figure 5.4: Geometry attached to Equation 5.28 [165].

Next, from Equations 5.24–5.27 the equation for calculating the demagnetization field $\mathbf{H}_{\text{demag}}$ acquires the form:

$$\mathbf{H}_{\text{demag}}(\mathbf{r}) = \frac{1}{4\pi\mu_0} \left[\int_V \frac{(\mathbf{r} - \mathbf{r}') \rho(\mathbf{r}')}{|\mathbf{r} - \mathbf{r}'|^3} d^3 r' + \int_S \frac{(\mathbf{r} - \mathbf{r}') \sigma(\mathbf{r}')}{|\mathbf{r} - \mathbf{r}'|^3} d^2 r' \right]. \quad (5.28)$$

In an alternative way, the demagnetization field $\mathbf{H}_{\text{demag}}$ can be obtained as a convolution of the magnetization \mathbf{m} and a kernel representing the dipole-dipole interaction [112]:

$$\mathbf{H}_{\text{demag},i}(\mathbf{r}) = \frac{M_S}{4\pi} \sum_j \int \frac{3r(i)r(j) - \delta_{ij}}{|\mathbf{r} - \mathbf{r}'|^3} \mathbf{m}_j(\mathbf{r}') d^3 r', \quad (5.29)$$

$$r(i) = \frac{\mathbf{r}_i - \mathbf{r}'_i}{|\mathbf{r} - \mathbf{r}'|}, \quad r(j) = \frac{\mathbf{r}_j - \mathbf{r}'_j}{|\mathbf{r} - \mathbf{r}'|}. \quad (5.30)$$

Here, $i, j = x, y, z$ are vector component.

The energy associated with the demagnetising field is given by [140]:

$$E_{\text{demag}} = -\frac{1}{2} \mu_0 M_S \int_V (\mathbf{H}_{\text{demag}} \cdot \mathbf{m}) dV. \quad (5.31)$$

Here, the demagnetization field $\mathbf{H}_{\text{demag}}$ could be calculated based on Equation 5.28 or Equation 5.29 and the prefactor 1/2 arises from the fact that the source of $\mathbf{H}_{\text{demag}}$ is the magnetization \mathbf{m} itself [2].

5.3.4 Ampere field

In case of the STT-MRAM, the current flowing through the free layer generates a magnetic field (Ampere's field), which must be taken into account when calculating the effective magnetic field \mathbf{H}_{eff} . It is to note that this contribution does not take part in field-induced switching MRAM and must be excluded from Equation 5.16 for the effective field calculation. The Ampere field can be calculated by the Bio-Savart's law [165]:

$$\mathbf{H}_{\text{current}} = \frac{1}{4\pi} \int_V \left[\mathbf{J}(\mathbf{r}') \times \frac{\mathbf{r} - \mathbf{r}'}{|\mathbf{r} - \mathbf{r}'|^3} \right] d^3r'. \quad (5.32)$$

Here, $\mathbf{J}(\mathbf{r}')$ is a current density vector.

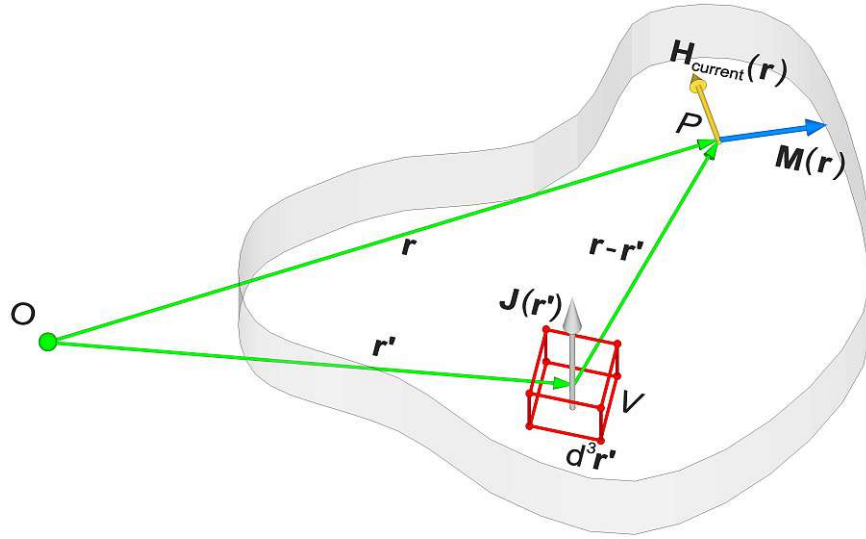


Figure 5.5: Geometry attached to Equation 5.32.

The energy associated with the Ampere field [165] is:

$$E_{\text{current}} = -\mu_0 M_S \int_V (\mathbf{H}_{\text{current}} \cdot \mathbf{m}) dV. \quad (5.33)$$

5.3.5 Thermal field

The thermal fluctuations of the magnetization occur in the magnetic film when it is heated. They can be described by the introduction of an auxiliary random magnetic field. The thermal field must satisfy the following statistical properties [65],[64]:

$$\langle H_{th,i}(t) \rangle = 0, \quad (5.34)$$

$$\langle H_{th,i}(t), H_{th,j}(t') \rangle = D\delta_{ij}\delta(t - t'), \quad (5.35)$$

where i and j are the coordinates x, y, z , the constant D measures the strength of the thermal fluctuations, and $\langle \rangle$ denotes an average taken over different realizations of the fluctuating field. The value of D is obtained from the Fokker-Planck equation [75]. According to Equations 5.34–5.35, the thermal field is uncorrelated in time and space, and \mathbf{H}_{th} is described by random Gaussian distributed numbers with zero mean value.

6 Numerical Implementation of Micromagnetic Approach

6.1 Space Discretization

In micromagnetics, the free layer of the pillar structure is divided by parallelepiped computational cells (Figure 6.1). Each computational cell ($\Delta V = \Delta x \Delta y \Delta z$) is represented by a unit magnetization vector $\mathbf{m} = (m_x, m_y, m_z)$, associated with the center of the cell. A computational cell corresponds to a uniform magnetic volume with the exchange parameter A , anisotropy constant K_1 (in a case of the uniaxial anisotropy) or K_1 and K_2 (in a case of the cubic anisotropy), damping parameter α , saturation magnetization M_S , and gyromagnetic ration γ . This parameters are the input for simulations. The dynamic of the computational cell is described by the LLG or LLGS equation, depending on the MRAM switching method.

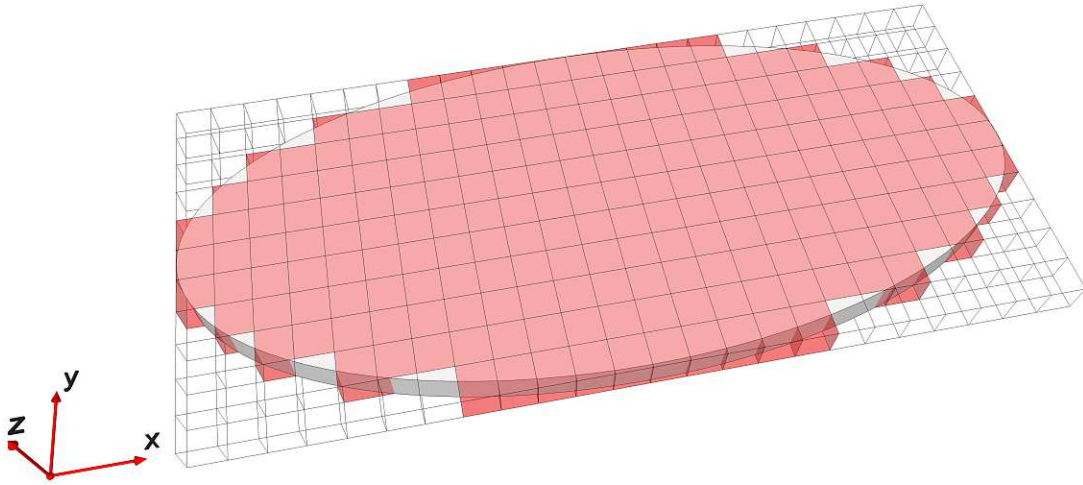


Figure 6.1: Discretization of the free layer with an elliptical cross-section.

The initial magnetization state of the free layer usually depends on the problem considered. In the simulations of the free layer switching, there are two possible initial states, defined as follows: (i) unidirectional magnetization of all cells (in the case of an ellipse, usually along the long axis); (ii) the equilibrium state, determined by the

external factors and the geometry of the free layer. Depending on the initial state, important parameters such as the MRAM switching time from one magnetization state to another will vary.

6.2 Magnetic Field Discretization

There are two main approaches to calculate the effective magnetic field: field-based and energy-based approaches. In the energy-based approach, the magnetic energy is calculated directly from the discretized magnetization and the effective magnetic field is obtained from resultant energy, as a cell-averaged field [165]. The effective magnetic field in the field-based approach is calculated directly from the discretized magnetization, and the energy is obtained from the magnetic field. In the implementation the field-based approach is used: for each computational cell and each time step, the effective field is calculated by Equation 5.16, and discretized as shown below.

6.2.1 External field

The external field is an input parameter for simulation and for the calculation of the effective magnetic field its value is directly added to the sum of calculated fields. The energy of a single computational cell associated with the external field can be obtained from:

$$E_{ext}(i, j, k) = -\mu_0 M_S (\mathbf{H}_{ext}(i, j, k) \cdot \mathbf{m}(i, j, k)) \Delta V. \quad (6.1)$$

6.2.2 Exchange field

For the exchange field one must know the magnetization direction in the nearest neighbor cells (in general 6 cells). The discretized exchange field is calculated based on [165]:

$$\mathbf{H}_{exch}(i, j, k) = \frac{2A}{\mu_0 M_S} \sum \frac{\mathbf{m}(i', j', k') - \mathbf{m}(i, j, k)}{\Delta^2}. \quad (6.2)$$

$\mathbf{m}(i', j', k')$ denotes a magnetization in the nearest neighbor cells (Figure 6.2), and Δ is the distance between the two magnetic moments (i.e. Δx or Δy or Δz). However, according to Equation 6.2 to determine the exchange field at the boundary cell (i.e. if there is no next neighbor cell) is a problem. The most common solution to this problem is to introduce a “ghost” magnetic vector at a missing location, with a value to be the same as the nearest magnetic vector at the boundary [165].

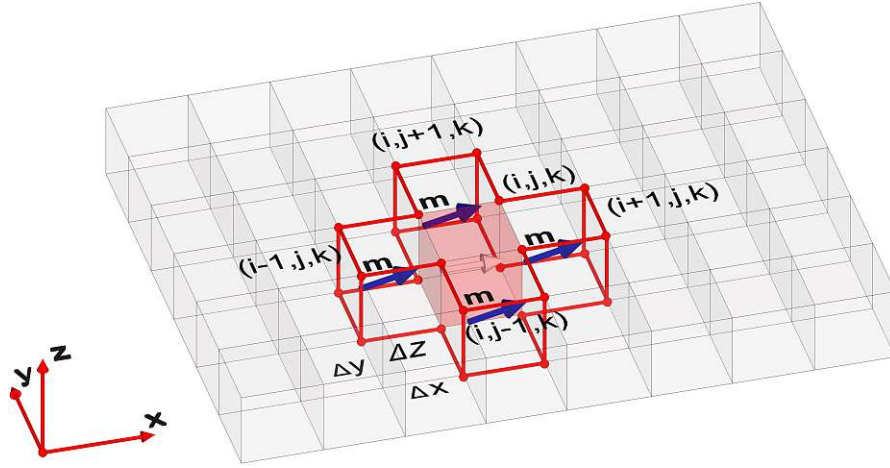


Figure 6.2: Exchange field calculation basics.

The energy of a single computational cell associated with the exchange field can be obtained from the equation:

$$E_{exch}(i, j, k) = -\frac{1}{2}\mu_0 M_S (\mathbf{H}_{exch}(i, j, k) \cdot \mathbf{m}(i, j, k)) \Delta V. \quad (6.3)$$

6.2.3 Magnetocrystalline anisotropy field

When calculating the discretized anisotropy field only the magnetization direction in the cell for which the calculation is made is taken into account. For each computational cell, the anisotropy field is calculated directly on the basis of the Equation 5.20 in the case of the uniaxial anisotropy, or on the basis of Equation 5.22 in the case of the cubic anisotropy. This gives us equations for the calculation, as shown below:

in the case of of the uniaxial anisotropy:

$$\mathbf{H}_{ani}(i, j, k) = \frac{2K_1}{\mu_0 M_S} (\mathbf{m}(i, j, k) \cdot \mathbf{n}) \mathbf{n}, \quad (6.4)$$

in the case of the cubic anisotropy:

$$\mathbf{H}_{ani}(i, j, k) = -\frac{2D(i, j, k)}{\mu_0 M_S} \mathbf{m}(i, j, k). \quad (6.5)$$

Here, $D(i, j, k)$ is the space-dependent matrix, which is calculated from Equation 5.23. For both cases, the energy of a single computational cell associated with the anisotropy field can be obtained from the equation:

$$E_{ani}(i, j, k) = -\frac{1}{2}\mu_0 M_S (\mathbf{H}_{ani}(i, j, k) \cdot \mathbf{m}(i, j, k)) \Delta V. \quad (6.6)$$

6.2.4 Demagnetization and magnetostatic field

The most difficult and time consuming, compared to the anisotropy field and the exchange field, is the calculation of the demagnetization field. While in the calculation of the exchange field the magnetization must be considered only in the nearest neighbor computational cells and for the calculation of the anisotropy field it is necessary to know the magnetization in a computational cell for which the calculations of the field is made, in order to calculate the demagnetization field the iteration of the magnetizations of each computational cell with the magnetization of each computational cell must be considered. Thus, the calculation of the demagnetization field occupies most of the CPU time spent for each computational time-step.

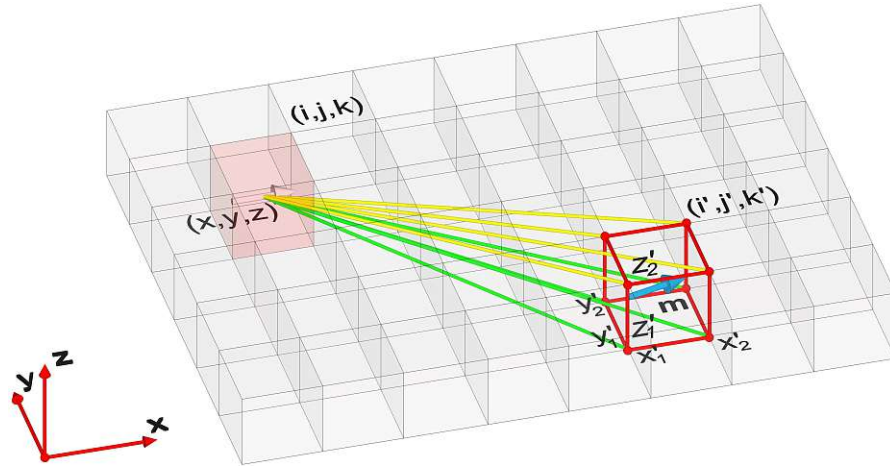


Figure 6.3: Demagnetization field calculation basics.

In the implementation the demagnetization field calculation based on the discretization of the Equation 5.29 is used. The resulting demagnetization field for each computational cell is calculated as the sum of the individual demagnetization contributions of the magnetization of all cells:

$$\mathbf{H}_{demag}(i, j, k) = \frac{M_S}{4\pi} \sum_{i'=1}^{N_x} \sum_{j'=1}^{N_y} \sum_{k'=1}^{N_z} (G(i, j, k, i', j', k') \cdot \mathbf{m}(i', j', k')). \quad (6.7)$$

Here, N_x , N_y , N_z are the grid dimensions in x , y , z direction, respectively, and $G(i, j, k, i', j', k')$ is a space-dependent matrix of the interaction coefficients. To determine this matrix, the quantities $\rho = \sqrt{u^2 + v^2 + w^2}$, $P_u = \arctan\left(\frac{vw}{u\rho}\right)$, $L_u =$

$-\ln(u + \rho)$ are introduced. P_v, P_w, L_v, L_w can be obtained through permutation of the variables u, v, w . These quantities are obtained on the basis of generalization of the equations for fast calculations of the integrals. The derivation of the equations for fast calculations of integrals is described in [112].

Eventually the required matrix $G(i, j, k, i', j', k')$ is obtained based on [112] (Figure 6.3):

$$G(i, j, k, i', j', k') = C(i, j, k, i', j', k') \Big|_{u=x-x'_1}^{u=x-x'_2} \Big|_{v=y-y'_1}^{v=y-y'_2} \Big|_{w=z-z'_1}^{w=z-z'_2}, \quad (6.8)$$

where

$$C(i, j, k, i', j', k') = \begin{bmatrix} P_u & L_w & L_v \\ L_w & P_v & L_u \\ L_v & L_u & P_w \end{bmatrix}. \quad (6.9)$$

It is to note that the matrix is symmetric, so only 6 of 9 elements of the matrix need to be calculated. Since the matrix is time-independent, it is possible to carry out the calculation only once.

The energy of a single computational cell associated with the demagnetization field can be obtained from the equation:

$$E_{demag}(i, j, k) = -\frac{1}{2}\mu_0 M_S (\mathbf{H}_{demag}(i, j, k) \cdot \mathbf{m}(i, j, k)) \Delta V. \quad (6.10)$$

The magnetostatic coupling between the reference layer and the free layer $\mathbf{H}_{ms}(i, j, k)$ is calculated based on an equation similar to Equation 6.7:

$$\mathbf{H}_{ms}(i, j, k) = \frac{M_S}{4\pi} \sum_{i'=1}^{NP_x} \sum_{j'=1}^{NP_y} \sum_{k'=1}^{NP_z} (G(i, j, k, i', j', k') \cdot \mathbf{p}(i', j', k')). \quad (6.11)$$

To do this, a reference magnetic layer is conditionally divided into parallelepiped elementary cells with magnetization $\mathbf{p} = \frac{\mathbf{M}_p}{M_{Sp}}$, where \mathbf{M}_p and M_{Sp} are the local magnetization and saturation magnetization of the reference layer, respectively. In Equation 6.11, $G(i, j, k, i', j', k')$ is calculated based on Equation 6.8, where NP_x, NP_y, NP_z are the grid dimensions in x, y, z directions, and in the implementation $NP_x = N_x, NP_y = N_y$, and $NP_z \geq N_z$ due to the thickness of the reference layer is typically greater than the thickness of the free layer. When the magnetization of the reference layer does not change with time, this field must be calculated only once.

The energy of a single computational cell associated with the magnetostatic coupling between the reference layer and the free layer can be obtained from the equation:

$$E_{ms}(i, j, k) = -\mu_0 M_S (\mathbf{H}_{ms}(i, j, k) \cdot \mathbf{m}(i, j, k)) \Delta V. \quad (6.12)$$

In contrast to the demagnetization energy, one should not take the prefactor 1/2 for energy of the magnetostatic coupling between the reference layer and the free layer, since the source of the \mathbf{H}_{ms} in a free layer is the magnetization of the reference layer.

6.2.5 Ampere field

In the implementation the Ampere field calculation based on the discretization of the Equation 5.32 is used. Since the integrand (Equation 5.32) of the Ampere field coincides with the integrand of the volume magnetic charge in the demagnetization field calculation (Equation 5.28), the equations for fast calculations of integrals proposed in [228] are used for the demagnetization field.

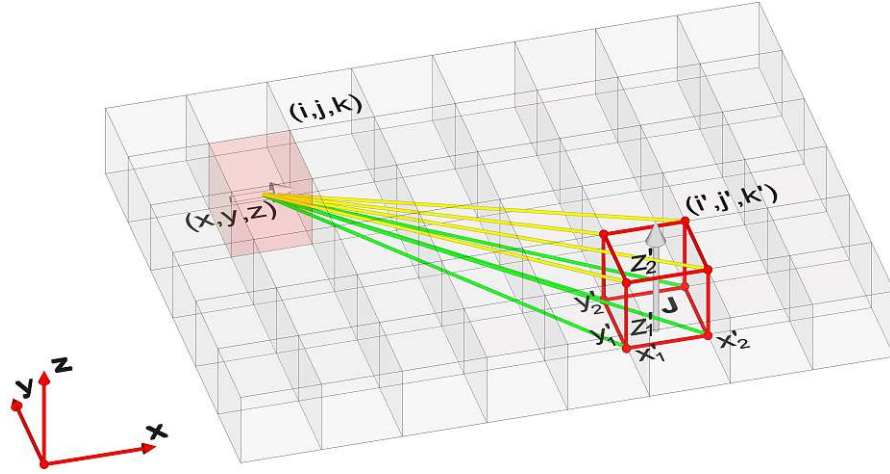


Figure 6.4: Ampere field calculation basics.

The resulting Ampere field for each computational cell is calculated as the sum of the individual Ampere field contributions due to the current flowing through each cell:

$$\mathbf{H}_{\text{current}}(i, j, k) = \frac{1}{4\pi} \sum_{i'=1}^{N_x} \sum_{j'=1}^{N_y} \sum_{k'=1}^{N_z} [\mathbf{J}(i', j', k') \times \mathbf{G}'(i, j, k, i', j', k')], \quad (6.13)$$

except for the cell at which this field is computed, i.e. $i' \neq i$ or $j' \neq j$ or $k' \neq k$. In Equation 6.13, $\mathbf{J}(i', j', k')$ is the current density vector and $\mathbf{G}'(i, j, k, i', j', k')$ is the space-dependent vector of the interaction coefficients. To determine this vector, quantities ρ and P_u similar to the quantities, used for calculation of the demagnetization

field (see above) are introduced, and $L'_u = \frac{1}{2} \ln \left(\frac{\rho+u}{\rho-u} \right)$. P_v, P_w, L'_v, L'_w can be obtained through the permutation of the variables u, v, w . Eventually the required vector $\mathbf{G}'(i, j, k, i', j', k')$ is obtained based on [228] (Figure 6.4):

$$\mathbf{G}'(i, j, k, i', j', k') = \mathbf{C}'(i, j, k, i', j', k') \Big|_{\substack{u=x-x'_2 \\ u=x-x'_1}}^{\substack{v=y-y'_2 \\ v=y-y'_1}} \Big|_{\substack{w=z-z'_2 \\ w=z-z'_1}}, \quad (6.14)$$

where

$$\mathbf{C}'(i, j, k, i', j', k') = \begin{bmatrix} uP_u - vL'_w - wL'_v \\ vP_v - wL'_u - uL'_w \\ wP_w - uL'_v - vL'_u \end{bmatrix}. \quad (6.15)$$

If one assumes that the current does not change with time, then the Ampere field must be calculated only once. Figure 6.5 shows an example of the Ampere field calculated for free layers with different cross-section.

The energy of a single computational cell associated with the Ampere field can be obtained from the equation:

$$E_{current}(i, j, k) = -\mu_0 M_S (\mathbf{H}_{current}(i, j, k) \cdot \mathbf{m}(i, j, k)) \Delta V. \quad (6.16)$$

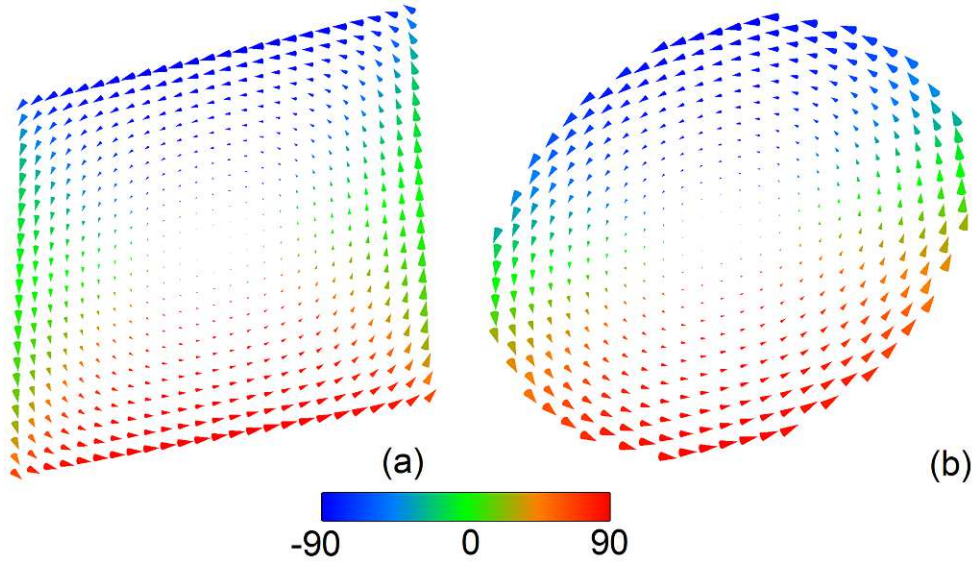


Figure 6.5: Direction of Ampere field in a free layer with: (a) square cross-section and (b) circular cross-section. The size of vector is normalized to its maximum value in each case. The color shows the angle between the vector of the Ampere field and the y -axis.

6.2.6 Thermal field

When calculating the discrete thermal field only the cell for which the calculation is made is taken into account [103]:

$$\mathbf{H}_{th}(i, j, k) = \sigma(i, j, k) \sqrt{\frac{\alpha}{1 + \alpha^2} \frac{2k_B T}{\gamma \Delta V \Delta t M_S}}. \quad (6.17)$$

Here, $\Delta V = \Delta x \Delta y \Delta z$ is the volume of the divided cell, Δt is the time step, $\sigma(i, j, k) = (\sigma_x, \sigma_y, \sigma_z)$ is a Gaussian random uncorrelated function with standard deviation equal 1.

The energy of a single computational cell associated with the thermal field can be obtained from the equation:

$$E_{th}(i, j, k) = -\mu_0 M_S (\mathbf{H}_{th}(i, j, k) \cdot \mathbf{m}(i, j, k)) \Delta V. \quad (6.18)$$

6.3 Time Discretization

The integration of LLG (LLGS) equation is done by using a fourth-order Runge-Kutta algorithm with a constant time step Δt . The new value of the magnetization at time $t + \Delta t$ is derived based on the magnetization value at time t as:

$$m(t + \Delta t) = m(t) + (k_1 + 2k_2 + 2k_3 + k_4)/6, \quad (6.19)$$

where

$$k_1 = f(m, t) \Delta t, \quad (6.20)$$

$$k_2 = f\left(m + \frac{k_1}{2}, t + \frac{\Delta t}{2}\right) \Delta t, \quad (6.21)$$

$$k_3 = f\left(m + \frac{k_2}{2}, t + \frac{\Delta t}{2}\right) \Delta t, \quad (6.22)$$

$$k_4 = f(m + k_3, t + \Delta t) \Delta t. \quad (6.23)$$

Here, $f(m, t)$ is an integrable equation, i.e. LLG or LLGS.

Summarizing all described above the flowchart of the micromagnetic simulation is presented on Figure 6.6.

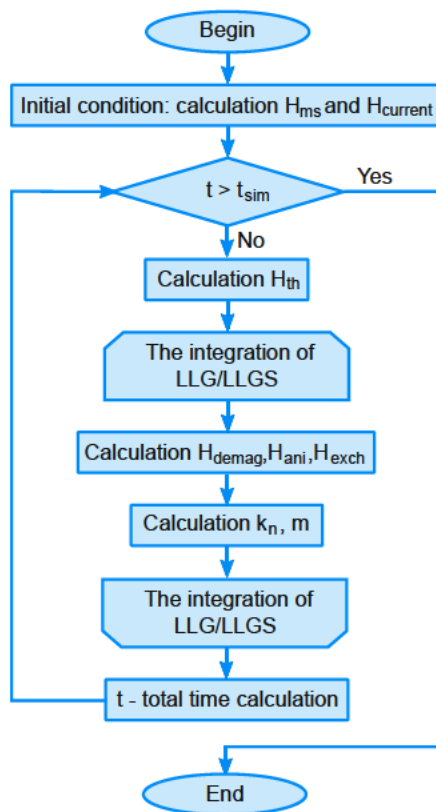


Figure 6.6: Flowchart of the micromagnetic simulation.

6.4 Energy Calculation

The full energy of a single computational cell is the sum of the corresponding contributions:

$$E_{cell}(i, j, k) = E_{ext}(i, j, k) + E_{exch}(i, j, k) + E_{ani}(i, j, k) + E_{demag}(i, j, k) + E_{ms}(i, j, k) + E_{th}(i, j, k) + E_{current}(i, j, k). \quad (6.24)$$

The total energy of the free layer is the sum of full energies of every computational cell:

$$E_{tot} = \sum_{i=1}^{N_x} \sum_{j=1}^{N_y} \sum_{k=1}^{N_z} E_{cell}(i, j, k). \quad (6.25)$$

To check the correctness of the calculation of the main contributions to the total energy (demagnetization, magnetocrystalline anisotropy and exchange energy) one of the basic test problems is solved, namely, the problem of the two magnetization states of the cube [93]: “flower” and “vortex” state (Figure 6.7).

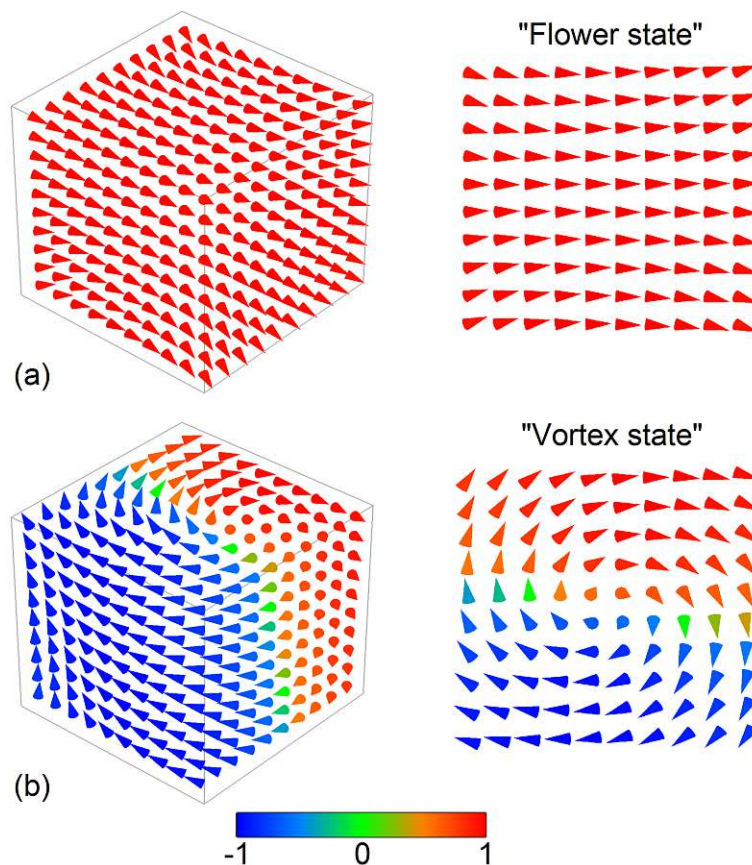


Figure 6.7: Magnetization states of the cube: (a) flower and (b) vortex. The color shows the direction of magnetization along the easy magnetocrystalline axis (x -axis).

The problem is to calculate the single domain limit of a cube, i.e. the length of the cube edge where the two magnetization states have the same total energy. The problem is material independent, so the energy density is expressed in quantities of $K_m = \frac{1}{2}\mu_0 M_S^2$ and the length of the cube edge in $l_{ex} = \sqrt{\frac{A}{K_m}}$, where M_S is the saturation magnetization and A is the material exchange constant. The material anisotropy coefficient K is taken equal to $0.1K_m$, and the easy axis is directed parallel to a principal axis of the cube. Different states for the cube magnetization are obtained by calculation of the magnetization relaxation based on LLG equation with different initial magnetization direction. For the “flower state” the initial magnetization direction should be along the easy anisotropy axis, and for the “vortex state” it should be perpendicularly to the easy axis.

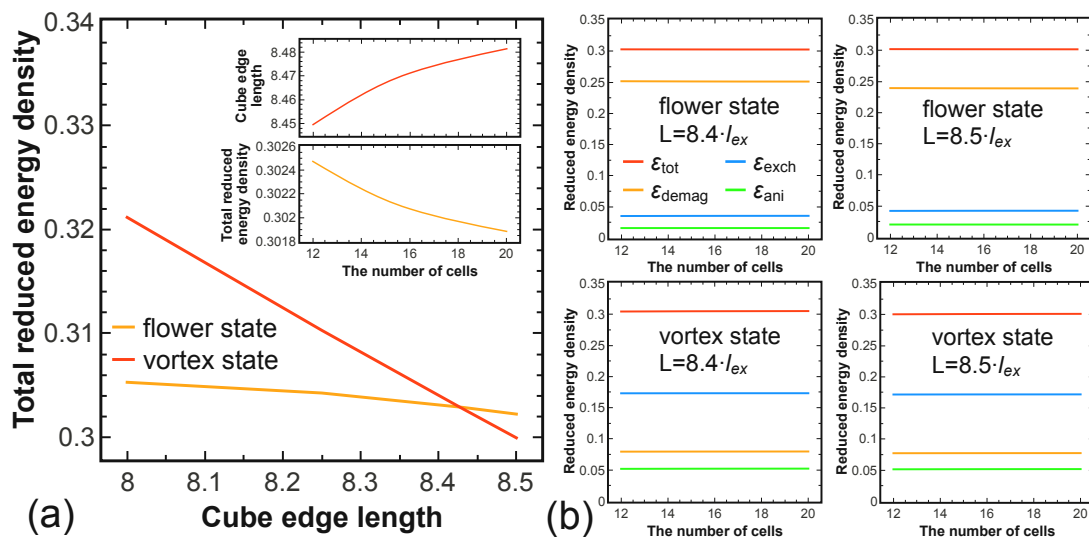


Figure 6.8: (a) The total energy density for two magnetization state of the cube vs. the length of the cube edge for a discretization mesh of $10 \times 10 \times 10$. The inset at the top shows the cube edge length with equality of the total energy density in two magnetization state of the cube for different discretization mesh from $12 \times 12 \times 12$ to $20 \times 20 \times 20$. The value of this total energy density is shown in the inset at the bottom. (b) Different contributions to the total energy density for two magnetization states of the cube for $L = 8.4l_{ex}$ and $L = 8.5l_{ex}$.

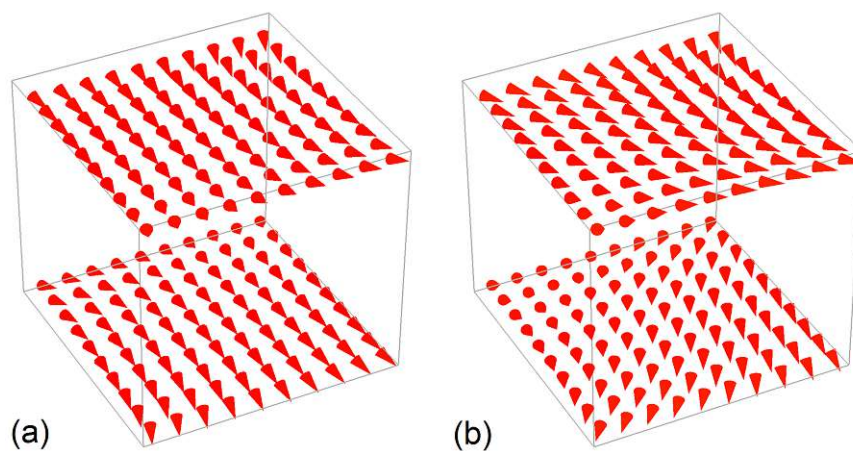


Figure 6.9: Different type of the cube “flower state”: (a) normal ($L = 8l_{ex}$) and (b) twisted flower ($L = 8.5l_{ex}$). Only the top and bottom magnetization layer of the cube are shown.

Figure 6.8a shows the simulation results for the length of cube edge from $8l_{ex}$ to $8.5l_{ex}$, for a discretization mesh of $10 \times 10 \times 10$. Equality of the total energy density was found for the length of cube edge equal to $8.43l_{ex}$. The small bending of the curve for the

total energy density for the “flower state” is determined by a transition to another kind of the “flower” with increasing the cube edge, the so called “twisted flower state”, which becomes energetically more favorable (Figure 6.9). For other discretization meshes the result is shown in inset of Figure 6.8a. Energy equality was found at about the same values of the total energy density.

Another useful check is to proof the independence of the total energy density from the discretization mesh. Figure 6.8b shows simulation results for total, demagnetization, anisotropy, and exchange energy densities for two magnetization cube states, for the edge length $8.4l_{ex}$ and $8.5l_{ex}$. As expected, the energy density is independent on the discretization mesh from $12 \times 12 \times 12$ to $20 \times 20 \times 20$.

7 STT-MRAM Cells Structure Optimization

7.1 Influence of the Reference Layers

First, the influence of the reference layers on switching time of the penta-layer nanopillar structure (Figure 7.1) is investigated. The model geometry of the nanopillar is defined as $\text{CoFe}(8\text{nm})/\text{AlO}_x(0.7\text{nm})/\text{Py}(4\text{nm})/\text{Cu}(6\text{nm})/\text{CoFe}(5\text{nm})$ (Py is $\text{Ni}_{81}\text{Fe}_{19}$), with an elliptical cross-section with 90- and 35-nm axes [66]. In the structure the different spacer layers are used to keep the difference in the magnetoresistance between the two states. This leads to an asymmetric switching time due to the different torques associated with the different spacer layers and therefore the structures require optimization.

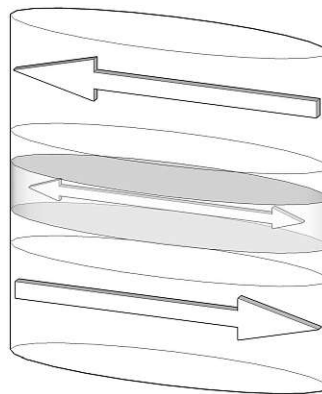


Figure 7.1: Schematic illustration of penta-layer MTJs.

The employed parameters for the simulations are shown in Table 7.1. Figure 7.2a demonstrates an evolution of the average magnetization in the free magnetic layer during switching. A compensating external magnetic field is introduced. The results are in good agreement with those for the same elliptical cross-section at 77K reported in [64]. The difference between the switching times from parallel to anti-parallel (with respect to the oxide tunnel junction) configuration increases when the compensating magnetic field is turned off (Figure 7.2b). The compensation can also be achieved by modifying the thicknesses of the fixed ferromagnetic layers and/or the distances between the layers. This opens the way for an optimization of the penta-layers structure.

Symbol	$T=77\text{K}$	$T=300\text{K}$
η_1	0.3	0.3
η_2	0.35	0.35
γ	$2.3245 \cdot 10^5 \text{ m}/(\text{A}\cdot\text{s})$	$2.3245 \cdot 10^5 \text{ m}/(\text{A}\cdot\text{s})$
α	0.01	0.01
A	$1.3 \cdot 10^{-11} \text{ J}/\text{m}$	$1.1 \cdot 10^{-11} \text{ J}/\text{m}$
M_S	$644 \cdot 10^3 \text{ A}/\text{m}$	$560 \cdot 10^3 \text{ A}/\text{m}$
M_{Sp}	$1.15 \cdot 10^6 \text{ A}/\text{m}$	$1 \cdot 10^6 \text{ A}/\text{m}$

η_1 – for MTJ with dielectrical spacer

η_2 – for GMR with metal spacer

$M_{Sp1} = M_{Sp2} = M_{Sp}$

Table 7.1: CoFe/AlO_x/Py/Cu/CoFe structure simulation parameters.

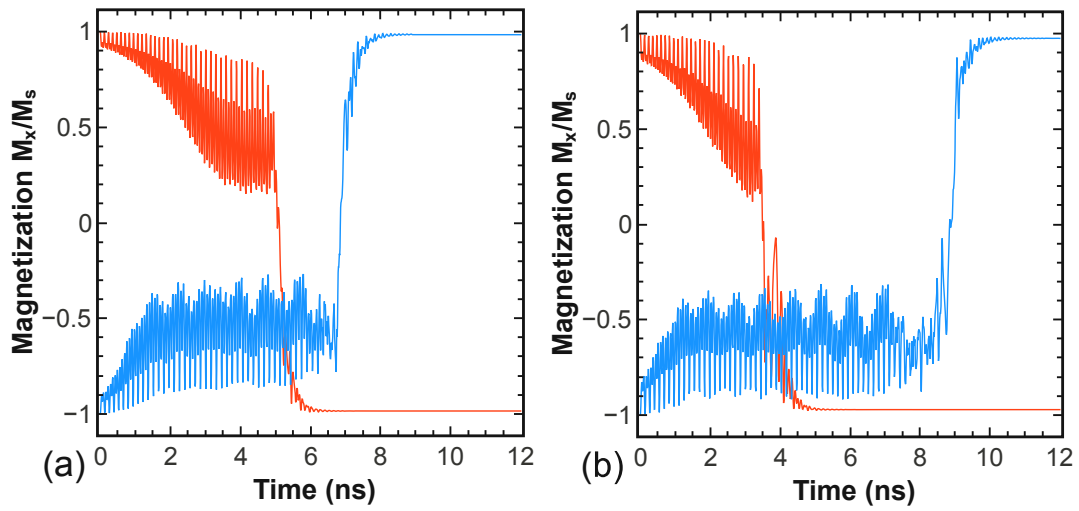


Figure 7.2: Evolution of the averaged magnetization of the free ferromagnetic layer during switching in a penta-layer structure: (a) compensating magnetic field 26mT; (b) no compensating field.

In the following, the influence of the thicknesses of the fixed layers on the in-plane magnetostatic field in the free magnetic layer is investigated. The corresponding dependence is shown in Figure 7.3. Each point is the result of statistical averaging with respect to 15 different realizations of the switching process. It demonstrates that the switching time from parallel to anti-parallel configuration and vice versa depends strongly on the fixed layer thickness. The most symmetric switching is achieved when the second fixed layer thickness is around 9-10 nm.

It is interesting to note that the switching time is shorter, when the compensation is achieved by modifying the thicknesses of the fixed ferromagnetic layers than in the case of an applied external field. To find the reason for this discrepancy, one should have

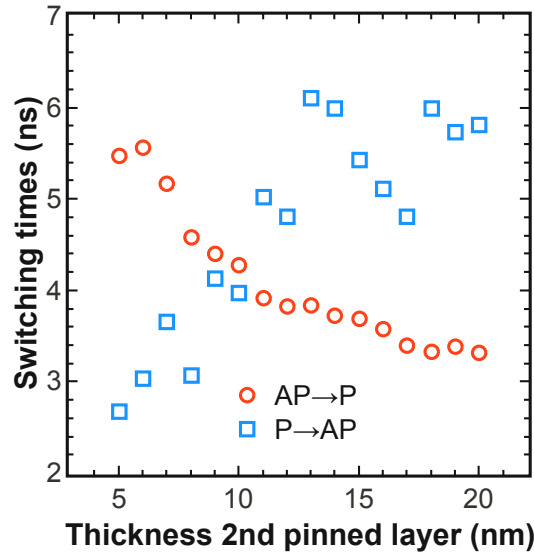


Figure 7.3: Dependence of the switching times between the two stable configurations on the thickness of the second fixed magnetic layer. The thickness of the first fixed magnetic layer is 8 nm.

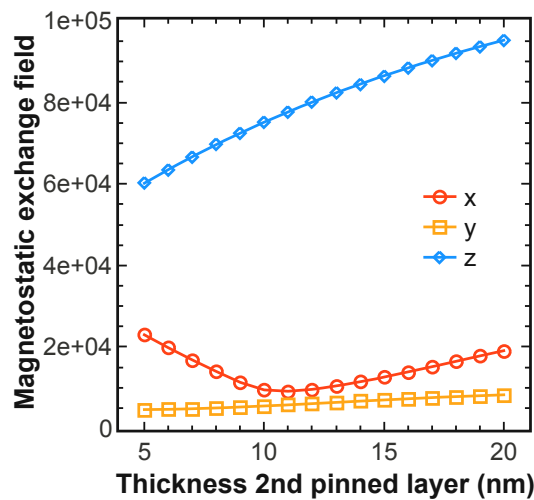


Figure 7.4: Dependence of the absolute values of different components of the averaged magnetostatic field \mathbf{H}_{ms} acting on the free magnetic layer on the thickness of the second fixed magnetic layer. The thickness of the first magnetic layer is fixed at 8 nm. The x - and y -component is directed along the long and short axis of the ellipsis, respectively, the z -component is directed parallel to the out-of-plane direction.

in mind that by varying the thickness of the fixed layer, one can only compensate the in-plane component of the magnetostatic field. At the same time, the field projection perpendicular to the plane is not compensated. The absolute value of the average field

orthogonal to the plane of the free layer is shown in Figure 7.4. This field component facilitates switching and explains the reduction in switching time.

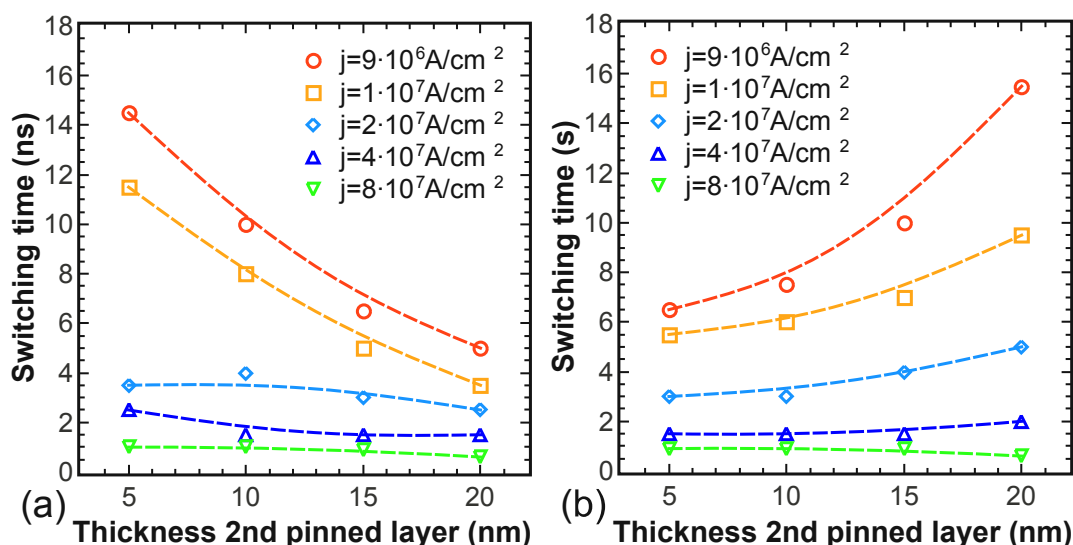


Figure 7.5: Dependence of the switching time for different current densities as function of the thickness of the fixed layer. The thickness of the free layer is 4.5 nm, $T=300\text{K}$, and the ellipse axes are 120 and 40 nm. (a) Switching from anti-parallel to parallel configuration. (b) Switching from parallel to anti-parallel configuration.

In order to make the system thermally stable at room temperature, the thickness of the free layer is increased from 4nm to 4.5nm, and the elliptical cross-section axes to 120 and 40 nm, correspondingly. Figure 7.5 displays the dependences of the switching times as a function of the fixed layer thickness at different current densities. As the current increases, the switching time decreases, as expected. Interestingly, the dependence of the switching time on the thickness vanishes at large current densities. This signifies that the magnetostatic coupling between the fixed and the free layers becomes irrelevant at high current densities. It is to note again that, at low current densities, an optimization of a particular penta-layer structure is required to achieve fast and symmetric switching behavior.

7.2 Composite Free Layer

For a future optimization of the nanopillar the structure with a composite free layer is proposed. The structure with a composite ferromagnetic free layer is obtained by removing a central stripe of width s from the monolithic free layer (Figure 7.6). In a first step the structure CoFe/spacer oxide(1nm)/Py(4nm)/spacer oxide(1nm)/CoFe (Py is $\text{Ni}_{81}\text{Fe}_{19}$) with an elliptical cross-section (major axes 90nm and 35nm, and $s=5\text{nm}$, correspondingly) is investigated. In order to simplify the identification of the important

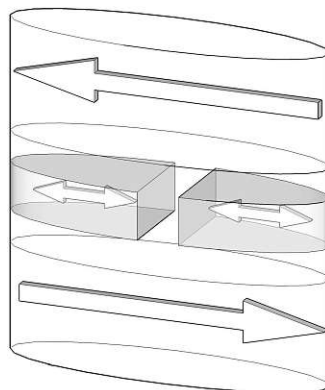


Figure 7.6: Schematic illustration of penta-layer MTJs with composite free layer.

features related to switching for such structures, it is assumed to be symmetric (the spacer layers are equivalent). It should be noted that for an asymmetric structure it is possible to apply the method described above to achieve a symmetric switching time.

Contrary to the standard consideration, it is not assumed the reference layers being fully compensated. They produce the magnetostatic field \mathbf{H}_{ms} , which couples the pinned layers and the free layer, thus offering an additional degree of freedom to improve the characteristics of the system.

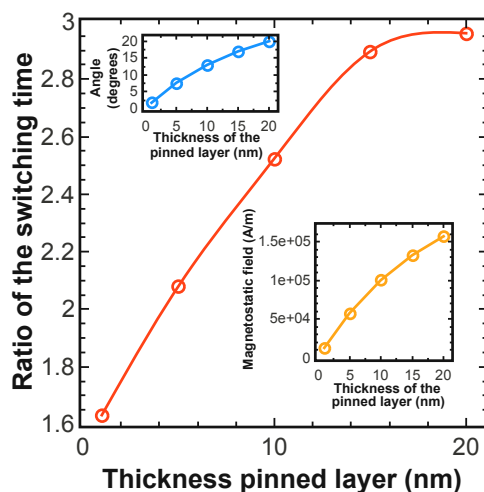


Figure 7.7: Ratio of the switching time in the monolithic structure vs. the switching time in the composite structure as function of the thickness of the pinned layer. The insets show the averaged initial angle (top) and the dependence of the absolute values of the z -component of the averaged magnetostatic field (bottom).

This non-compensated field causes the magnetization of the free layer to tilt out of the $x - y$ plane. The non-zero angle between the fixed magnetization and the magnetization in the free layer results in an enhanced spin transfer torque, when the current

starts flowing perpendicular to the $x - y$ plane. In the case of the monolithic structure, however, the torque remains marginal in the central region, where the magnetization is along the x axis. As the amplitude of the end domains precession increases, the central region experiences almost no spin torque and preserves its initial orientation along the x axis, thus preventing the whole layer from alternating its magnetization orientation. This is, however, not the case when the central region is removed in the composite structure and the end domains become virtually independent. Figure 7.7 demonstrates a substantial decrease of the switching time in the penta-layer structure with the composite free layer, for the same current density, as a function of the thickness of the pinned ferromagnetic layers. The switching process for the pinned layer thicknesses of 5nm, 15nm, and 20nm is shown in Figure 7.8. Due to the removal of the central region, which represented the “bottleneck” for switching in the monolithic structure, the shape anisotropy energy decreases (Figure 7.8, inset). However, its value is still sufficiently large for guaranteeing the thermal stability at operation conditions [66].

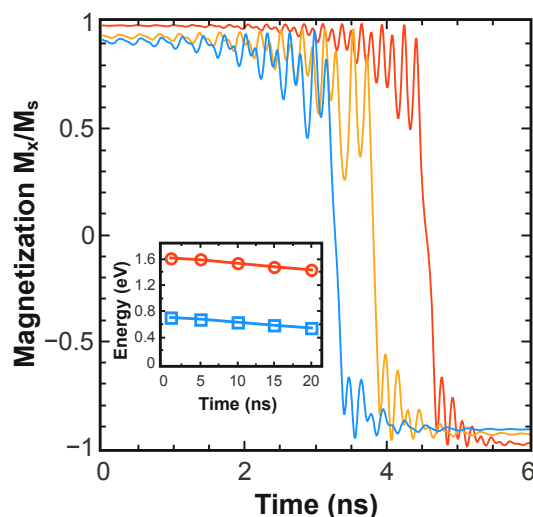


Figure 7.8: Switching process for MTJs with composite-free layer for the pinned layer thicknesses of 5 nm, 15 nm, and 20 nm (from right to left). The inset shows the shape anisotropy energy as the function of the thickness of the pinned layer for monolithic (circles) and composite (squares) free layer.

The switching time in a penta-layer structure with a composite free layer is decreasing, if the thickness of the pinned layers is increased. This is due to the fact that the z -component of the magnetostatic field \mathbf{H}_{ms} (Figure 7.7, bottom inset) increases together with the pinned layer thickness, causing a larger initial angle (Figure 7.7, top inset) between the relaxed magnetization in the domains of the free layer and the magnetization of the pinned layer, a larger torque and, as a consequence, a shorter switching time.

In the section only a first description and raw explanation of the fast switching phe-

nomena in the structure with the composite free layer was given. In the following the structure and phenomenon is discussed in detail.

7.2.1 Switching time reduction

For a more detailed study of the structure with composite free layer, CoFeB was considered as material for the free and reference layers (Table 7.2).

Symbol	$T=300\text{K}$
η	0.63
γ	$2.3245 \cdot 10^5 \text{ m}/(\text{A}\cdot\text{s})$
α	0.005
A	$1 \cdot 10^{-11} \text{ J}/\text{m}$
K_1	$2 \cdot 10^3 \text{ J}/\text{m}^3$
M_S	$8.9 \cdot 10^5 \text{ A}/\text{m}$

$$M_{Sp1} = M_{Sp2} = M_{Sp} = M_S$$

Table 7.2: CoFeB/MgO/CoFeB/MgO/CoFeB structure simulation parameters.

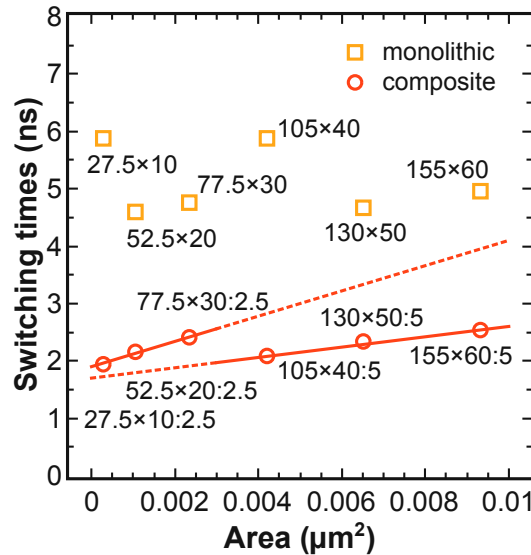


Figure 7.9: Average value of the switching times for MTJs with monolithic ($length \times width$) and composite ($length \times width : separation$) free layer as function of the cross-section area. Each point is a result of statistical averaging with respect to 50 realizations of the switching process.

The dependence of the switching time on the aspect ratio of the free layer is investigated now. The aspect ratio is chosen so that for a composite free layer $((length - separation)/2)/width = 1.25$. Figure 7.9 shows a decrease of the switching time in MTJs with a composite free layer as compared to that in MTJs with a monolithic

free layer of similar dimensions, for all cross-section areas. Each point is a result of statistical averaging with respect to 50 different realizations of the switching process. The results clearly show a linear dependence of the switching time in the composite structures on the ratio $area/separation$.

7.2.2 Thermal stability factor calculation

As discussed in Chapter 4 the critical parameter for the STT-MRAM is thermal stability, so the detailed investigation of the composite structure has to begin with the determination of this parameter. To find the switching path due to thermal agitations it is necessary to determine the state for which the barrier separating the two stable magnetization states in the free layer is minimal. Figure 7.10 shows that the switching path due to thermal agitations must go through the state with magnetizations of the halves opposite to each other (the C state in Figure 7.10).

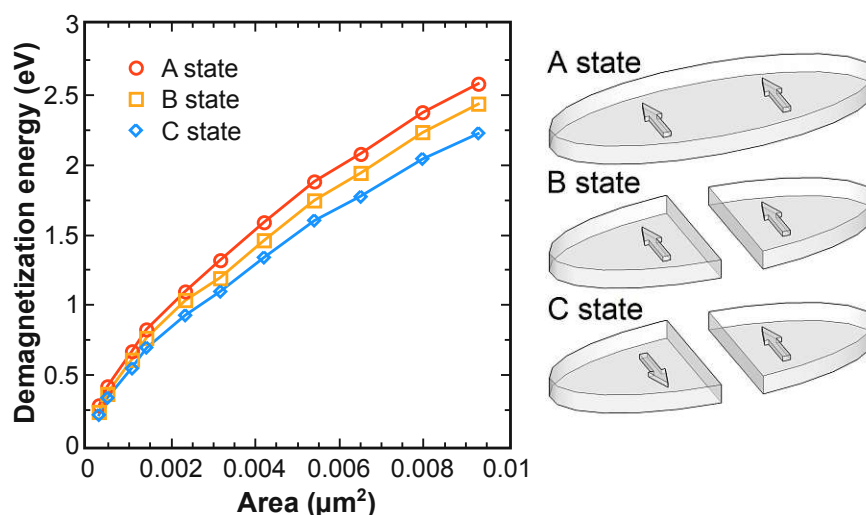


Figure 7.10: Dependence of the demagnetization energy for MTJs with monolithic (A) and composite (B,C) free layers as a function of the cross-sectional area.

Thus, the thermal stability factor for a composite structure is determined by the energy difference between the system in the state C (Figure 7.10) and the system with magnetization directed along the long axis of the ellipse.

After determining the method of calculating the thermal stability factor for the composite structure, the influence of scaling the dimensions on the thermal stability factor for MTJs with a composite free layer must be investigated. Due to the removal of the central region from the monolithic structure, the shape anisotropy is slightly decreased together with the thermal stability factor. To boost the thermal stability factor, it is sufficient to increase the thickness of the free layer and/or the aspect ratio. Figure 7.11 shows the thermal stability factors of MTJs with a composite free layer as a function

of the free layer thickness d . An MTJ with $52.5 \times 10\text{nm}^2$ cross-section and $d = 5\text{nm}$ free layer thickness has a thermal stability factor $\sim 60k_B T$, which exceeds all of the single p-MTJs demonstrated to date [199].

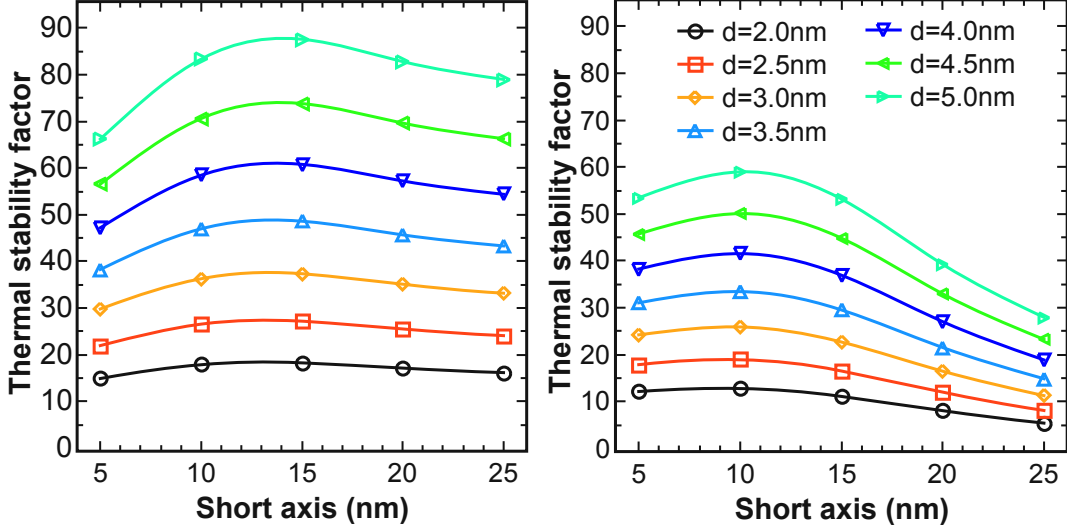


Figure 7.11: Thermal stability barrier for MTJs with monolithic (left) and composite free layer (right) as a function of the short axis length for several free layer thicknesses d . The long axis is fixed at 52.5nm and the thickness of the fixed layer is 5nm .

The similarity of change of the thermal stability factor for the monolithic and composite free layer allows us to derive an analytical equation for the calculation of the thermal stability factor of the composite structure based on the analytical equation for the monolithic free layer. For monolithic free layer with elliptical cross-section ($l > w \gg d$) the approximate value of the thermal stability factor is determined as [60]:

$$\Delta_m \approx d \left(\frac{1}{w} - \frac{1}{l} \right) \cdot \frac{\mu_0 M_S^2}{k_B T} \cdot V_m. \quad (7.1)$$

Here, w and l are the dimensions of the ellipse along the short and long axis, respectively, and V_m is the volume of the monolithic free layer. Similar to Equation 7.1, the approximate value of the thermal stability factor for composite free layer is described as:

$$\Delta_c \approx d \left(\frac{a}{w} - \frac{1}{l} \right) \cdot \frac{\mu_0 M_S^2}{k_B T} \cdot V_c. \quad (7.2)$$

Here, a is a fitting parameter, $V_c = V_m - w \cdot s \cdot d$ is the volume of the composite free layer, where s is a distance between two parts of the composite free layer.

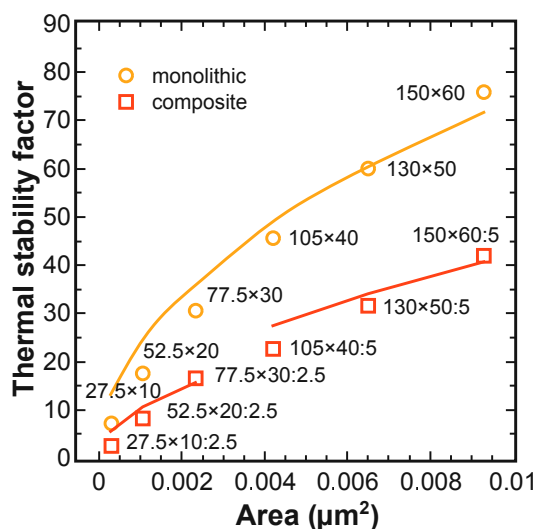


Figure 7.12: Thermal stability barrier for MTJs with monolithic and composite free layer as a function of the cross-section area. The approximate value of the thermal stability factors are obtained by Equations 7.1–7.2 (shown by lines). Symbols indicate the results obtained from micromagnetic simulation.

Figure 7.12 shows the result of the thermal stability factor simulations based on two different approaches. The fitting parameter a for the composite structure strongly depends on the separation and is equal to $2/3$ for small separations ($s = 2.5\text{nm}$), and $3/4$ for larger separations ($s = 5\text{nm}$).

7.2.3 Switching energy reduction

To reveal the reason for fast switching one has to look at the magnetization dynamics of the left and right part of the composite structure separately (Figure 7.13). A structure with an elliptical $52.5 \times 25\text{nm}^2$ cross-section and the following layer sequence is considered: CoFeB(5nm)/MgO(1nm)/CoFeB(2nm)/MgO(1nm)/CoFeB(5nm). The central 2.5 nm stripe is removed from the middle CoFeB layer. Figures 7.13b and 7.13c show that the switching processes of the left and right parts of the composite free layer occur in opposite senses to each other. Most importantly, the magnetizations of each piece stay practically in-plane. Because the magnetization does not go out-of-plane, as during switching of the monolithic free layer, this switching behavior should lead to a decrease of the switching energy barrier. It turns out that the switching paths by current and due to thermal fluctuations are similar. Thus, as in p-MTJs, the switching barrier in the composite structure becomes practically equal to the thermal stability barrier defined by the shape anisotropy of the composite free layer structure. The reduction of the switching barrier leads to the reduction of the switching time in a composite structure as compared to a conventional MTJ at the same switching current density.

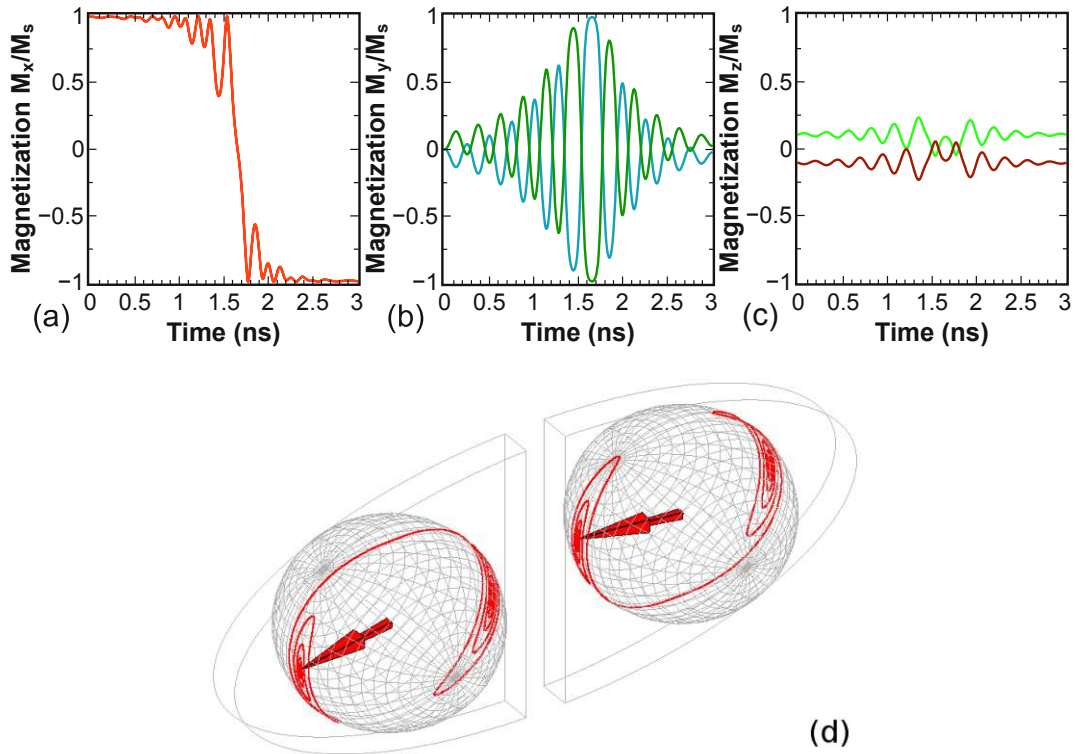


Figure 7.13: Magnetization components vs. time for an elliptical $52.5 \times 25\text{nm}^2$ MTJ with a composite free layer. The magnetization of the left and right halves is shown separately.

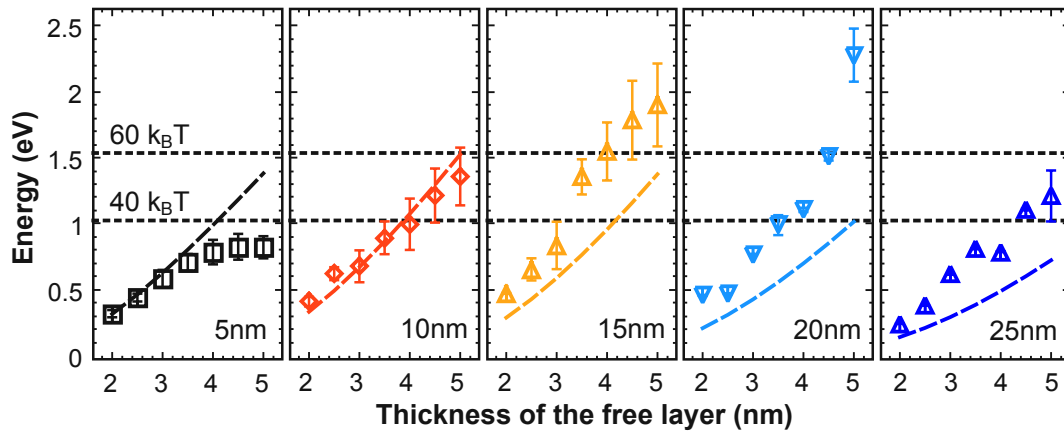


Figure 7.14: Thermal energy (lines) vs. switching energy (symbols) barriers for the composite structure. The long axis is fixed at 52.5nm and the thickness of the fixed layer is 5nm . Dependences are shown for short axes of 5nm , 10nm , 15nm , 20nm , and 25nm length. Each point is a result of statistical averaging with respect to 30 different realizations of the switching process.

In the following the height of the thermal energy barrier is compared with that of the switching energy barrier (Figure 7.14). As expected from the analysis of the magnetization dynamics, the switching barrier becomes practically equal to the thermal stability barrier.

Figure 7.15 shows the ratio of the switching energy barrier in monolithic and composite structures. It displays an almost 14-fold decrease of the switching energy in MTJs with composite layer.

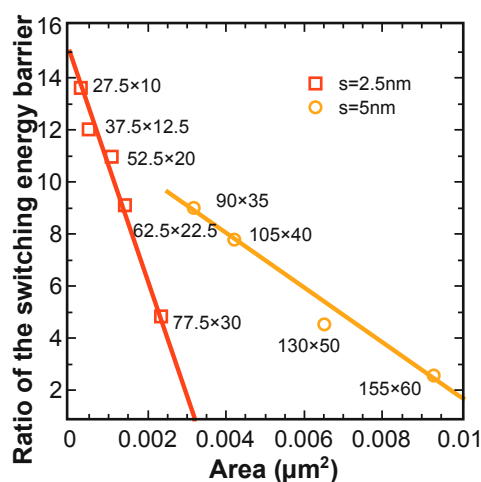


Figure 7.15: Ratio of the switching energy barriers in the monolithic to the composite structure as function of the cross-section area. Each point is a result of statistical averaging with respect to 50 realizations of the switching process.

7.2.4 Acceleration switching effect

The equality of the switching and the thermal barriers in composite structures results in an almost linear increase of the switching time in these MTJs with increasing thickness of the free layer and/or aspect ratio, see Figure 7.16a. The dependence for the monolithic structure is shown in Figure 7.16b.

The influence of the MTJ geometry on the switching acceleration in MTJs with a composite free layer relative to the one with a monolithic layer is illustrated in Figure 7.17. The long axis is fixed at 52.5nm. Each point is a result of statistical averaging over 30 different realizations of the switching process. To decrease the switching time in the composite structure it is necessary to increase the thickness of the pinned layers. An almost threefold reduction of the switching time is achieved in MTJs with a composite free layer without compromising the thermal stability.

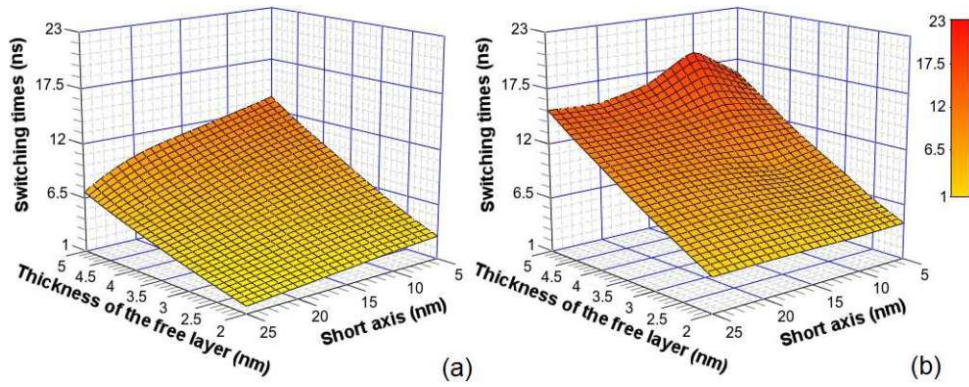


Figure 7.16: Switching times in the composite structure (a) and a monolithic structure (b) as a function of the thickness of the free layer and short axis length. The long axis is fixed at 52.5nm and the thicknesses of the fixed layers are 5nm.

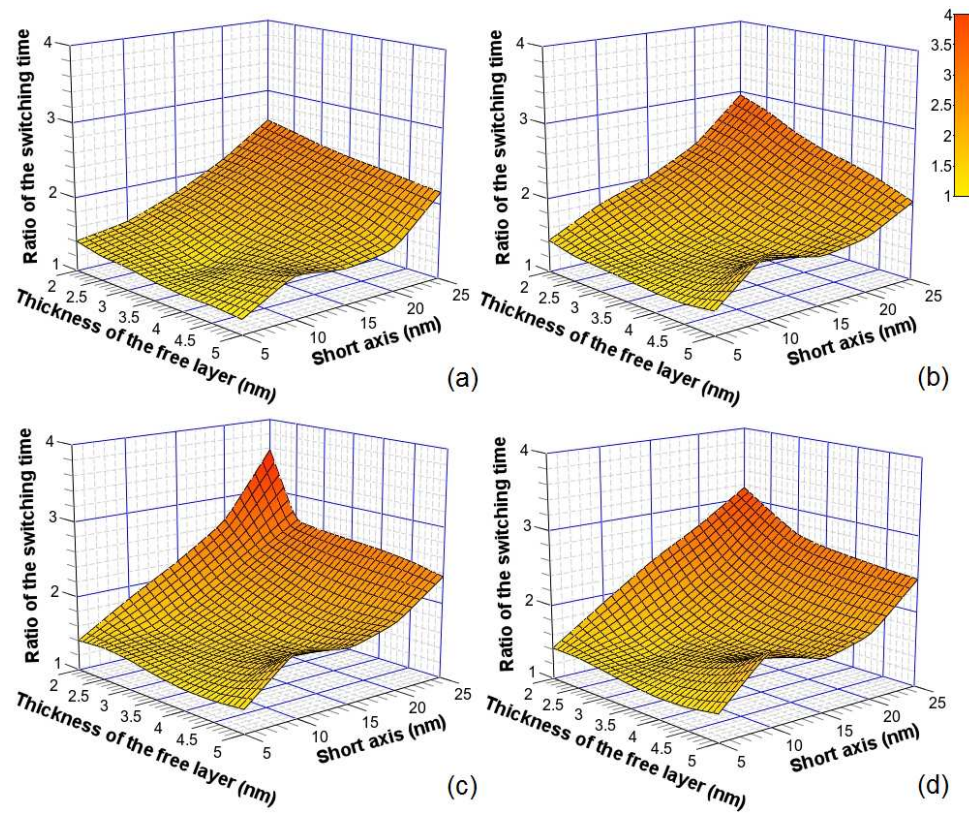


Figure 7.17: Switching time ratio between the monolithic and composite structures vs. free layer thickness and short axis length. The long axis is fixed at 52.5nm. Dependences are shown for the thickness of the fixed layers: (a) 5nm, (b) 10nm, (c) 15nm, and (d) 20nm.

7.2.5 Standard deviation of the switching time distribution

Now the standard deviations of the switching time distributions are compared in the monolithic and composite structure shown in Figure 7.18a. The width of the switching time distribution for MTJs with a composite free layer can be almost ~ 2000 times narrower than that for MTJs with a monolithic free layer. The dependence of the value of the standard deviation on composite layer thickness and aspect ratio is also shown in Figure 7.18b. An MTJ with $52.5 \times 25\text{nm}^2$ cross-section has a standard deviation of the switching time $\sim 10^{-3}\text{ns}$, while an MTJ with $52.5 \times 10\text{nm}^2$ cross-section has the standard deviation of the switching time 0.3-1.6ns.

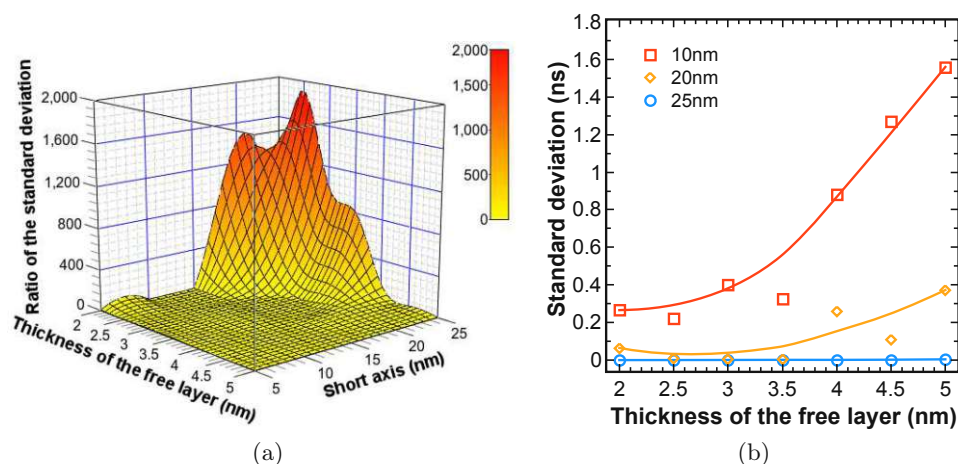


Figure 7.18: (a) Ratio of the standard deviation of the switching time in the monolithic structure and composite structure as function of thickness of the free layer and short axis length. The long axis is fixed at 52.5nm and the thickness of the fixed layers are 10nm. (b) The standard deviation of the switching time distribution in the composite structure as a function of thickness of the free layer. The long axis is fixed at 52.5nm and the thickness of the fixed layers are 15nm. Dependences are shown for short axis of 10nm, 20nm, and 25nm.

In order to find a physical explanation for the distribution narrowing, the switching process is analyzed in detail. A schematic illustration of the self-stabilization and self-acceleration principle of switching in a composite free layer is explained in Figure 7.19. Each half of the free layer generates a stray magnetic field which influences the other half and helps stabilizing the switching process. This stray magnetic field increases with growing short axis which leads to the switching times distribution narrowing. Before the moment when the magnetizations of the different halves of the composite layer are in opposite directions to each other (Figure 7.19b) the stray magnetic field acts as a stabilizing factor of switching (Figure 7.19a). After the opposite magnetization state the stray magnetic fields accelerate switching as illustrated in Figure 7.19c.

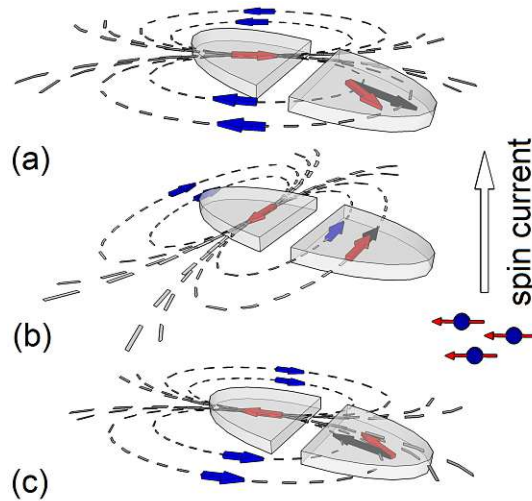


Figure 7.19: Schematic illustration of (a) the state with self-stabilization direction of the stray magnetic field, (b) opposite magnetization state, and (c) self-acceleration switching state in an MTJ with a composite free layer.

7.3 Structure Optimization of the Composite Free Layer

In this section a structural optimization of the composite free layer (see subsection 7.2) is presented by means of extensive micromagnetic simulations and a new structure for the composite free layer is proposed. To distinguish the two types of composite free layers, the notation for an MTJ with the free layer consisting of two equivalent parts of half-elliptic form separated by a narrow non-magnetic spacer is introduced as C-MTJ (Figure 7.6) and C2-MTJ for the new structure.

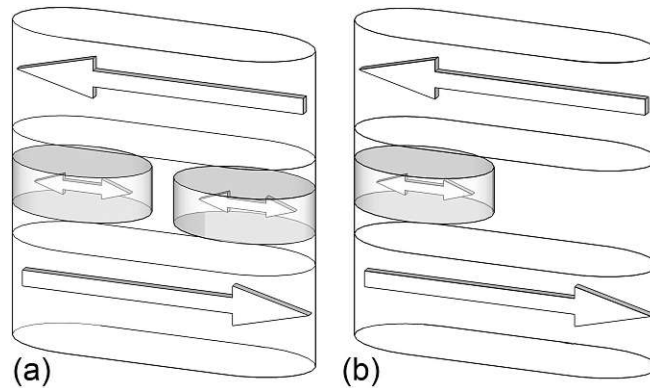


Figure 7.20: Schematic illustration of penta-layer MTJs: (a) with composite free layer (C2-MTJ) and (b) with monolithic free layer (M2-MTJ).

The free layer of the C2-MTJ (Figure 7.20a) is composed of two ellipses with the axes $a/2$ and b inscribed into a rectangle $a \times b$. Thus, the newly proposed structure does not

require a narrow gap between the two parts of the composite layer, and therefore can be easily fabricated. Next, the most important parameters of STT-MRAM devices, switching time, thermal stability, and switching energy barrier of C2-MTJ, C-MTJ, conventional MTJ with monolithic free layer (Figure 7.1), and an M2-MTJ structure with one small free layer elliptical shape (Figure 7.20b) are compared.

7.3.1 Switching time and standard deviation

First, the switching times of C2-MTJs are discussed and compared with those of C-MTJs. Figure 7.21 shows the dependence of the switching time on the thicknesses of the free layer for three values of the short axis: 10nm, 15nm, and 20nm. The long axis is fixed at 52.5nm. The simulations demonstrate that C2-MTJs and C-MTJs have practically equal switching times for all considered cross-sections of the free layer.

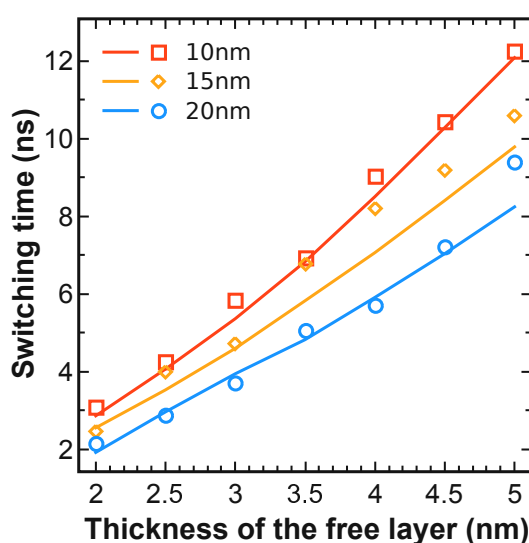


Figure 7.21: Switching time of C-MTJs (symbols) and C2-MTJs (lines) as function of the thickness of the free layer. The long axis is fixed at 52.5nm and the thickness of the fixed layer is 5nm. Dependences are shown for short axes of 10nm, 15nm, and 20nm length. Each point is a result of statistical averaging with respect to 30 different realizations of the switching process.

The fact that the switching times in C-MTJs and C2-MTJs are equal also means a switching acceleration for C2-MTJs as compared to the conventional MTJ with a monolithic free layer. This is indeed confirmed by the results of the simulations shown in Figure 7.22a. Figure 7.22b demonstrates that C2-MTJs display almost the same switching times as the structure with a single small ellipse (M2-MTJ, Figure 7.20b).

Now the standard deviations of the switching time distributions in C-MTJs and C2-MTJs are compared. The dependence of the value of the standard deviation on composite layer thickness and aspect ratio for C2-MTJ is shown in Figure 7.23. With

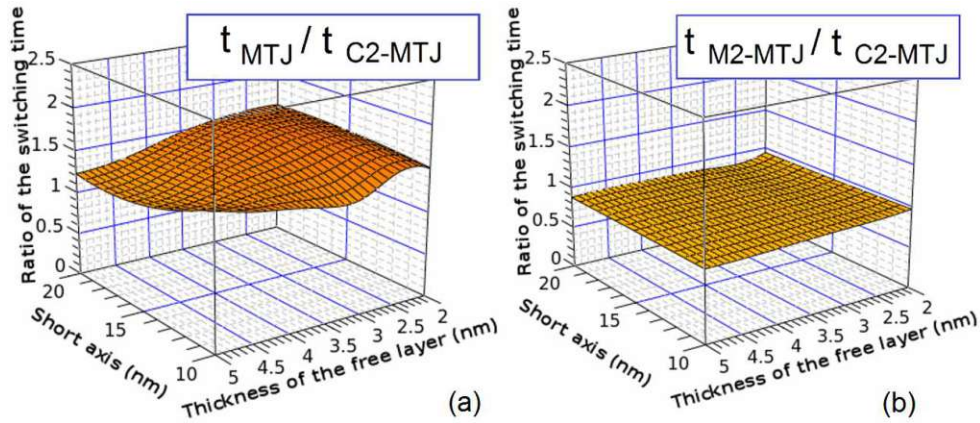


Figure 7.22: Ratio of the switching times in the monolithic structure and composite structure as function of thickness of the free layer and short axis length. The long axis is fixed at 52.5nm. Dependences are shown for ratio: (a) conventional MTJ vs. C2-MTJ, (b) M2-MTJ vs. C2-MTJ.

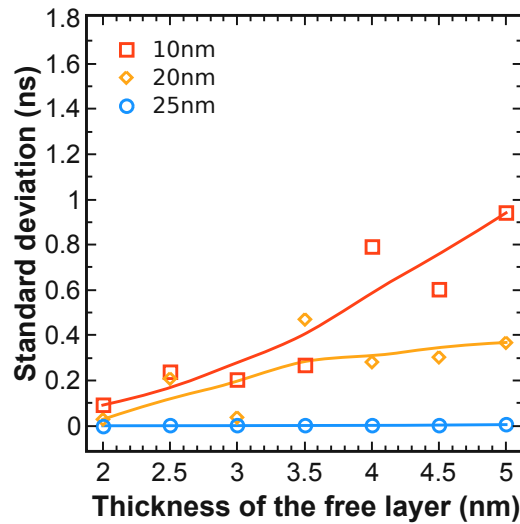


Figure 7.23: The standard deviation of the switching time distribution in the C2-MTJ structure as function of the thickness of the free layer. The long axis is fixed at 52.5nm and the thickness of the fixed layer is 15nm. Dependences are shown for the short axis of 10nm, 20nm, and 25nm. Each point is a result of statistical averaging with respect to 30 different realizations of the switching process.

$52.5 \times 25\text{nm}^2$ cross-section a standard deviation of the switching time $\sim 10^{-3}\text{ns}$ is obtained for both structure, while with $52.5 \times 10\text{nm}^2$ cross-section the standard deviation of the switching time is 0.3-1.6ns for the C-MTJ (Figure 7.18b) and 0.09-0.9ns for the C2-MTJ (Figure 7.23). Thus the C2-MTJ structure shows a ~ 2 -3 times narrower distribution of the switching times as compared to the C-MTJ structure at large aspect ratio of the free layer.

7.3.2 Thermal stability factor

Now the thermal stability factor for the two types of the composite layer structures, C-MTJ and C2-MTJ, are compared. Figure 7.24a confirms that the replacement of the free layer consisting of the two half-ellipses separated with a narrow gap (C-MTJ) by only two small ellipses (C2-MTJ), does not result in a loss of thermal stability. With $52.5 \times 10 \text{nm}^2$ cross-section and 5nm thickness of the free layer a thermal stability factor $\sim 60k_B T$ is obtained.

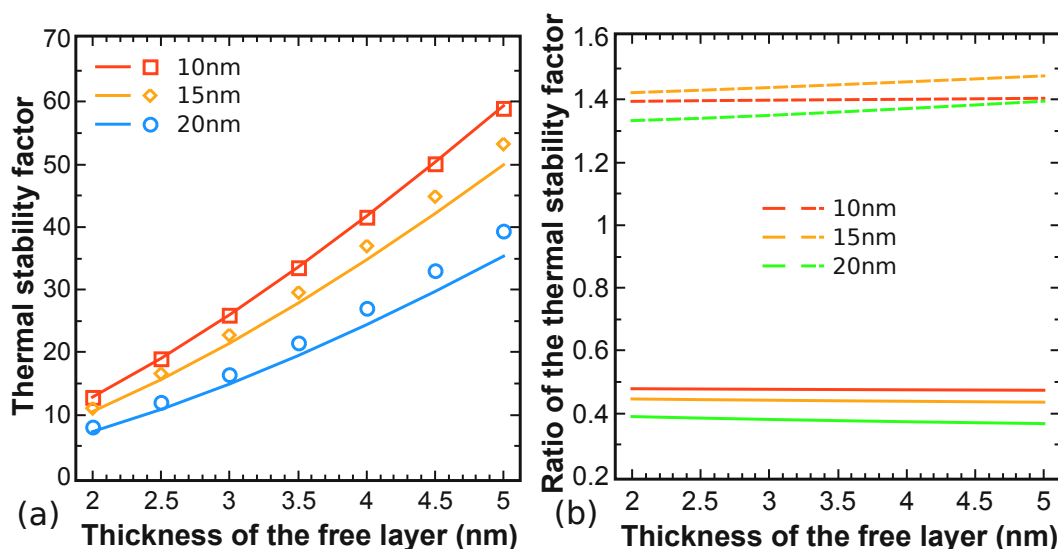


Figure 7.24: (a) Thermal stability factor for C-MTJ (symbols) and C2-MTJ (lines) as function of the thickness of the free layer. Each point is a result of statistical averaging with respect to 30 different realizations of the switching process. (b) Ratio of the thermal stability factors for monolithic structure and composite structure as function of thickness of the free layer and short axis length. Dependences are shown for ratio: M2-MTJ to C2-MTJ (solid lines), conventional MTJ to C2-MTJ (dotted lines). The long axis is fixed at 52.5nm and the thickness of the fixed layer is 5nm. Dependences are shown for short axes of 10nm, 15nm, and 20nm length.

Next, the thermal stability factor for C2-MTJ with that of the two structures with monolithic free layer, conventional MTJ and M2-MTJ, are compared. Due to the removal of the central region from the monolithic structure the shape anisotropy in the C2-MTJ is decreased together with the thermal stability factor (Figure 7.24b). The constant ratio of the thermal stability factor as a function of the aspect ratio and thicknesses of the free layer indicates that the thermal stability factors for both structures scales similarly. This means that in order to increase the thermal stability factor in C2-MTJs it is sufficient to increase the thickness of the free layer and/or the aspect ratio.

In comparison to the second structure with monolithic free layer, M2-MTJ, the C2-MTJ structure shows a gain in thermal stability by a factor of ~ 2 times (Figure 7.24b), while maintaining the same switching time (Figure 7.22b), confirming the superiority of the C2-MTJ structure over the M2-MTJ one.

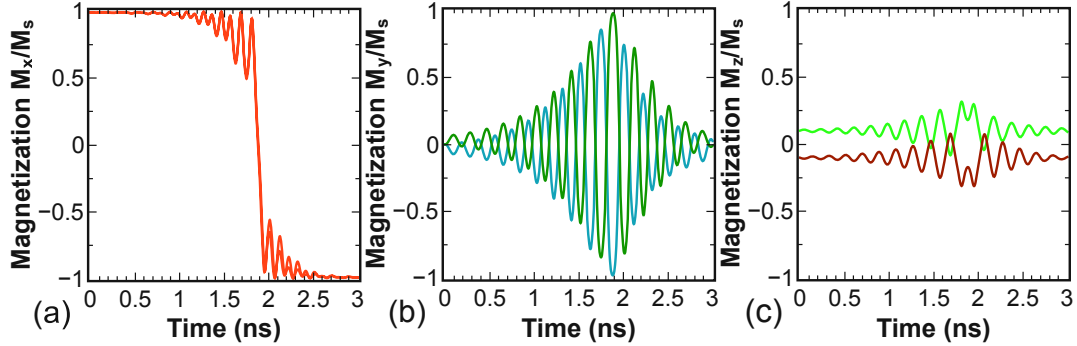


Figure 7.25: Magnetization components vs. time for an elliptical $52.5 \times 20\text{nm}^2$ C2-MTJ. The magnetization of the left and right halves is shown separately.

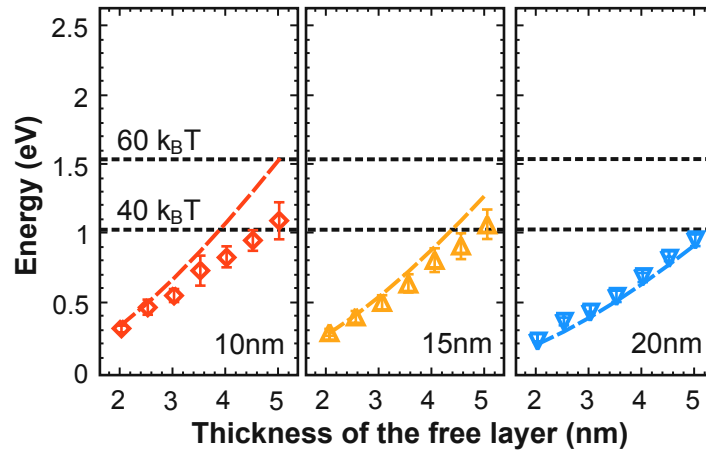


Figure 7.26: Thermal energy (lines) vs. switching energy (symbols) barriers for the C2-MTJ structure. The long axis is fixed at 52.5nm and the thickness of the fixed layer is 5nm . Dependences are shown for short axes of 10nm , 15nm , and 20nm length. Each point is a result of statistical averaging with respect to 30 different realizations of the switching process.

7.3.3 Switching energy

To determine the reason of the fast switching in C2-MTJs the switching process was investigated in detail. Figure 7.25 shows that, as in a C-MTJ, the switching processes of the left and right part of the C2-MTJ free layer occur in opposite senses to each other. Importantly, the switching occurs in the $x - y$ plane. This is clearly seen at the

time instance for 1.9ns, when the left and right ellipses pass simultaneously through the state $(0; -1; 0)$ and $(0; 1; 0)$ respectively (Figure 7.25).

In the following the height of the thermal energy barrier is compared with that of the switching energy barrier. As expected from the analysis of the magnetization dynamics, the switching barrier becomes practically equal to the thermal stability barrier in both C-MTJ (Figure 7.14) and C2-MTJ (Figure 7.26) structures. The C2-MTJ structure possesses a slightly lower switching barrier as compared to the C-MTJ structure with the same aspect ratio of the free layer.

8 Magnetization Oscillations in MTJ-based Structures

8.1 Switching Failure in a MTJ-based STT-MRAM

During the comparison between the switching time of the structure with composite and monolithic free layers, it has been found that for a structure with the geometry CoFeB(5nm)/MgO(1nm)/CoFeB(3.5nm)/MgO(1nm)/CoFeB(5nm) and a monolithic free layer with an elliptical cross-section $52.5 \times 15 \text{ nm}^2$, a large percentage of switching was finished with failure (i.e. did not result to opposite magnetization state). In this section the switching probability of in-plane penta-layer MTJs for different switching current densities and pulse durations is investigated.

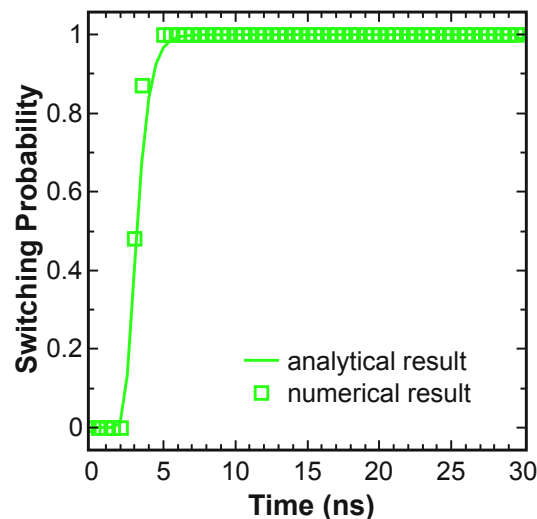


Figure 8.1: Switching probability as a function of the pulse duration obtained from analytical solution (line) and numerical solution (symbols) for a current density of $7.5 \cdot 10^6 \text{ A/cm}^2$. For the switching probability estimation, 1000 simulations were performed for each pulse width.

First the dependence of the switching statistics on the current density and pulse duration (Figure 8.1, Figure 8.2) is investigated. For that purpose 100 switching cycles under the current density $2.5 \cdot 10^6 \text{ A/cm}^2$, $5 \cdot 10^6 \text{ A/cm}^2$, and $7.5 \cdot 10^6 \text{ A/cm}^2$ and a pulse time of 30ns have been simulated. The state of the system at time intervals of

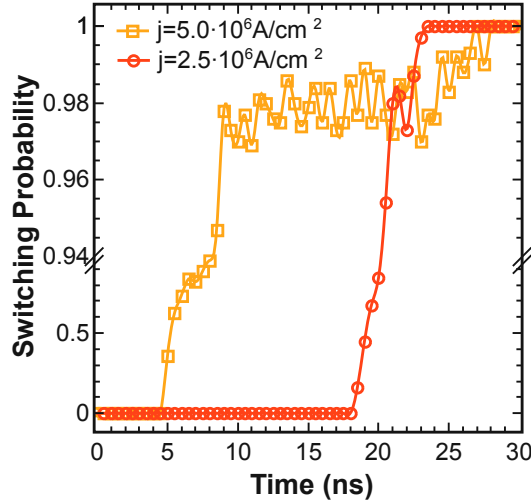


Figure 8.2: Switching probability as a function of the pulse duration for current densities $2.5 \cdot 10^6 \text{ A/cm}^2$ and $5 \cdot 10^6 \text{ A/cm}^2$. For switching probability estimation, 1000 simulations of switching were performed on each pulse width.

multiples of 0.5ns was taken, and for each of these states 10 relaxation processes under the influence of temperature were computed. This gave 1000 simulation realizations of the switching process for each pulse duration (multiple of 0.5ns) and for each of the three values of the current density for switching probability evaluation.

Figure 8.1 shows that for a current density $7.5 \cdot 10^6 \text{ A/cm}^2$ the numerical solution is in good agreement with the analytical expression:

$$P(t_p) = \exp(-\Delta \cdot \sin^2 \varphi). \quad (8.1)$$

Here, t_p is duration of the current pulse, Δ is the thermal stability factor. For φ the equation from [57] is used:

$$\varphi = \frac{\pi}{2} \exp\left(-\frac{\eta \mu_B}{e M_S d} (j - j_c) \cdot t_p\right). \quad (8.2)$$

Here, η is the spin polarization factor, μ_B is the Bohr's magneton, e is the electron charge, M_S is the saturation magnetizations, d is the thickness of the free layer, j_c is the critical current density, j is the current density ($j > j_c$).

Next, it was found that the switching probability for the current density $5 \cdot 10^6 \text{ A/cm}^2$ is equal to one when the pulse is longer than 26.5ns. This pulse duration is longer than the respective value of 23ns needed to achieve the ultimate switching at the current density $2.5 \cdot 10^6 \text{ A/cm}^2$ (Figure 8.2). Interestingly, for the current density $5 \cdot 10^6 \text{ A/cm}^2$ and a pulse duration between 8ns and 26.5ns the switching probability is less than one

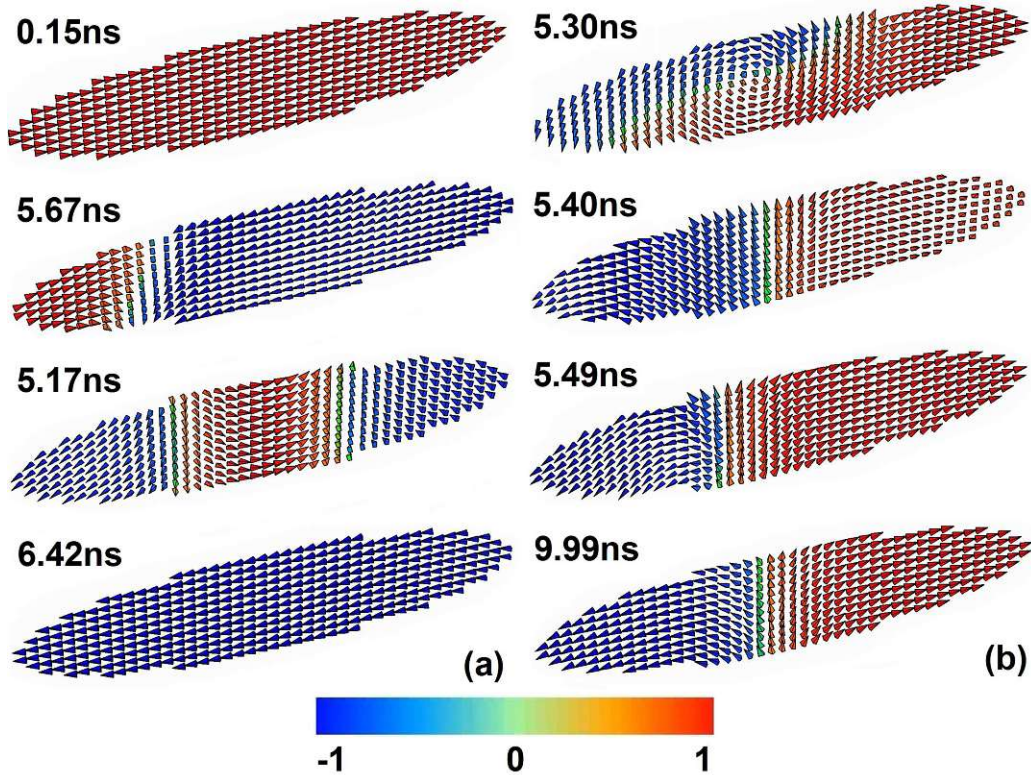


Figure 8.3: Snapshots of the switching process for a penta-layer MTJ: (a) normal switching process; (b) with transverse domain wall formation. The direction of the magnetization is shown by unit vectors, the color indicates the value of the component in direction of the long axis.

and fluctuates. This is in striking contrast to the earlier results, where the increasing pulse duration and current density always led to the switching probability increase [31]. To determine the reason for this discrepancy, the switching process is investigated in detail (Figure 8.3). It was found that during some of the switching realizations at the current density $5 \cdot 10^6 \text{ A/cm}^2$ a vortex is created (Figure 8.3b, 5.3ns). The formation of the vortex state in films thicker than 3.2nm is fully consistent with the results obtained previously for three-layer structures with a synthetic free layer [253]. After the vortex is formed, it transforms into a transverse domain wall (Figure 8.3b, 5.4ns). After that the transverse wall starts oscillating around the center of the free layer with an increasing amplitude (Figure 8.4a), which leads to the increase of the switching time. At a lower current density the domain wall is not formed and the switching proceeds normally (Figure 8.3a). The formation of the transverse domain wall is possible at higher currents, when the switching energy barrier for normal switching is practically equal to the formation energy barrier of the vortex/transverse domain wall state (Figure 8.4b).

Next, the validity of the criterion typically used to describe the 100% switching is

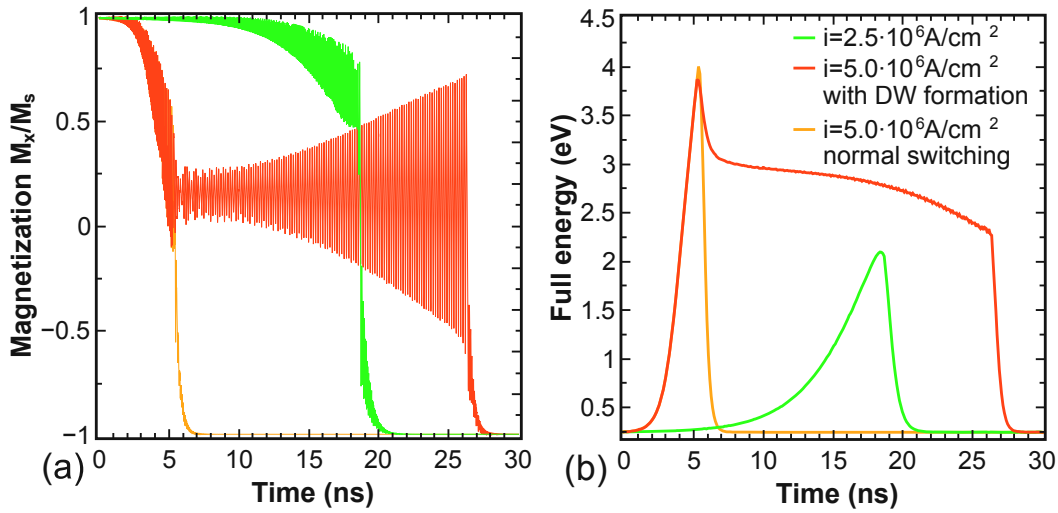


Figure 8.4: Averaged magnetization component in the direction of the long axis (a) and full energy (b) as a function of time. The current densities are shown in (b) for both cases.

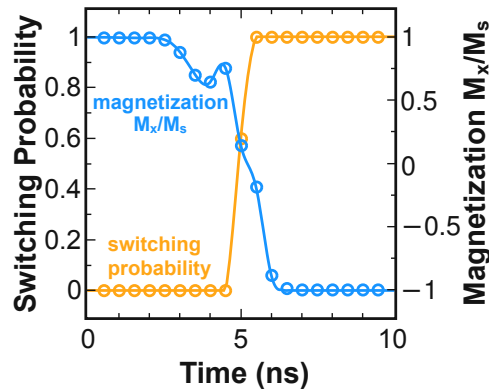


Figure 8.5: Switching probability vs. averaged magnetization component in the direction of the long axis as a function of time for normal switching.

investigated. As illustrated in Figure 8.5, in the case of normal switching from 1 to -1 the switching probability is defined to be 1 if the normalized average magnetization M_x/M_S along the long axis becomes less than -0.5 ($M_x/M_S < -0.5$) [31]. If, however, the vortex state is generated, due to the oscillatory behavior of the domain wall the 100% switching can be achieved even when $M_x/M_S > 0.5$ (Figure 8.6). This exception demonstrates that in making a decision about reliable switching one has to consider not only the average magnetization but also the state of the system during switching.

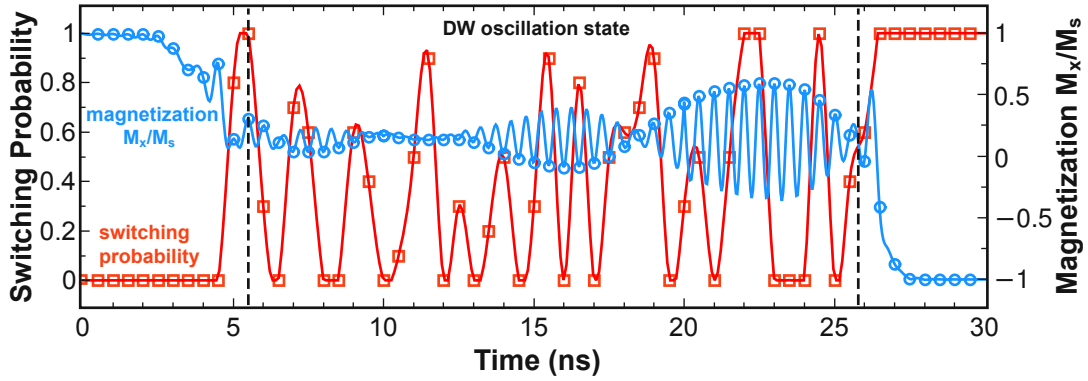


Figure 8.6: Switching probability vs. averaged magnetization component in the direction of the long axis as a function of time for switching with formation of the transverse domain wall.

8.2 MTJ-based Bias-Field-Free Spin-Torque Oscillator

Detected oscillations in the penta-layered structure are parasitic and undesirable phenomenon in structures used for MTJ-based memory. However, this effect can be utilized for spin-torque oscillators. Spin-torque oscillators together with STT-MRAM are the new types of spintronics devices utilizing all-electrical magnetization manipulation by current and have been intensely developed lately based on MgO-MTJs with a large magneto-resistance ratio [69].

Spin-torque oscillators based on MTJs with an in-plane magnetization [264] show high frequency capabilities, but still need an external magnetic field and/or are characterized by low output power level [212]. Oscillators on MTJs with perpendicular magnetization [263] and vortex-based oscillators [61] are shown to generate oscillations without an external magnetic field, however, their low operating frequencies, usually below 2GHz, limit their functionality and application as a tunable oscillator [212].

In this section two new concepts of bias-field-free spin-torque oscillators are proposed and discussed in details.

8.2.1 MTJ with half-elliptic reference layer

A penta-layer MTJ structure with only a half-ellipsis used as the reference layers (Figure 8.7) is investigated. The geometry of the device is a similar to that used in the previous section, namely CoFeB(20nm)/MgO(1nm)/CoFeB(3.5nm)/MgO(1nm)/CoFeB(20nm).

Figure 8.8 shows the oscillating process in such a structure in details. It was found that the structure with half-elliptic pinned layers, in contrast to the standard structure with the elliptic pinned layers, shows stable oscillations with nearly constant amplitude.

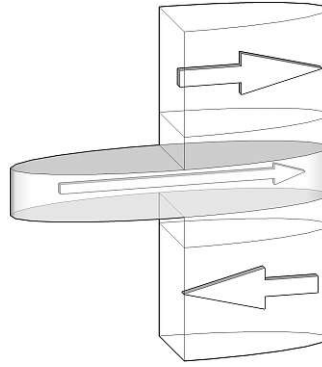


Figure 8.7: Schematic illustration of a penta-layer MTJ with half-elliptic pinned layers.

The Fourier transform of the signal is sharply peaked around the frequency ~ 6.785 GHz (Figure 8.9a).

The frequency of the oscillations only slightly depends on the current densities, as shown in Figure 8.9b.

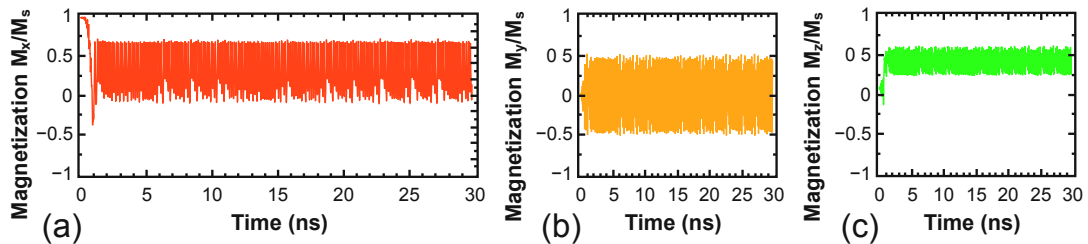


Figure 8.8: Magnetization components as a function of time: (a) x -component; (b) y -component; (c) z -component.

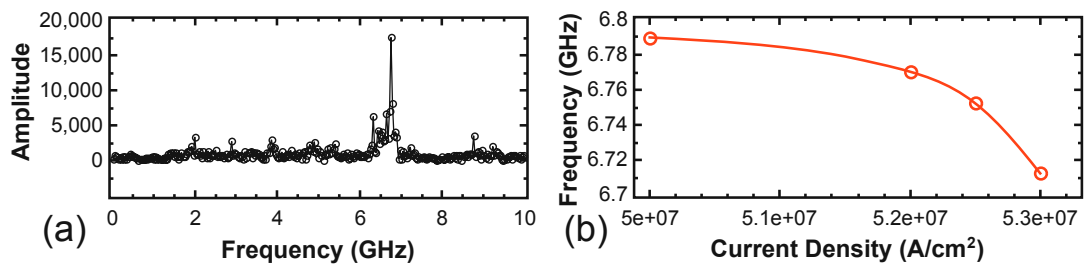


Figure 8.9: (a) Signal spectral density for the current density $j=5 \cdot 10^7$ A/cm². (b) Frequency as function of current density.

8.2.2 Two MTJs with shared free layer

Unfortunately the structure with half-elliptic reference layer proposed in the previous section, has one major drawback, namely a narrow range of current densities at which the oscillations are observed, which limits its use. This is due to the fact that despite the partial coverage of the free layer by the reference layers, resulting in the spin-current injection in only a part of the free layer, the free layer magnetization switching may still occur at higher currents.

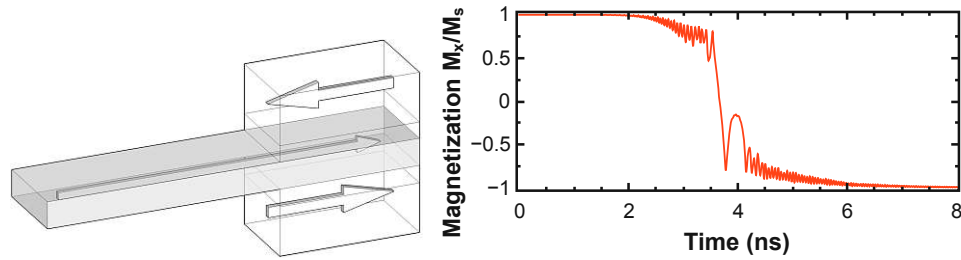


Figure 8.10: (left) Schematic illustration of a penta-layer MgO-MTJ without complete overlap of the free layer and the fixed layers. (right) Magnetization (x -component) as a function of time for a free layer of $70 \times 10 \text{ nm}^2$.

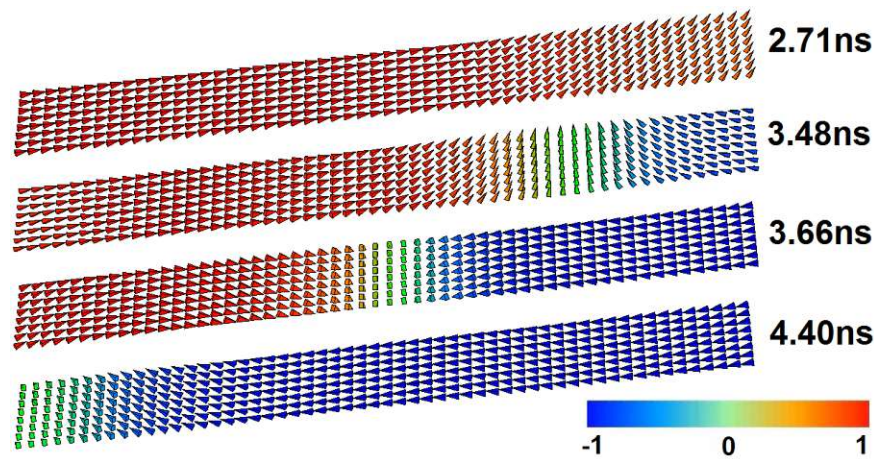


Figure 8.11: Snapshots of the switching process for a penta-layer MgO-MTJ without complete overlap of the free layer and the fixed layers. The direction of the magnetization is shown by unit vectors. The color indicates the value of the component along the long axis (x -axis).

In order to demonstrate this fact more clearly, the system consisting of CoFeB(5nm)/MgO(1nm)/CoFeB(3.5nm)/MgO(1nm)/CoFeB(5nm) MTJs, with the reference layers $20 \times 10 \text{ nm}^2$ ($a \times b$) and rectangular free layer $70 \times 10 \text{ nm}^2$ (Figure 8.10, left) is considered. Figure 8.10 (right) shows the dynamics of the magnetization component along the x -direction of the long axis as a function of time. The current density used for switching

is equal to $1 \cdot 10^7 \text{ A/cm}^2$. Despite that the fixed layer covers only a part of the free layer, so the injection of spin-current occurs in a part of the free layer only 20nm long, it is still possible to switch the free layer magnetization.

For demonstration of the switching process the magnetization dynamics of the free layer at different instances is shown in Figure 8.11. One can conclude that after applying the current a transversal domain wall is formed in the free magnetic layer close to the area of the spin-current injection, the motion of which away from the MTJ eventually switches the free layer.

In order to prevent the switching of the free layer and to favor an oscillatory behavior, a second MgO-MTJ is added to the system (Figure 8.12).

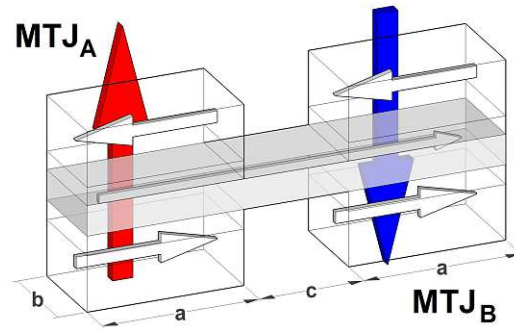


Figure 8.12: Schematic illustration of a spin-torque oscillator based on two MgO-MTJs with shared free layer. Colored arrows indicate the positive direction of the current for each of the MgO-MTJs.

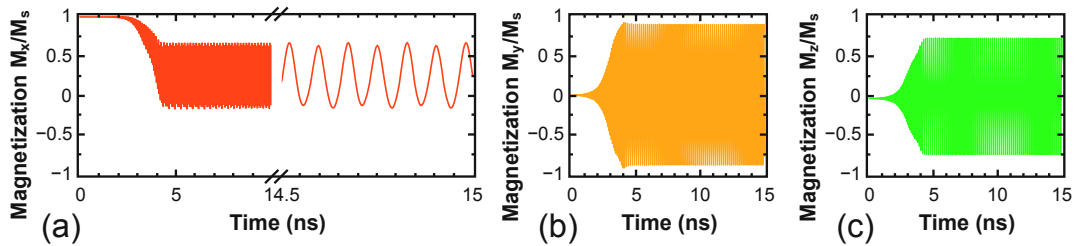


Figure 8.13: Magnetization components in MTJ_B as a function of time for a free layer of $50 \times 10 \text{ nm}^2$: (a) x -component; (b) y -component; (c) z -component. The current density through MTJ_A is $7.5 \cdot 10^7 \text{ A/cm}^2$ and $1 \cdot 10^7 \text{ A/cm}^2$ through MTJ_B .

First, the system with the free layer of a rectangular form with dimensions $50 \times 10 \text{ nm}^2$ ($c=10 \text{ nm}$), and the reference layer sizes to be the same as in the previous simulations ($20 \times 10 \text{ nm}^2$) is examined. The current density through the MTJ_A is $7.5 \cdot 10^7 \text{ A/cm}^2$ and $1 \cdot 10^7 \text{ A/cm}^2$ through the MTJ_B . Figure 8.13 shows the switching process in such a structure in detail. It is found that, in contrast to the previously considered structure, the structure with the two MgO-MTJs demonstrates stable oscillations with a constant amplitude. The Fourier transform of the signal is sharply peaked around the frequency of 13GHz (Figure 8.14).

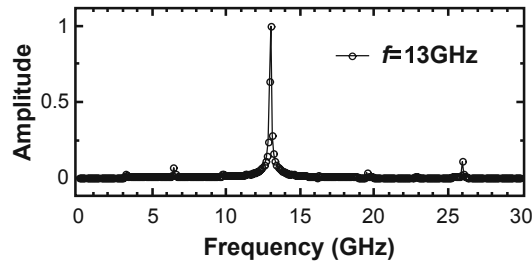


Figure 8.14: Signal spectral density normalized to its maximum value. The current density through MTJ_A is $7.5 \cdot 10^7$ A/cm² and $1 \cdot 10^7$ A/cm² through MTJ_B . The peak of the amplitude is observed at the frequency of 13GHz.

In order to understand the oscillations in such structures, the dynamics of the magnetization in MTJ_B in the pseudo macro-spin approximation (Figure 8.15) is considered. The pseudo macro-spin approximation includes the following actions: (i) the modeling of the magnetization dynamics was originally made as micromagnetic simulation; (ii) for MTJ_B the magnetization at each time is averaged over the area of MTJ_B .

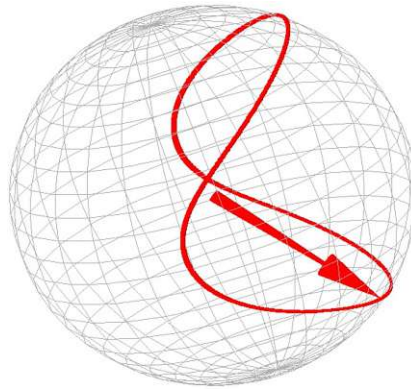


Figure 8.15: Pseudo macro-spin approximation of the oscillation trajectory in MTJ_B .

As can be seen, the cause of the high-frequency of oscillations in such structures, as compared with other structures that are experiencing oscillation without an external field, is that during each cycle the magnetization passes twice through the magnetization states with opposite direction.

Geometrical dependence of the oscillation regime appearance

One of the important issues for future practical applications of this concept of oscillators is finding the conditions under which the transition between the oscillating behavior to the complete switching occurs. To clarify this issue, the structures with free layer length from 45nm to 60nm (with 5nm step), and width equals to 10nm are investigated.

The current density through the MTJ_A is from $5 \cdot 10^6$ A/cm² to $1 \cdot 10^8$ A/cm² and from $5 \cdot 10^6$ A/cm² to $3.5 \cdot 10^7$ A/cm² through the MTJ_B .

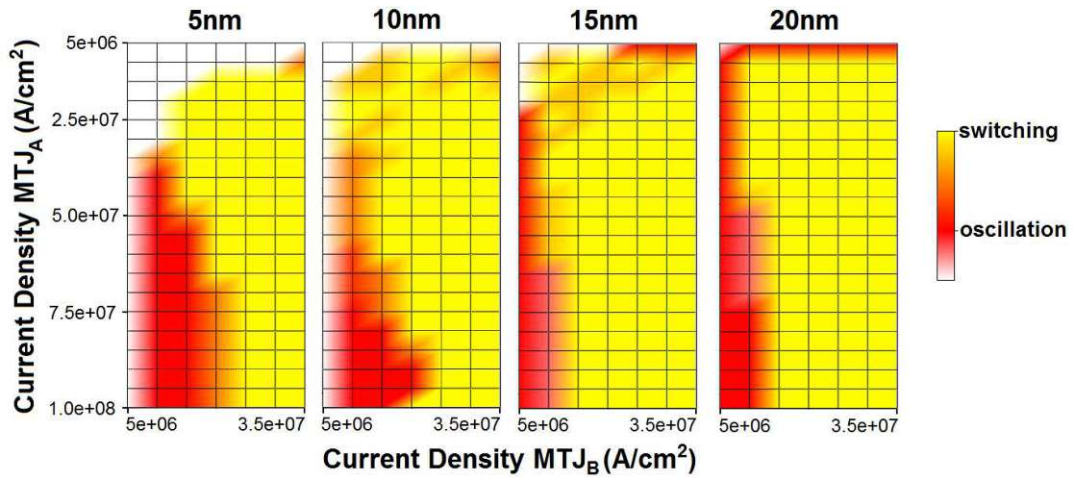


Figure 8.16: Schematic illustration of the geometrical dependence of the oscillation regime on the current densities through MTJ_A and MTJ_B . The dependences are shown for four lengths of the free layer: 45nm ($c=5$ nm), 50nm ($c=10$ nm), 55nm ($c=15$ nm), 60nm ($c=20$ nm).

The results (Figure 8.16) indicate that increasing the length of the free layer and thus the distance between the MgO-MTJs shifts the oscillation region towards larger j_a/j_b ratio. The white area in Figure 8.16 means that none of the types of behavior during the simulation time (15ns) was observed and the system presented its initial state.

The influence of current density and geometry on the oscillation frequency

Next, the influence of the current density j_a/j_b ratio on the oscillation frequency is studied. The structures with geometry of the free layer 60×10 nm² ($c=20$ nm) are examined. The current density through the MTJ_A varies from $1 \cdot 10^7$ to $5 \cdot 10^8$ A/cm², while in MTJ_B it is fixed to $5 \cdot 10^6$ A/cm². The simulation results shown (Figure 8.17), that increasing the ratio j_a/j_b increases the oscillation frequency.

Now the structures with a geometry of the free layer 50×10 nm² ($c=10$ nm) are investigated. The current densities through the MTJ_A vary from $1.5 \cdot 10^8$ to $2 \cdot 10^8$ A/cm², while through the MTJ_B from $1 \cdot 10^7$ to $3.5 \cdot 10^7$ A/cm². Increasing j_a leads to an increase of the range of j_b , where the stable oscillations are observed (Figure 8.18).

The output power depends on the oscillations amplitude $(m_{xmax} - m_{xmin})/2$, as it directly reflects the difference between the two extremes in the magnetization oscillations.

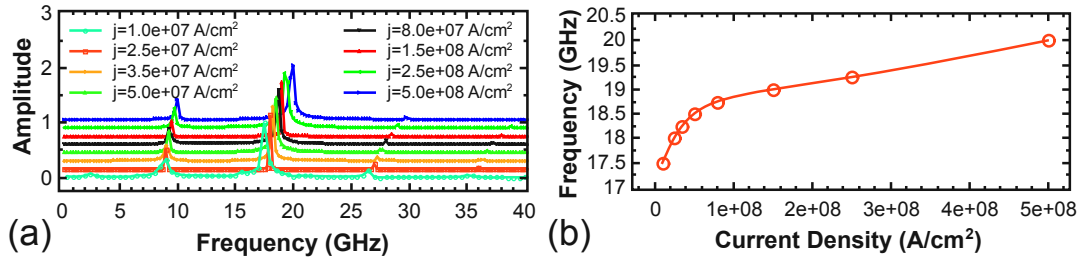


Figure 8.17: (a) Signal spectral density normalized to its maximum value. The length of the free layer is 60nm ($c=20$ nm). Current density through MTJ_A varies from $1 \cdot 10^7$ to $5 \cdot 10^8$ A/cm², while in MTJ_B it is fixed to $5 \cdot 10^6$ A/cm². For convenience the curves are shown with 0.15 offset in the amplitude for different values of the current density through MTJ_A . (b) Frequency as a function of current density.

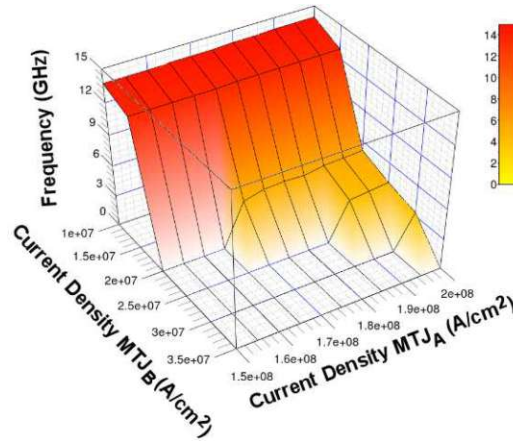


Figure 8.18: Frequency as a function of current densities in MTJ_A and MTJ_B . Current densities through MTJ_A vary from $1.5 \cdot 10^8$ to $2 \cdot 10^8$ A/cm², while through MTJ_B from $1 \cdot 10^7$ to $3.5 \cdot 10^7$ A/cm². The length of the free layer is 50nm ($c=10$ nm).

Figure 8.19 shows the simulation results for frequency and amplitude of the oscillations for different geometrical parameters: thickness of the free layer, short axis, distance between the MTJ_A and MTJ_B , MTJ_B long axis. The simulations demonstrate that a decrease of the distance c between the MTJ_A and MTJ_B , a decrease of the long axis a of the MTJ_B , and an increase of the short axis b and thicknesses of the free layer cause an increase of the frequency at the same current density. The oscillation amplitude depends on the geometry in the manner inverse to that of the frequency, except the variation of the short axis b and thicknesses of the free layer, which do not lead to noticeable changes in the amplitude of the oscillations. It is to note, that the variation of the long axis of the MTJ_A does not lead to a change in the frequency and amplitude of oscillations.

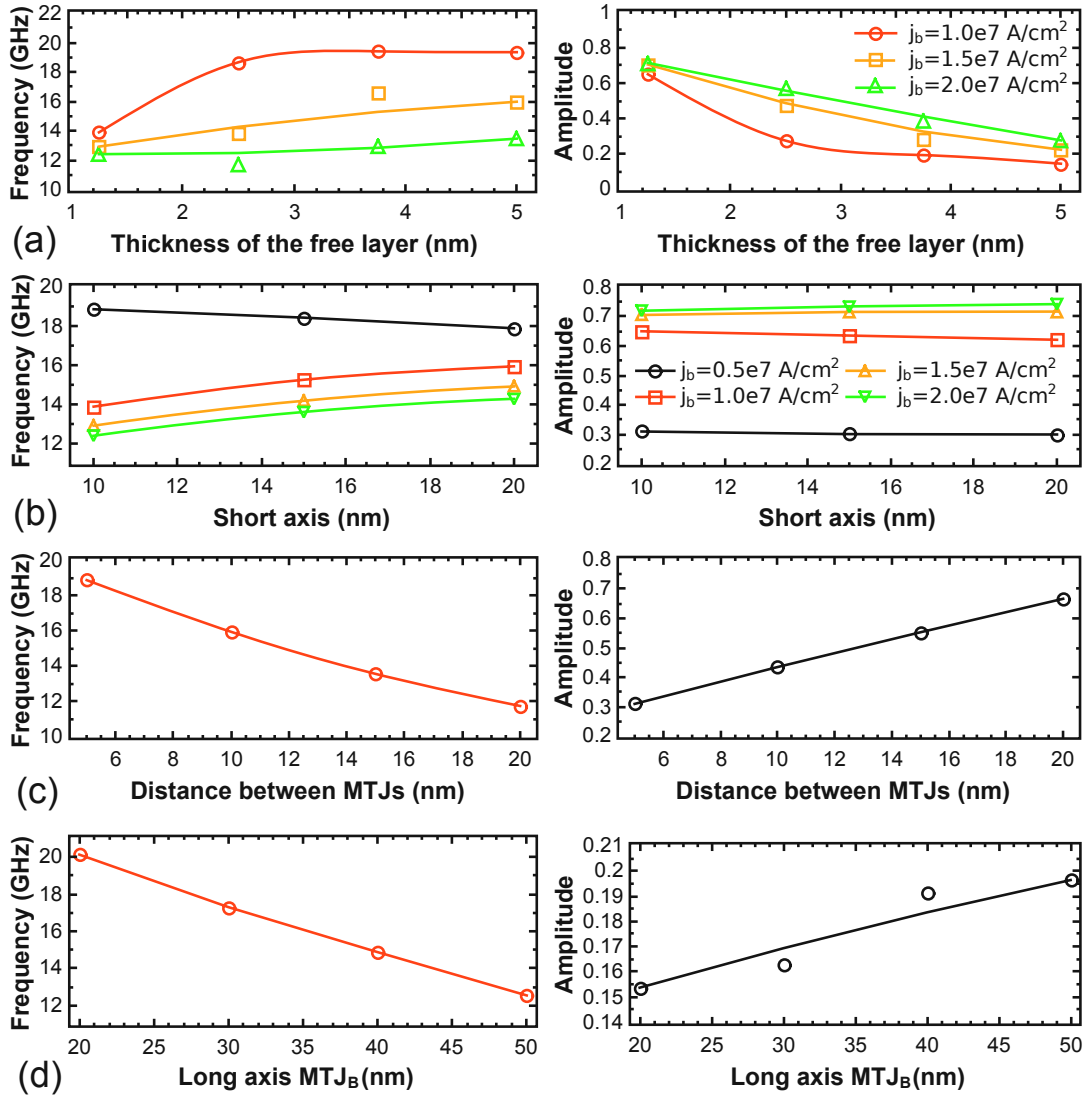


Figure 8.19: The influence of the device geometry on oscillation frequency: (a) thickness of the free layer; (b) short axis; (c) distance between MTJs; (d) long axis MTJ_B.

Structure optimization of the spin-torque oscillator

Using the simple dependences derived in the previous section showed that the structure of the free layer $45 \times 10 \times 1.25 \text{ nm}^3$ combines both high frequency and amplitude of oscillations (Figure 8.20). The current density through the MTJ_A is $5 \cdot 10^8 \text{ A/cm}^2$ and $2 \cdot 10^7 \text{ A/cm}^2$ through MTJ_B. The transition to the oscillation regime required less than 1ns. Figure 8.21 shows oscillation trajectory in the MTJ_B of this structure in the pseudo macro-spin approximation.

In what follows, the oscillations in a system composed of two three-layer MgO-MTJs

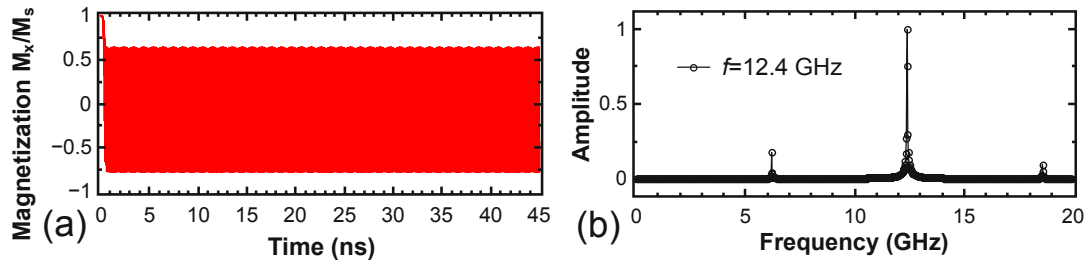


Figure 8.20: (a) Magnetization (x -component) as a function of time for free layer $45 \times 10 \times 1.25 \text{ nm}^3$. The current density through MTJ_A is $5 \cdot 10^8 \text{ A/cm}^2$ and $2 \cdot 10^7 \text{ A/cm}^2$ through MTJ_B . (b) Signal spectral density normalized to its maximum value. The peak of the amplitude is observed at a frequency of 12.4GHz.

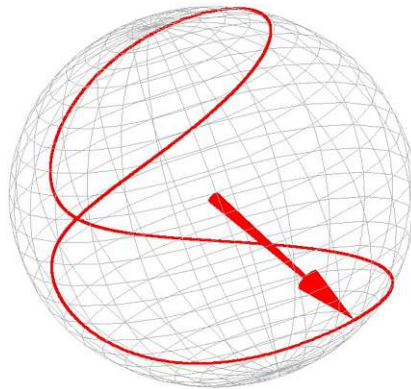


Figure 8.21: Pseudo macro-spin approximation of the oscillation trajectory in MTJ_B of the optimized structure.

with a shared free layer (Figure 8.22) are investigated. The structure geometry and the current densities are the same as for the previous oscillator.

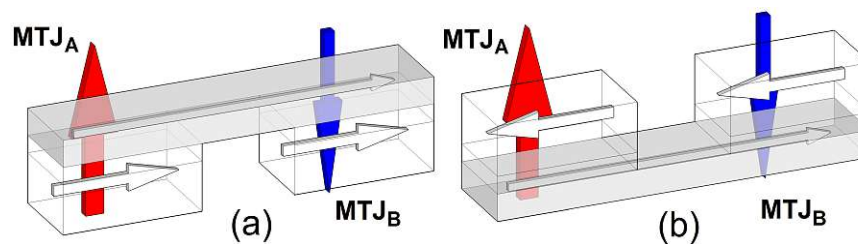


Figure 8.22: Schematic illustration of the two types of the oscillator based on two three-layer MgO-MTJs with shared free layer.

Both structures based on two three-layer MgO-MTJs with shared free layer (Figure 8.22a and Figure 8.22b), as well as structure based on two penta-layer MgO-MTJs (Figure 8.12), demonstrate stable oscillations. Figure 8.23 shows the signal spectral density normalized to its maximum value. The peaks of the amplitude are observed

at the frequencies of 10.3GHz and 17.7GHz for the structure (a) and (b), respectively. Note that the structure (b) shows an oscillation frequency higher than the conventional penta-layer structures and three-layer (a) at the same current densities. The reason is the in-plane magnetic field due to the pinned layers. In contrast to the conventional penta-layer MTJ, where the magnetostatic field is compensated, in the three-layer MTJ structure this field tries to reverse the magnetization in the structure (a) or to stabilize it in the structure (b). This results in an increase (decrease) of the operation frequency in the structure (b) (structure(a)) as compared to the conventional structure based on two penta-layer MgO-MTJs, making these structures attractive for tuning their frequency without biasing magnetic field.

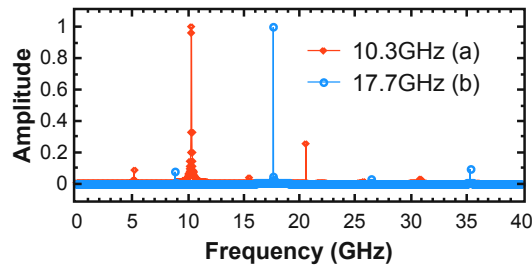


Figure 8.23: Signal spectral density normalized to its maximum value. The peak of the amplitude is observed at a frequency of 10.3GHz (structure (a)) and 17.7GHz (structure (b)).

9 Summary

Among the main results of the thesis are:

1. Introduction and development of a realistic stochastic model of the resistive switching. The dominance of stochastic processes in the RRAM operation degrades the reliability of this memory. This makes RRAM an unlikely candidate for universal memory development, at least in its current stage.
 2. Development of methods for achieving a symmetrical switching in asymmetric penta-layers MTJs structures.
 3. Introduction of a new concept of the free layer in the form of an in-plane composite free layer and its subsequent structural optimization. The discovered mechanism of switching acceleration and critical current reduction in STT-MRAM is general and does not depend on the magnetic material used for the free layer fabrication. This makes the proposed concepts of STT-MRAM with a composite free layer (C-MTJ and C2-MTJ) a good candidate for the development of future universal memory.
 4. Theoretical prediction of a new mechanism for switching failure in a MTJ-based STT-MRAM through formation of the vortex/transverse domain wall in a free layer.
 5. Introduction of two new concepts of a bias-field-free spin-torque oscillator.
- (1): The first full stochastic microscopic model of oxide resistive switching was developed. The main advantage of the stochastic model is that for the first time the movement of oxygen ions is taken into account. The distribution of the electron occupation probabilities calculated with the model is in good agreement with previous work. It has been shown that the process of rupture of the conductive filament is determined by the dynamics of oxygen ions and not only by the formation of the low occupation region. The simulated RRAM switching hysteresis cycle is in agreement with the experimental result. The main mechanism leading to the devices degradation and switching failure was identified.
- (2): By varying the thicknesses of the reference in-plane ferromagnetic layers and/or the separation between them, one can modulate the switching time and achieve an almost symmetric switching in asymmetric MTJs without an external magnetic field. The simulations also highlight the importance of the field acting perpendicular to the plane. This field facilitates switching. The proposed method is used for performance

optimization of STT-MRAM devices based on a dual MTJ with two barriers and ultra-thin dual MTJ cells.

(3): A new concept of a composite free layer (C-MTJ) was introduced. The composite magnetic layer consists of two half-ellipses separated by a non-magnetic spacer. As in p-MTJs, in MTJs with a composite free layer the switching barrier energy is practically equal to the thermal stability barrier. Due to the removal of the central region in the monolithic structure, the shape anisotropy is slightly decreased together with the thermal stability factor. To boost the thermal stability factor in composite structures it is sufficient to increase the thickness of the free layer and/or the aspect ratio, so the thermal stability factor exceeds that for p-MTJs demonstrated to date. An almost threefold decrease of the switching time in such structures has been found by simulation. Also a very narrow distribution of switching times is found for the proposed composite structure. In order to explain the distribution narrowing, the principles of the self-stabilization and self-acceleration of an MTJ with composite free layer switching were identified.

Furthermore, a new C2-MTJ structure with a composite free layer consisting of two ellipses with the axes $a/2$ and b inscribed into a rectangle $a \times b$ was proposed and analyzed. The simulations show that, while preserving all the advantages of the C-MTJ structure, such as fast switching, high thermal stability factor, and very narrow distribution of switching times, the newly proposed structure can be easier fabricated and offers a higher potential for STT-MRAM performance optimization. A very narrow distribution of switching times of C-MTJ and C2-MTJ structures is useful not only for application in a STT-MRAM memory cell, but also for magnetic sensors.

(4): Extensive simulations show that under certain conditions there is a non-negligible probability of the formation of a vortex state/transverse domain wall during switching. This results in a drastic increase in the switching time or can even lead to a complete switching failure. The detected switching failure mechanism must be taken into account in a realistic performance optimization of STT-MRAM devices.

In addition, an exception in the criterion typically used to describe the 100% switching was found. In the case of in-plane switching from 1 to -1 the switching probability is defined equal to 1 if the normalized average magnetization M_x/M_S along the long axis becomes less than -0.5 ($M_x/M_S < -0.5$). If, however, the vortex state is generated, 100% switching can be achieved even when $M_x/M_S > 0.5$. This exception demonstrates that one has to consider not only the average magnetization but also the state of the system during switching in taking decision about switching reliably.

(5): Methods for utilizing this parasitic switching effect to construct a spin-torque oscillator are shown. A newly proposed structure of the bias-field-free spin-torque oscillator has a form of a penta-layer MTJ structure with half-ellipsis reference layers. The structure with half-ellipsis reference layers develops stable oscillations with nearly constant amplitude. The Fourier transform of the signal is sharply peaked around

a frequency of $\sim 6.785\text{GHz}$. It is to note that the frequency of the oscillations only slightly depends on the current value.

Furthermore, a new concept of bias-field-free spin-torque oscillators based on two MTJs with a shared free layer, which show stable oscillations without any external magnetic field has been proposed. The operating frequency of the stable oscillations can be tuned in a wide range by varying the geometry of the MTJs and the current densities flowing through the MTJs, making this structure attractive for many high frequency applications.

Bibliography

- [1] S. E. Ahn, M.-J. Lee, Y. Park, B. S. Kang, C. B. Lee, K. H. Kim, S. Seo, D.-S. Suh, D.-C. Kim, J. Hur, W. Xianyu, G. Stefanovich, H. Yin, I.-K. Yoo, J.-H. Lee, J.-B. Park, I. G. Baek, and B. H. Park. Write Current Reduction in Transition Metal Oxide Based Resistance Change Memory. *Advanced Materials*, 20(5):924–928, 2008.
- [2] G. Albuquerque. *Magnetization Precession in Confined Geometry: Physical and Numerical Aspects*. PhD thesis, Paris-Sud University, Orsay, 2002.
- [3] D. Apalkov, S. Watts, A. Driskill-Smith, E. Chen, Z. Diao, and V. Nikitin. Comparison of Scaling of In-Plane and Perpendicular Spin Transfer Switching Technologies by Micromagnetic Simulation. *IEEE Transactions on Magnetics*, 46(6):2240–2243, 2010.
- [4] D. Aurélio, L. Torres, and G. Finocchio. Magnetization Switching Driven by Spin-Transfer-Torque in High-TMR Magnetic Tunnel Junctions. *Journal of Magnetism and Magnetic Materials*, 321(23):3913–3920, 2009.
- [5] U. Avci, I. Ban, D. Kencke, and P. Chang. Floating Body Cell (FBC) Memory for 16-nm Technology with Low Variation on Thin Silicon and 10-nm BOX. In *Proceedings of the IEEE International SOI Conference*, pages 29–30, 2008.
- [6] I. G. Baek, M. Lee, S. Seo, M.-J. Lee, D. Seo, D. S. Suh, J. Park, S. Park, T. Kim, I. Yoo, U. in Chung, and J. Moon. Highly Scalable Nonvolatile Resistive Memory Using Simple Binary Oxide Driven by Asymmetric Unipolar Voltage Pulses. In *Proceedings of the IEEE International Electron Devices Meeting (IEDM)*, pages 587–590, 2004.
- [7] M. N. Baibich, J. M. Broto, A. Fert, F. N. Van Dau, F. Petroff, P. Etienne, G. Creuzet, A. Friederich, and J. Chazelas. Giant Magnetoresistance of (001)Fe/(001)Cr Magnetic Superlattices. *Physical Review Letters*, 61:2472–2475, 1988.
- [8] S. Balatti, S. Ambrogio, D. Gilmer, and D. Ielmini. Set Variability and Failure Induced by Complementary Switching in Bipolar RRAM. *IEEE Electron Device Letters*, 34(7):861–863, 2013.

- [9] I. Ban, U. Avci, D. Kencke, and P. Chang. A Scaled Floating Body Cell (FBC) Memory with High-k+ Metal Gate on Thin-Silicon and Thin-BOX for 16 nm Technology Node and Beyond". In *Proceedings of the Symposium on VLSI Technology (VLSIT)*, pages 92–93, 2008.
- [10] I. Ban, U. Avci, U. Shah, C. Barns, D. Kencke, and P. Chang. Floating Body Cell with Independently-Controlled Double Gates for High Density Memory. In *Proceedings of the IEEE International Electron Devices Meeting (IEDM)*, pages 1–4, 2006.
- [11] M. Bawedin, S. Cristoloveanu, and D. Flandre. Unusual Floating Body Effect in Fully Depleted MOSFETs. In *Proceedings of the IEEE International SOI Conference*, pages 151–152, 2004.
- [12] M. Bawedin, S. Cristoloveanu, and D. Flandre. A Capacitorless 1T-DRAM on SOI Based on Dynamic Coupling and Double-Gate Operation. *IEEE Electron Device Letters*, 29(7):795–798, 2008.
- [13] M. Bawedin, S. Cristoloveanu, J. Yun, and D. Flandre. A New Memory Effect (MSD) in Fully Depleted SOI MOSFETs. *Solid-State Electronics*, 49(9):1547–1555, 2005.
- [14] A. Beck, J. G. Bednorz, C. Gerber, C. Rossel, and D. Widmer. Reproducible Switching Effect in Thin Oxide Films for Memory Applications. *Applied Physics Letters*, 77(1):139–141, 2000.
- [15] R. S. Beech, J. A. Anderson, A. V. Pohm, and J. M. Daughton. Curie Point Written Magnetoresistive Memory. *Journal of Applied Physics*, 87(9):6403–6405, 2000.
- [16] L. Berger. Emission of Spin Waves by a Magnetic Multilayer Traversed by a Current. *Physical Review B*, 54:9353–9358, 1996.
- [17] D. V. Berkov. *Handbook of Magnetism and Advanced Magnetic Materials*, volume Micromagnetism, chapter Magnetization Dynamics Including Thermal Fluctuations: Basic Phenomenology, Fast Remagnetization Processes and Transitions Over High-energy Barriers. John Wiley & Sons, Ltd., 2007.
- [18] G. Bersuker, D. C. Gilmer, D. Veksler, P. Kirsch, L. Vandelli, A. Padovani, L. Larcher, K. McKenna, A. Shluger, V. Iglesias, M. Porti, and M. Nafria. Metal Oxide Resistive Memory Switching Mechanism Based on Conductive Filament Properties. *Journal of Applied Physics*, 110(12):124518, 2011.
- [19] G. Bersuker, J. Yum, V. Iglesias, M. Porti, M. Nafria, K. McKenna, A. Shluger, P. Kirsch, and R. Jammy. Grain Boundary-Driven Leakage Path Formation in HfO₂ Dielectrics. In *Proceedings of the European Solid-State Device Research Conference (ESSDERC)*, pages 333–336, 2010.

- [20] G. Bersuker, J. Yum, L. Vandelli, A. Padovani, L. Larcher, V. Iglesias, M. Porti, M. Nafria, K. McKenna, A. Shluger, P. Kirsch, and R. Jammy. Grain Boundary-Driven Leakage Path Formation in HfO_2 Dielectrics. *Solid-State Electronics*, 65-66:146–150, 2011.
- [21] E. Bertin, D. Halley, Y. Henry, N. Najjari, H. Majjad, M. Bowen, V. DaCosta, J. Arabski, and B. Doudin. Random Barrier Double-Well Model for Resistive Switching in Tunnel Barriers. *Journal of Applied Physics*, 109(8):083712, 2011.
- [22] K. P. Biju, X. Liu, S. Kim, S. Jung, J. Park, and H. Hwang. Coexistence of Filamentary and Homogeneous Resistive Switching in Graded WO_x Thin Films. *physica status solidi (RRL) – Rapid Research Letters*, 5(3):89–91, 2011.
- [23] G. Binasch, P. Grünberg, F. Saurenbach, and W. Zinn. Enhanced Magnetoresistance in Layered Magnetic Structures with Antiferromagnetic Interlayer Exchange. *Physical Review B*, 39:4828–4830, 1989.
- [24] A. Bobeck, R. F. Fischer, A. Perneski, J. Remeika, and L. Van Uiter. Application of Orthoferrites to Domain-Wall Devices. *IEEE Transactions on Magnetics*, 5(3):544–553, 1969.
- [25] M. Bocquet, D. Deleruyelle, C. Muller, and J.-M. Portal. Self-consistent Physical Modeling of Set/Reset Operations in Unipolar Resistive-Switching Memories. *Applied Physics Letters*, 98(26):263507, 2011.
- [26] M. Bowen, V. Cros, F. Petroff, A. Fert, C. Martínez Boubeta, J. L. Costa-Krämer, J. V. Anguita, A. Cebollada, F. Briones, J. M. de Teresa, L. Morellón, M. R. Ibarra, F. Güell, F. Peiró, and A. Cornet. Large Magnetoresistance in $\text{Fe}/\text{MgO}/\text{FeCo}(001)$ Epitaxial Tunnel Junctions on $\text{GaAs}(001)$. *Applied Physics Letters*, 79(11):1655–1657, 2001.
- [27] W. H. Butler, X.-G. Zhang, T. C. Schulthess, and J. M. MacLaren. Spin-Dependent Tunneling Conductance of $\text{Fe}|\text{MgO}|\text{Fe}$ Sandwiches. *Physical Review B*, 63:054416, 2001.
- [28] C. Cagli, D. Ielmini, F. Nardi, and A. Lacaíta. Evidence for Threshold Switching in the Set Process of NiO-Based RRAM and Physical Modeling for Set, Reset, Retention and Disturb Prediction. In *Proceedings of the IEEE International Electron Devices Meeting (IEDM)*, pages 1–4, 2008.
- [29] X. Cao, X. Li, X. Gao, W. Yu, X. Liu, Y. Zhang, L. Chen, and X. Cheng. Forming-Free Colossal Resistive Switching Effect in Rare-Earth-Oxide Gd_2O_3 Films for Memristor Applications. *Journal of Applied Physics*, 106(7):073723, 2009.
- [30] M. Carpentieri, G. Finocchio, B. Azzerboni, L. Torres, L. Lopez-Diaz, and E. Martinez. Effect of the Classical Ampere Field in Micromagnetic Computations of Spin Polarized Current-Driven Magnetization Processes. *Journal of Applied Physics*, 97(10):10C713, 2005.

- [31] M. Carpentieri, G. Finocchio, L. Torres, and B. Azzerboni. Modeling of Fast Switching Processes in Nanoscale Spin Valves. *Journal of Applied Physics*, 103(7):07B117, 2008.
- [32] S. C. Chae, J. S. Lee, S. Kim, S. B. Lee, S. H. Chang, C. Liu, B. Kahng, H. Shin, D.-W. Kim, C. U. Jung, S. Seo, M.-J. Lee, and T. W. Noh. Random Circuit Breaker Network Model for Unipolar Resistance Switching. *Advanced Materials*, 20(6):1154–1159, 2008.
- [33] S. H. Chang, J. S. Lee, S. C. Chae, S. B. Lee, C. Liu, B. Kahng, D.-W. Kim, and T. W. Noh. Occurrence of Both Unipolar Memory and Threshold Resistance Switching in a NiO Film. *Physical Review Letters*, 102:026801, 2009.
- [34] W.-Y. Chang, Y.-C. Lai, T.-B. Wu, S.-F. Wang, F. Chen, and M.-J. Tsai. Unipolar Resistive Switching Characteristics of ZnO Thin Films for Nonvolatile Memory Applications. *Applied Physics Letters*, 92(2):022110, 2008.
- [35] C. Chappert, A. Fert, and F. N. Van Dau. The Emergence of Spin Electronics in Data Storage. *Nature Materials*, 6(11):813–823, 2007.
- [36] B. Chen, Y. Lu, B. Gao, Y. H. Fu, F. Zhang, P. Huang, Y. Chen, L. Liu, X. Liu, J. Kang, Y. Y. Wang, Z. Fang, H. Y. Yu, X. Li, X. Wang, N. Singh, G. Q. Lo, and D.-L. Kwong. Physical Mechanisms of Endurance Degradation in TMO-RRAM. In *Proceedings of the IEEE International Electron Devices Meeting (IEDM)*, pages 12.3.1–12.3.4, 2011.
- [37] Y.-S. Chen, T.-Y. Wu, P.-J. Tzeng, P.-S. Chen, H.-Y. Lee, C.-H. Lin, P.-S. Chen, and M.-J. Tsai. Forming-Free HfO₂ Bipolar RRAM Device with Improved Endurance and High Speed Operation. In *Proceedings of the International Symposium on VLSI Technology, Systems, and Applications (VLSI-TSA)*, pages 37–38, 2009.
- [38] Y. Y. Chen, G. Pourtois, C. Adelman, L. Goux, B. Govoreanu, R. Degreave, M. Jurczak, J. A. Kittl, G. Groeseneken, and D. J. Wouters. Insights into Ni-Filament Formation in Unipolar-Switching Ni/HfO₂/TiN Resistive Random Access Memory Device. *Applied Physics Letters*, 100(11):113513, 2012.
- [39] W. Chien, F. Lee, Y. Lin, Y. Chen, M. Lee, H. Lung, K. Hsieh, and C.-Y. Lu. Current Status and Future Challenges of Resistive Switching Memories. In *Extended Abstracts of the 2011 International Conference on Solid State Devices and Materials (SSDM)*, pages 1003–1004, 2011.
- [40] W. Chien, F. M. Lee, Y. Y. Lin, M. H. Lee, S. H. Chen, C. C. Hsieh, E. K. Lai, H. H. Hui, Y. K. Huang, C. C. Yu, C. Chen, H. L. Lung, K. Y. Hsieh, and C.-Y. Lu. Multi-layer Sidewall WO_x Resistive Memory Suitable for 3D ReRAM. In *Proceedings of the Symposium on VLSI Technology (VLSIT)*, pages 153–154, 2012.

- [41] B. J. Choi, D. S. Jeong, S. K. Kim, C. Rohde, S. Choi, J. H. Oh, H. J. Kim, C. S. Hwang, K. Szot, R. Waser, B. Reichenberg, and S. Tiedke. Resistive Switching Mechanism of TiO_2 Thin Films Grown by Atomic-layer Deposition. *Journal of Applied Physics*, 98(3):033715, 2005.
- [42] J. S. Choi, J.-S. Kim, I. R. Hwang, S. H. Hong, S. H. Jeon, S.-O. Kang, B. H. Park, D. C. Kim, M. J. Lee, and S. Seo. Different Resistance Switching Behaviors of NiO Thin Films Deposited on Pt and SrRuO_3 Electrodes. *Applied Physics Letters*, 95(2):022109, 2009.
- [43] F. Chudnovskii, L. Odynets, A. Pergament, and G. Stefanovich. Electroforming and Switching in Oxides of Transition Metals: The Role of Metal–Insulator Transition in the Switching Mechanism. *Journal of Solid State Chemistry*, 122(1):95–99, 1996.
- [44] R. P. Cowburn. The Future of Universal Memory. *Materials Today*, 6(7–8):32–38, 2003.
- [45] S. Cristoloveanu, M. Bawedin, J. Wan, S. Chang, C. Navarro, A. Zaslavsky, C. Le Royer, F. Andrieu, N. Rodriguez, and F. Gamiz. Innovative Capacitorless SOI DRAMs. In *Proceedings of the IEEE International SOI Conference*, pages 1–2, 2012.
- [46] J. M. Daughton and A. V. Pohm. Design of Curie Point Written Magnetoresistance Random Access Memory Cells. *Journal of Applied Physics*, 93(10):7304–7306, 2003.
- [47] G. Dearnaley. Electronic Conduction Through Thin Unsaturated Oxide Layers. *Physics Letters A*, 25(10):760–761, 1967.
- [48] G. Dearnaley. A Theory of the Oxide-Coated Cathode. *Thin Solid Films*, 3(3):161–174, 1969.
- [49] G. Dearnaley, D. Morgan, and A. Stoneham. A Model for Filament Growth and Switching in Amorphous Oxide Films. *Journal of Non-Crystalline Solids*, 4(C):593–612, 1970.
- [50] G. Dearnaley, A. M. Stoneham, and D. V. Morgan. Electrical Phenomena in Amorphous Oxide Films. *Reports on Progress in Physics*, 33(3):1129–1191, 1970.
- [51] R. Degraeve, A. Fantini, S. Clima, B. Govoreanu, L. Goux, Y. Y. Chen, D. Wouters, P. Roussel, G. Kar, G. Pourtois, S. Cosemans, J. Kittl, G. Groeseneken, M. Jurczak, and L. Altimime. Dynamic ‘Hour Glass’ Model for SET and RESET in HfO_2 RRAM. In *Proceedings of the Symposium on VLSI Technology (VLSIT)*, pages 75–76, 2012.
- [52] R. Degraeve, L. Goux, S. Clima, B. Govoreanu, Y. Y. Chen, G. Kar, P. Rousse, G. Pourtois, D. Wouters, L. Altimime, M. Jurczak, G. Groeseneken, and J. Kittl. Modeling and Tuning the Filament Properties in RRAM Metal Oxide Stacks for

- Optimized Stable Cycling. In *Proceedings of the International Symposium on VLSI Technology, Systems, and Applications (VLSI-TSA)*, pages 1–2, 2012.
- [53] R. Degraeve, P. Roussel, L. Goux, D. Wouters, J. Kittl, L. Altimime, M. Jurczak, and G. Groeseneken. Generic Learning of TDDB Applied to RRAM for Improved Understanding of Conduction and Switching Mechanism Through Multiple Filaments. In *Proceedings of the IEEE International Electron Devices Meeting (IEDM)*, pages 28.4.1–28.4.4, 2010.
- [54] B. Derrida. An Exactly Soluble Non-equilibrium System: The Asymmetric Simple Exclusion Process. *Physics Reports*, 301(1–3):65–83, 1998.
- [55] J. Dewald, A. Pearson, W. Northover, and W. P. Jr. Semi-conducting Glasses. *Journal of the Electrochemical Society*, 109:C243, 1962.
- [56] Z. Diao, D. Apalkov, M. Pakala, Y. Ding, A. Panchula, and Y. Huai. Spin Transfer Switching and Spin Polarization in Magnetic Tunnel Junctions with MgO and AlO_x Barriers. *Applied Physics Letters*, 87(23):232502, 2005.
- [57] Z. Diao, Z. Li, S. Wang, Y. Ding, A. Panchula, E. Chen, L.-C. Wang, and Y. Huai. Spin-Transfer Torque Switching in Magnetic Tunnel Junctions and Spin-Transfer Torque Random Access Memory. *Journal of Physics: Condensed Matter*, 19(16):165209, 2007.
- [58] Z. Diao, A. Panchula, Y. Ding, M. Pakala, S. Wang, Z. Li, D. Apalkov, H. Nagai, A. Driskill-Smith, L.-C. Wang, E. Chen, and Y. Huai. Spin Transfer Switching in Dual MgO Magnetic Tunnel Junctions. *Applied Physics Letters*, 90(13):132508, 2007.
- [59] R. Dong, D. S. Lee, W. F. Xiang, S. J. Oh, D. J. Seong, S. H. Heo, H. J. Choi, M. J. Kwon, S. N. Seo, M. B. Pyun, M. Hasan, and H. Hwang. Reproducible Hysteresis and Resistive Switching in Metal-Cu_xO-Metal Heterostructures. *Applied Physics Letters*, 90(4):042107, 2007.
- [60] R. Dorrance, F. Ren, Y. Toriyama, A. Amin, C.-K. Yang, and D. Markovic. Scalability and Design-Space Analysis of a 1T-1MTJ Memory Cell. In *IEEE/ACM International Symposium on Nanoscale Architectures (NANOARCH)*, pages 32–36, 2011.
- [61] A. Dussaux, B. Georges, J. Grollier, V. Cros, A. Khvalkovskiy, A. Fukushima, M. Konoto, H. Kubota, K. Yakushiji, S. Yuasa, K. Zvezdin, K. Ando, and A. Fert. Large Microwave Generation from Current-Driven Magnetic Vortex Oscillators in Magnetic Tunnel Junctions. *Nature Communications*, 1:8, 2010.
- [62] M. Ertosun, H. Cho, P. Kapur, and K. Saraswat. A Nanoscale Vertical Double-Gate Single-Transistor Capacitorless DRAM. *IEEE Electron Device Letters*, 29(6):615–617, 2008.

- [63] L. eun Yu, S. Kim, M.-K. Ryu, S.-Y. Choi, and Y.-K. Choi. Structure Effects on Resistive Switching of Devices for RRAM Applications. *IEEE Electron Device Letters*, 29(4):331–333, 2008.
- [64] G. Finocchio, B. Azzarboni, G. D. Fuchs, R. A. Buhrman, and L. Torres. Micromagnetic Modeling of Magnetization Switching Driven by Spin-Polarized Current in Magnetic Tunnel Junctions. *Journal of Applied Physics*, 101(6):063914, 2007.
- [65] G. Finocchio, M. Carpentieri, B. Azzarboni, L. Torres, E. Martinez, and L. Lopez-Diaz. Micromagnetic Simulations of Nanosecond Magnetization Reversal Processes in Magnetic Nanopillar. *Journal of Applied Physics*, 99(8):08G522, 2006.
- [66] G. D. Fuchs, I. N. Krivorotov, P. M. Braganca, N. C. Emley, A. G. F. Garcia, D. C. Ralph, and R. A. Buhrman. Adjustable Spin Torque in Magnetic Tunnel Junctions with Two Fixed Layers. *Applied Physics Letters*, 86(15):152509, 2005.
- [67] T. Fujii, M. Kawasaki, A. Sawa, H. Akoh, Y. Kawazoe, and Y. Tokura. Hysteretic Current–Voltage Characteristics and Resistance Switching at an Epitaxial Oxide Schottky Junction SrRuO₃/SrTi_{0.99}Nb_{0.01}O₃. *Applied Physics Letters*, 86(1):012107, 2005.
- [68] M. Fujimoto, H. Koyama, M. Konagai, Y. Hosoi, K. Ishihara, S. Ohnishi, and N. Awaya. TiO₂ Anatase Nanolayer on TiN Thin Film Exhibiting High-Speed Bipolar Resistive Switching. *Applied Physics Letters*, 89(22):223509, 2006.
- [69] A. Fukushima, T. Seki, K. Yakushiji, H. Kubota, S. Yuasa, and K. Ando. Statistical Variance in Switching Probability of Spin-Torque Switching in MgO-MTJ. *IEEE Transactions on Magnetism*, 48(11):4344–4346, 2012.
- [70] B. Gao, J. Kang, Y. Chen, F. Zhang, B. Chen, P. Huang, L. Liu, X. Liu, Y. Y. Wang, X. A. Tran, Z. Wang, H. Yu, and A. Chin. Oxide-Based RRAM: Unified Microscopic Principle for Both Unipolar and Bipolar Switching. In *Proceedings of the IEEE International Electron Devices Meeting (IEDM)*, pages 17.4.1–17.4.4, 2011.
- [71] B. Gao, J. Kang, L. Liu, X. Liu, and B. Yu. A Physical Model for Bipolar Oxide-Based Resistive Switching Memory Based on Ion-Transport-Recombination Effect. *Applied Physics Letters*, 98(23):232108, 2011.
- [72] B. Gao, B. Sun, H. Zhang, L. Liu, X. Liu, R. Han, J. Kang, and B. Yu. Unified Physical Model of Bipolar Oxide-Based Resistive Switching Memory. *IEEE Electron Device Letters*, 30(12):1326–1328, 2009.
- [73] B. Gao, S. Yu, N. Xu, L. F. Liu, B. Sun, X. Liu, R. Han, J. Kang, B. Yu, and Y. Y. Wang. Oxide-Based RRAM Switching Mechanism: A New Ion-Transport-Recombination Model. In *Proceedings of the IEEE International Electron Devices Meeting (IEDM)*, pages 1–4, 2008.

- [74] B. Gao, H. Zhang, B. Chen, L. Liu, X. Liu, R. Han, J. Kang, Z. Fang, H. Yu, B. Yu, and D.-L. Kwong. Modeling of Retention Failure Behavior in Bipolar Oxide-Based Resistive Switching Memory. *IEEE Electron Device Letters*, 32(3):276–278, 2011.
- [75] J. L. García-Palacios and F. J. Lázaro. Langevin-Dynamics Study of the Dynamical Properties of Small Magnetic Particles. *Physical Review B*, 58:14937–14958, 1998.
- [76] J. Gibbons and W. Beadle. Switching Properties of Thin NiO Films. *Solid-State Electronics*, 7(11):785–790, 1964.
- [77] T. Gilbert. A Phenomenological Theory of Damping in Ferromagnetic Materials. *IEEE Transactions on Magnetism*, 40(6):3443–3449, 2004.
- [78] L. Goux, Y.-Y. Chen, L. Pantisano, X.-P. Wang, G. Groeseneken, M. Jurczak, and D. Wouters. On the Gradual Unipolar and Bipolar Resistive Switching of TiN/HfO₂/Pt Memory Systems. *Electrochemical and Solid-State Letters*, 13(6):G54–G56, 2010.
- [79] L. Goux, A. Fantini, G. Kar, Y. Chen, N. Jossart, R. Degraeve, S. Clima, B. Govoreanu, G. Lorenzo, G. Pourtois, D. Wouters, J. Kittl, L. Altimime, and M. Jurczak. Ultralow Sub-500nA Operating Current High-Performance TiN/Al₂O₃/HfO₂/Hf/TiN Bipolar RRAM Achieved Through Understanding-Based Stack-Engineering. In *Proceedings of the Symposium on VLSI Technology (VLSIT)*, pages 159–160, 2012.
- [80] J. Grollier, V. Cros, A. Hamzic, J. M. George, H. Jaffrès, A. Fert, G. Faini, J. Ben Youssef, and H. Legall. Spin-Polarized Current Induced Switching in Co/Cu/Co Pillars. *Applied Physics Letters*, 78(23):3663–3665, 2001.
- [81] T. Hamamoto and T. Ohsawa. Overview and Future Challenges of Floating Body RAM (FBRAM) Technology for 32nm Technology Node and Beyond. In *Proceedings of the European Solid-State Device Research Conference (ESSDERC)*, pages 25–29, 2008.
- [82] W. R. Hiatt and T. W. Hickmott. Bistable Switching in Niobium Oxide Diodes. *Applied Physics Letters*, 6(6):106–108, 1965.
- [83] T. W. Hickmott. Low-Frequency Negative Resistance in Thin Anodic Oxide Films. *Journal of Applied Physics*, 33(9):2669–2682, 1962.
- [84] T. W. Hickmott. Potential Distribution and Negative Resistance in Thin Oxide Films. *Journal of Applied Physics*, 35(9):2679–2689, 1964.
- [85] C. Ho, C.-L. Hsu, C.-C. Chen, J.-T. Liu, C.-S. Wu, C.-C. Huang, C. Hu, and F.-L. Yang. 9nm Half-Pitch Functional Resistive Memory Cell with <1 μA Programming Current Using Thermally Oxidized Sub-Stoichiometric WO_x Film. In

- Proceedings of the IEEE International Electron Devices Meeting (IEDM)*, pages 19.1.1–19.1.4, 2010.
- [86] S. Hong. Memory Technology Trend and Future Challenges. In *Proceedings of the IEEE International Electron Devices Meeting (IEDM)*, pages 12.4.1–12.4.4, 2010.
- [87] C.-W. Hsu, I.-T. Wang, C.-L. Lo, M.-C. Chiang, W.-Y. Jang, C.-H. Lin, and T.-H. Hou. Self-Rectifying Bipolar TaO_x/TiO₂ RRAM with Superior Endurance Over 10¹² Cycles for 3D High-Density Storage-Class Memory. In *Proceedings of the Symposium on VLSI Technology (VLSIT)*, pages T166–T167, 2013.
- [88] Y. Huai, F. Albert, P. Nguyen, M. Pakala, and T. Valet. Observation of Spin-Transfer Switching in Deep Submicron-Sized and Low-Resistance Magnetic Tunnel Junctions. *Applied Physics Letters*, 84(16):3118–3120, 2004.
- [89] Y. Huai, M. Pakala, Z. Diao, and Y. Ding. Spin Transfer Switching Current Reduction in Magnetic Tunnel Junction Based Dual Spin Filter Structures. *Applied Physics Letters*, 87(22):222510, 2005.
- [90] P. Huang, Y. Deng, B. Gao, B. Chen, F. Zhang, D. Yu, L. Liu, G. Du, J. Kang, and X. Liu. Optimization of Conductive Filament of Oxide-Based RRAM for Low Operation Current by Stochastic Simulation. In *Extended Abstracts of the 2012 International Conference on Solid State Devices and Materials (SSDM)*, pages 1–2, 2012.
- [91] P. Huang, B. Gao, B. Chen, F. Zhang, L. Liu, G. Du, J. Kang, and X. Liu. Stochastic Simulation of Forming, SET and RESET Process for Transition Metal Oxide-Based Resistive Switching Memory. In *Proceedings of the International Conference on Simulation of Semiconductor Processes and Devices (SISPAD)*, pages 312–315, 2012.
- [92] P. Huang, X. Liu, W. Li, Y. Deng, B. Chen, Y. Lu, B. Gao, L. Zeng, K. Wei, G. Du, X. Zhang, and J. Kang. A Physical Based Analytic Model of RRAM Operation for Circuit Simulation. In *Proceedings of the IEEE International Electron Devices Meeting (IEDM)*, pages 26.6.1–26.6.4, 2012.
- [93] A. Hubert. μ MAG Standard Problem.
Internet: <http://www.ctcms.nist.gov/~rdm/spec3.html>.
- [94] A. Hubert, S. Cristoloveanu, M. Bawedin, and T. Ernst. Scalability of MSD Memory Effect. In *Proceedings of the International Conference on Ultimate Integration of Silicon (ULIS)*, pages 139–142, 2009.
- [95] I. Hwang, M.-J. Lee, G.-H. Buh, J. Bae, J. Choi, J.-S. Kim, S. Hong, Y. S. Kim, I. S. Byun, S.-W. Lee, S. E. Ahn, B. S. Kang, S.-O. Kang, and B. H. Park. Resistive Switching Transition Induced by a Voltage Pulse in a Pt/NiO/Pt Structure. *Applied Physics Letters*, 97(5):052106, 2010.

- [96] D. Ielmini. Filamentary-Switching Model in RRAM for Time, Energy and Scaling Projections. In *Proceedings of the IEEE International Electron Devices Meeting (IEDM)*, pages 17.2.1–17.2.4, 2011.
- [97] D. Ielmini. Modeling the Universal Set/Reset Characteristics of Bipolar RRAM by Field- and Temperature-Driven Filament Growth. *IEEE Transactions on Electron Devices*, 58(12):4309–4317, 2011.
- [98] D. Ielmini, S. Larentis, and S. Balatti. A Physics-Based Model of Resistive Switching in Metal Oxides. In *Extended Abstracts of the 2012 International Conference on Solid State Devices and Materials (SSDM)*, pages 1–2, 2012.
- [99] D. Ielmini, F. Nardi, and C. Cagli. Physical Models of Size-Dependent Nanofilament Formation and Rupture in NiO Resistive Switching Memories. *Nanotechnology*, 22(25):254022, 2011.
- [100] S. Ikeda, J. Hayakawa, Y. Ashizawa, Y. M. Lee, K. Miura, H. Hasegawa, M. Tsunoda, F. Matsukura, and H. Ohno. Tunnel Magnetoresistance of 604% at 300K by Suppression of Ta Diffusion in CoFeB/MgO/CoFeB Pseudo-Spin-Valves Annealed at High Temperature. *Applied Physics Letters*, 93(8):082508, 2008.
- [101] S. Ikeda, K. Miura, H. Yamamoto, K. Mizunuma, H. D. Gan, M. Endo, S. Kanai, J. Hayakawa, F. Matsukura, and H. Ohno. A Perpendicular-Anisotropy CoFeB–MgO Magnetic Tunnel Junction. *Nature Materials*, 9(9):721–724, 2010.
- [102] H. Imamura and S. Maekawa. *Handbook of Magnetism and Advanced Magnetic Materials*, volume Fundamentals and Theory, chapter Theory of Spin-dependent Tunneling. John Wiley & Sons, Ltd., 2007.
- [103] K. Ito, T. Devolder, C. Chappert, M. J. Carey, and J. A. Katine. Probabilistic Behavior in Subnanosecond Spin Transfer Torque Switching. *Journal of Applied Physics*, 99(8):08G519, 2006.
- [104] ITRS. International technology roadmap for semiconductors. 2012 Edition. Internet: <http://www.itrs.net/>.
- [105] M. Iwayama, T. Kai, M. Nakayama, H. Aikawa, Y. Asao, T. Kajiyama, S. Ikegawa, H. Yoda, and A. Nitayama. Reduction of Switching Current Distribution in Spin Transfer Magnetic Random Access Memories. *Journal of Applied Physics*, 103(7):07A720, 2008.
- [106] M. Janousch, G. Meijer, U. Staub, B. Delley, S. Karg, and B. Andreasson. Role of Oxygen Vacancies in Cr-Doped SrTiO₃ for Resistance-Change Memory. *Advanced Materials*, 19(17):2232–2235, 2007.
- [107] D. Jeong, H. Schroeder, and R. Waser. Coexistence of Bipolar and Unipolar Resistive Switching Behaviors in a Pt/TiO₂/Pt Stack. *Electrochemical and Solid-State Letters*, 10(8):G51–G53, 2007.

- [108] D. Jeong, R. Thomas, R. Katiyar, J. Scott, H. Kohlstedt, A. Petraru, and C. Hwang. Emerging Memories: Resistive Switching Mechanisms and Current Status. *Reports on Progress in Physics*, 75(7), 2012.
- [109] D. S. Jeong, H. Schroeder, U. Breuer, and R. Waser. Characteristic Electroforming Behavior in Pt/TiO₂/Pt Resistive Switching Cells Depending on Atmosphere. *Journal of Applied Physics*, 104(12):123716, 2008.
- [110] K. W. Jeong, Y. H. Do, K. S. Yoon, C. O. Kim, and J. P. Hong. Resistive Switching Characteristics of Unique Binary-Oxide MgO_x Films. *Journal of the Korean Physical Society*, 48(6):1501–1504, 2006.
- [111] M. Julliere. Tunneling Between Ferromagnetic Films. *Physics Letters A*, 54(3):225–226, 1975.
- [112] A. Kákay. *Numerical Investigations of Micromagnetic Structures*. PhD thesis, Research Institute for Solid State Physics and Optics, Hungarian Academy of Sciences, 2005.
- [113] A. Kalantarian, G. Bersuker, B. Butcher, D. Gilmer, S. Privitera, S. Lombardo, R. Geer, Y. Nishi, P. Kirsch, and R. Jammy. Microscopic Model for the Kinetics of the Reset Process in HfO₂ RRAM. In *Proceedings of the International Symposium on VLSI Technology, Systems, and Applications (VLSI-TSA)*, pages 1–2, 2013.
- [114] K. Kamiya, M. Yang, B. Magyari-Kope, M. Niwa, Y. Nishi, and K. Shiraishi. Physics in Designing Desirable ReRAM Stack Structure – Atomistic Recipes Based on Oxygen Chemical Potential Control and Charge Injection/Removal. In *Proceedings of the IEEE International Electron Devices Meeting (IEDM)*, pages 20.2.1–20.2.4, 2012.
- [115] K. Kamiya, M. Y. Yang, B. Magyari-Köpe, M. Niwa, Y. Nishi, and K. Shiraishi. Theoretical Design of Desirable Stack Structure for Resistive Random Access Memories. *ECS Transactions*, 58:181–188, 2013.
- [116] K. Kamiya, M. Y. Yang, B. Magyari-Kope, M. Niwa, Y. Nishi, and K. Shiraishi. Vacancy Cohesion-Isolation Phase Transition Upon Charge Injection and Removal in Binary Oxide-Based RRAM Filamentary-Type Switching. *IEEE Transactions on Electron Devices*, 60(10):3400–3406, 2013.
- [117] J. A. Katine, F. J. Albert, R. A. Buhrman, E. B. Myers, and D. C. Ralph. Current-Driven Magnetization Reversal and Spin-Wave Excitations in Co/Cu/Co Pillars. *Physical Review Letters*, 84:3149–3152, 2000.
- [118] A. D. Kent, B. Özyilmaz, and E. del Barco. Spin-Transfer-Induced Precessional Magnetization Reversal. *Applied Physics Letters*, 84(19):3897–3899, 2004.

- [119] A. Khvalkovskiy, D. Apalkov, S. Watts, R. Chepulskii, R. Beach, A. Ong, X. Tang, A. Driskill-Smith, W. H. Butler, P. Visscher, D. Lottis, E. Chen, V. Nikitin, and M. Krounbi. Basic Principles of STT-MRAM Cell Operation in Memory Arrays. *Journal of Physics D: Applied Physics*, 46(8):074001, 2013.
- [120] D. C. Kim, S. Seo, S. E. Ahn, D.-S. Suh, M. J. Lee, B.-H. Park, I. K. Yoo, I. G. Baek, H.-J. Kim, E. K. Yim, J. E. Lee, S. O. Park, H. S. Kim, U.-I. Chung, J. T. Moon, and B. I. Ryu. Electrical Observations of Filamentary Conductions for the Resistive Memory Switching in NiO Films. *Applied Physics Letters*, 88(20):202102, 2006.
- [121] K. Kim, B. Choi, S. Song, G. Kim, and C. Hwang. Filamentary Resistive Switching Localized at Cathode Interface in NiO Thin Films. *Journal of the Electrochemical Society*, 156(12):G213–G216, 2009.
- [122] K. M. Kim, B. J. Choi, B. W. Koo, S. Choi, D. S. Jeong, and C. S. Hwang. Resistive Switching in Pt/Al₂O₃/TiO₂/Ru Stacked Structures. *Electrochemical and Solid-State Letters*, 9(12):G343–G346, 2006.
- [123] K. M. Kim, B. J. Choi, Y. C. Shin, S. Choi, and C. S. Hwang. Anode-Interface Localized Filamentary Mechanism in Resistive Switching of TiO₂ Thin Films. *Applied Physics Letters*, 91(1):012907, 2007.
- [124] K. M. Kim and C. S. Hwang. The Conical Shape Filament Growth Model in Unipolar Resistance Switching of TiO₂ Thin Film. *Applied Physics Letters*, 94(12):122109, 2009.
- [125] K. M. Kim, D. S. Jeong, and C. S. Hwang. Nanofilamentary Resistive Switching in Binary Oxide System; a Review on the Present Status and Outlook. *Nanotechnology*, 22(25):254002, 2011.
- [126] K. M. Kim, M. H. Lee, G. H. Kim, S. J. Song, J. Y. Seok, J. H. Yoon, and C. S. Hwang. Understanding Structure-Property Relationship of Resistive Switching Oxide Thin Films Using a Conical Filament Model. *Applied Physics Letters*, 97(16):162912, 2010.
- [127] M. Kim, I. G. Baek, Y. Ha, S. Baik, J. Kim, D. J. Seong, S. Kim, Y. Kwon, C. R. Lim, H.-K. Park, D. Gilmer, P. Kirsch, R. Jammy, Y. Shin, S. Choi, and C. Chung. Low Power Operating Bipolar TMO ReRAM for Sub 10 nm Era. In *Proceedings of the IEEE International Electron Devices Meeting (IEDM)*, pages 19.3.1–19.3.4, 2010.
- [128] S. Kim and Y.-K. Choi. A Comprehensive Study of the Resistive Switching Mechanism in Al/TiO_x/TiO₂/Al-Structured RRAM. *IEEE Transactions on Electron Devices*, 56(12):3049–3054, 2009.

- [129] S. Kim, X. Liu, J. Park, S. Jung, W. Lee, J. Woo, J. Shin, G. Choi, C. Cho, S. Park, D. Lee, E. jun Cha, B.-H. Lee, H. D. Lee, S. G. Kim, S. Chung, and H. Hwang. Ultrathin ($<10\text{nm}$) $\text{Nb}_2\text{O}_5/\text{NbO}_2$ Hybrid Memory with Both Memory and Selector Characteristics for High Density 3D Vertically Stackable RRAM Applications. In *Proceedings of the Symposium on VLSI Technology (VLSIT)*, pages 155–156, 2012.
- [130] W.-G. Kim and S.-W. Rhee. Effect of the Top Electrode Material on the Resistive Switching of TiO_2 Thin Film. *Microelectronic Engineering*, 87(2):98–103, 2010.
- [131] Y.-M. Kim and J.-S. Lee. Reproducible Resistance Switching Characteristics of Hafnium Oxide-Based Nonvolatile Memory Devices. *Journal of Applied Physics*, 104(11):114115, 2008.
- [132] K. Kinoshita, T. Tamura, M. Aoki, Y. Sugiyama, and H. Tanaka. Bias Polarity Dependent Data Retention of Resistive Random Access Memory Consisting of Binary Transition Metal Oxide. *Applied Physics Letters*, 89(10):103509, 2006.
- [133] K. Kinoshita, H. Tanaka, M. Yoshihara, and S. Kishida. Insight into Distribution and Switching of Resistive Random-Access Memory Filaments Based on Analysis of Variations in Memory Characteristics. *Journal of Applied Physics*, 112(4):044503, 2012.
- [134] A. N. Korotkov and K. K. Likharev. Shot Noise Suppression at One-Dimensional Hopping. *Physical Review B*, 61:15975–15987, 2000.
- [135] M. Kozicki, M. Park, and M. Mitkova. Nanoscale Memory Elements Based on Solid-State Electrolytes. *IEEE Transactions on Nanotechnology*, 4(3):331–338, 2005.
- [136] H. Kronmüller. *Handbook of Magnetism and Advanced Magnetic Materials*, volume Micromagnetism, chapter General Micromagnetic Theory. John Wiley & Sons, Ltd., 2007.
- [137] M. Kryder and C. S. Kim. After Hard Drives – What Comes Next? *IEEE Transactions on Magnetism*, 45(10):3406–3413, 2009.
- [138] C. Kugeler, C. Nauenheim, M. Meier, A. Rudiger, and R. Waser. Fast Resistance Switching of TiO_2 and MSQ Thin Films for Non-Volatile Memory Applications (RRAM). In *9th Annual Non-Volatile Memory Technology Symposium (NVMTS)*, pages 1–6, 2008.
- [139] D.-H. Kwon, K. Kim, J. Jang, J. Jeon, M. Lee, G. Kim, X.-S. Li, G.-S. Park, B. Lee, S. Han, M. Kim, and C. Hwang. Atomic Structure of Conducting Nanofilaments in TiO_2 Resistive Switching Memory. *Nature Nanotechnology*, 5(2):148–153, 2010.

- [140] M. Labrune and J. Miltat. Wall Structures in Ferro/Antiferromagnetic Exchange-Coupled Bilayers: A Numerical Micromagnetic Approach. *Journal of Magnetism and Magnetic Materials*, 151(1–2):231–245, 1995.
- [141] L. Landau and E. Lifshitz. On the Theory of the Dispersion of Magnetic Permeability in Ferromagnetic Bodies. *Physikalische Zeitschrift der Sowjetunion*, 8:153–169, 1935.
- [142] S. Larentis, F. Nardi, S. Balatti, D. Gilmer, and D. Ielmini. Resistive Switching by Voltage-Driven Ion Migration in Bipolar RRAM – Part II: Modeling. *IEEE Transactions on Electron Devices*, 59(9):2468–2475, 2012.
- [143] B. Lee, P. Zhou, J. Yang, Y. Zhang, B. Zhao, E. Ipek, O. Mutlu, and D. Burger. Phase-Change Technology and the Future of Main Memory. *IEEE Micro*, 30(1):143–143, 2010.
- [144] D. Lee, H. Choi, H. Sim, D. Choi, H. Hwang, M.-J. Lee, S.-A. Seo, and I. Yoo. Resistance Switching of the Nonstoichiometric Zirconium Oxide for Nonvolatile Memory Applications. *IEEE Electron Device Letters*, 26(10):719–721, 2005.
- [145] H. Lee, Y. S. Chen, P. Chen, P. Gu, Y. Hsu, S. Wang, W. Liu, C. Tsai, S. Sheu, P.-C. Chiang, W. Lin, C. H. Lin, W.-S. Chen, F. Chen, C. Lien, and M. Tsai. Evidence and Solution of Over-RESET Problem for HfO_x Based Resistive Memory with Sub-ns Switching Speed and High Endurance. In *Proceedings of the IEEE International Electron Devices Meeting (IEDM)*, pages 19.7.1–19.7.4, 2010.
- [146] H. Y. Lee, P. S. Chen, T. Y. Wu, C. C. Wang, P. J. Tzeng, C. H. Lin, F. Chen, M.-J. Tsai, and C. Lien. Electrical Evidence of Unstable Anodic Interface in Ru/HfO_x/TiN Unipolar Resistive Memory. *Applied Physics Letters*, 92(14):142911, 2008.
- [147] K. Lee, J.-S. Jang, Y. Kwon, K.-H. Lee, Y.-K. Park, and W. Y. Choi. A Unified Model for Unipolar Resistive Random Access Memory. *Applied Physics Letters*, 100(8):083509, 2012.
- [148] K.-J. Lee and B. Dieny. Micromagnetic Investigation of the Dynamics of Magnetization Switching Induced by a Spin Polarized Current. *Applied Physics Letters*, 88(13):132506, 2006.
- [149] S. Lee, H. Kim, D.-J. Yun, S.-W. Rhee, and K. Yong. Resistive Switching Characteristics of ZnO Thin Film Grown on Stainless Steel for Flexible Nonvolatile Memory Devices. *Applied Physics Letters*, 95(26):262113, 2009.
- [150] S. B. Lee, S. C. Chae, S. H. Chang, J. S. Lee, S. Seo, B. Kahng, and T. W. Noh. Scaling Behaviors of Reset Voltages and Currents in Unipolar Resistance Switching. *Applied Physics Letters*, 93(21):212105, 2008.

- [151] S. B. Lee, S. C. Chae, S. H. Chang, and T. W. Noh. Predictability of Reset Switching Voltages in Unipolar Resistance Switching. *Applied Physics Letters*, 94(17):173504, 2009.
- [152] S. R. Lee, Y.-B. Kim, M. Chang, K. M. Kim, C. B. Lee, J. H. Hur, G.-S. Park, D. Lee, M.-J. Lee, C.-J. Kim, U.-I. Chung, I.-K. Yoo, and K. Kim. Multi-level Switching of Triple-layered TaO_x RRAM with Excellent Reliability for Storage Class Memory. In *Proceedings of the Symposium on VLSI Technology (VLSIT)*, pages 71–72, 2012.
- [153] K. Likharev, N. S. Bakhvalov, G. S. Kazacha, and S. I. Serdyukova. Single-Electron Tunnel Junction Array: an Electrostatic Analog of the Josephson Transmission Line. *IEEE Transactions on Magnetics*, 25(2):1436–1439, 1989.
- [154] C.-C. Lin, C.-Y. Lin, M.-H. Lin, C.-H. Lin, and T.-Y. Tseng. Voltage-Polarity-Independent and High-Speed Resistive Switching Properties of V-Doped SrZrO₃ Thin Films. *IEEE Transactions on Electron Devices*, 54(12):3146–3151, 2007.
- [155] C.-Y. Lin, C.-Y. Wu, C.-Y. Wu, C. Hu, and T.-Y. Tseng. Bistable Resistive Switching in Al₂O₃ Memory Thin Films. *Journal of the Electrochemical Society*, 154(9):G189–G192, 2007.
- [156] C.-Y. Lin, C.-Y. Wu, C.-Y. Wu, T.-C. Lee, F.-L. Yang, C. Hu, and T.-Y. Tseng. Effect of Top Electrode Material on Resistive Switching Properties of Film Memory Devices. *IEEE Electron Device Letters*, 28(5):366–368, 2007.
- [157] K.-L. Lin, T.-H. Hou, J. Shieh, J.-H. Lin, C.-T. Chou, and Y.-J. Lee. Electrode Dependence of Filament Formation in HfO₂ Resistive-Switching Memory. *Journal of Applied Physics*, 109(8):084104, 2011.
- [158] H. Liu, D. Bedau, D. Backes, J. A. Katine, and A. D. Kent. Precessional Reversal in Orthogonal Spin Transfer Magnetic Random Access Memory Devices. *Applied Physics Letters*, 101(3):032403, 2012.
- [159] H. Liu, D. Bedau, D. Backes, J. A. Katine, J. Langer, and A. D. Kent. Ultrafast Switching in Magnetic Tunnel Junction Based Orthogonal Spin Transfer Devices. *Applied Physics Letters*, 97(24):242510, 2010.
- [160] T.-Y. Liu, T. Yan, R. Scheuerlein, Y. Chen, J. Lee, G. Balakrishnan, G. Yee, H. Zhang, A. Yap, J. Ouyang, T. Sasaki, S. Addepalli, A. Al-Shamma, C.-Y. Chen, M. Gupta, G. Hilton, S. Joshi, A. Kathuria, V. Lai, D. Masiwal, M. Matsumoto, A. Nigam, A. Pai, J. Pakhale, C. Siau, X. Wu, R. Yin, L. Peng, J. Kang, S. Huynh, H. Wang, N. Nagel, Y. Tanaka, M. Higashitani, T. Minvielle, C. Gorla, T. Tsukamoto, T. Yamaguchi, M. Okajima, T. Okamura, S. Takase, T. Hara, H. Inoue, L. Fasoli, M. Mofidi, R. Shrivastava, and K. Quader. A 130.7mm² 2-layer 32Gb ReRAM Memory Device in 24nm Technology. In *Proceedings of the IEEE International Solid-State Circuits Conference (ISSCC)*, pages 210–211, 2013.

- [161] X. Liu, K. P. Biju, J. Lee, J. Park, S. Kim, S. Park, J. Shin, S. M. Sadaf, and H. Hwang. Parallel Memristive Filaments Model Applicable to Bipolar and Filamentary Resistive Switching. *Applied Physics Letters*, 99(11):113518, 2011.
- [162] Y. Lu, B. Gao, Y. Fu, B. Chen, L. Liu, X. Liu, and J. Kang. A Simplified Model for Resistive Switching of Oxide-Based Resistive Random Access Memory Devices. *IEEE Electron Device Letters*, 33(3):306–308, 2012.
- [163] K. Machida, N. Funabashi, K. ichi Aoshima, Y. Miyamoto, N. Kawamura, K. Kuga, and N. Shimidzu. Spin Transfer Switching of Closely Arranged Multiple Pillars with Current-Perpendicular-to-Plane Spin Valves. *Journal of Applied Physics*, 103(7):07A713, 2008.
- [164] J. Mathon and A. Umerski. Theory of Tunneling Magnetoresistance of an Epitaxial Fe/MgO/Fe(001) Junction. *Physical Review B*, 63:220403, 2001.
- [165] J. E. Miltat and M. J. Donahue. *Handbook of Magnetism and Advanced Magnetic Materials*, volume Micromagnetism, chapter Numerical Micromagnetics: Finite Difference Methods. John Wiley & Sons, Ltd., 2007.
- [166] T. Miyazaki and N. Tezuka. Giant Magnetic Tunneling Effect in Fe/Al₂O₃/Fe Junction. *Journal of Magnetism and Magnetic Materials*, 139(3):L231–L234, 1995.
- [167] N. Mojumder, C. Augustine, and K. Roy. Self-Consistent Transport-Magnetic Simulation and Benchmarking of Hybrid Spin-Torque Driven Magnetic Tunnel Junctions (MTJs). In *18th Biennial University/Government/Industry Micro/-Nano Symposium (UGIM)*, pages 1–6, 2010.
- [168] N. N. Mojumder, C. Augustine, D. E. Nikonov, and K. Roy. Effect of Quantum Confinement on Spin Transport and Magnetization Dynamics in Dual Barrier Spin Transfer Torque Magnetic Tunnel Junctions. *Journal of Applied Physics*, 108(10):104306, 2010.
- [169] J. S. Moodera, L. R. Kinder, T. M. Wong, and R. Meservey. Large Magnetoresistance at Room Temperature in Ferromagnetic Thin Film Tunnel Junctions. *Physical Review Letters*, 74:3273–3276, 1995.
- [170] R. Münstermann, T. Menke, R. Dittmann, and R. Waser. Coexistence of Filamentary and Homogeneous Resistive Switching in Fe-Doped SrTiO₃ Thin-Film Memristive Devices. *Advanced Materials*, 22(43):4819–4822, 2010.
- [171] E. B. Myers, D. C. Ralph, J. A. Katine, R. N. Louie, and R. A. Buhrman. Current-Induced Switching of Domains in Magnetic Multilayer Devices. *Science*, 285(5429):867–870, 1999.
- [172] K. Nagashima, T. Yanagida, K. Oka, and T. Kawai. Unipolar Resistive Switching Characteristics of Room Temperature Grown SnO₂ Thin Films. *Applied Physics Letters*, 94(24):242902, 2009.

- [173] Y. B. Nian, J. Strozier, N. J. Wu, X. Chen, and A. Ignatiev. Evidence for an Oxygen Diffusion Model for the Electric Pulse Induced Resistance Change Effect in Transition-Metal Oxides. *Physical Review Letters*, 98:146403, 2007.
- [174] Y. Nishi and J. Jameson. Recent Progress in Resistance Change Memory. In *Proceedings of the Device Research Conference*, pages 271–274, 2008.
- [175] S. Okhonin, M. Nagoga, E. Carman, R. Beffa, and E. Faraoni. New Generation of Z-RAM. In *Proceedings of the IEEE International Electron Devices Meeting (IEDM)*, pages 925–928, 2007.
- [176] S. Okhonin, M. Nagoga, J. M. Sallese, and P. Fazan. A SOI Capacitor-Less 1T-DRAM Concept. In *Proceedings of the IEEE International SOI Conference*, pages 153–154, 2001.
- [177] S. R. Ovshinsky. Reversible Electrical Switching Phenomena in Disordered Structures. *Physical Review Letters*, 21:1450–1453, 1968.
- [178] D. Oxley. Electroforming, Switching and Memory Effects in Oxide Thin Films. *ElectroComponent Science and Technology*, 3(4):217–224, 1977.
- [179] S. S. P. Parkin, C. Kaiser, A. Panchula, P. M. Rice, B. Hughes, M. Samant, and S.-H. Yang. Giant Tunnelling Magnetoresistance at Room Temperature with MgO (100) Tunnel Barriers. *Nature Materials*, 3(12):862–867, 2004.
- [180] I. Prejbeanu, M. Kerekes, R. Sousa, H. Sibuet, O. Redon, B. Dieny, and J. Nozières. Thermally Assisted MRAM. *Journal of Physics: Condensed Matter*, 19(16):165218, 2007.
- [181] G. Prinz. Spin-Polarized Transport. *Physics Today*, 48(4):58–63, 1995.
- [182] N. Raghavan, R. Degraeve, A. Fantini, L. Goux, D. Wouters, G. Groeseneken, and M. Jurczak. Stochastic Variability of Vacancy Filament Configuration in Ultra-Thin Dielectric RRAM and its Impact on OFF-State Reliability. In *Proceedings of the IEEE International Electron Devices Meeting (IEDM)*, pages 21.1.1–21.1.4, 2013.
- [183] N. Rodriguez, S. Cristoloveanu, and F. Gamiz. A-RAM: Novel Capacitor-Less DRAM Memory. In *Proceedings of the IEEE International SOI Conference*, pages 1–2, 2009.
- [184] N. Rodriguez, S. Cristoloveanu, and F. Gamiz. Capacitor-Less A-RAM SOI Memory: Principles, Scaling and Expected Performance. *Solid-State Electronics*, 59(1):44–49, 2011.
- [185] N. Rodriguez, S. Cristoloveanu, and F. Gamiz. Novel Capacitorless 1T-DRAM Cell for 22-nm Node Compatible With Bulk and SOI Substrates. *IEEE Transactions on Electron Devices*, 58(8):2371–2377, 2011.

- [186] N. Rodriguez, F. Gamiz, and S. Cristoloveanu. A-RAM Memory Cell: Concept and Operation. *IEEE Electron Device Letters*, 31(9):972–974, 2010.
- [187] N. Rodriguez, F. Gamiz, C. Marquez, C. Navarro, F. Andrieu, O. Faynot, and S. Cristoloveanu. Fabrication and Validation of A2RAM Memory Cells on SOI and Bulk Substrates. In *Proceedings of the IEEE International Memory Workshop (IMW)*, pages 135–138, 2013.
- [188] N. Rodriguez, C. Navarro, F. Gamiz, F. Andrieu, O. Faynot, and S. Cristoloveanu. Experimental Demonstration of A2RAM Memory Cell on SOI. In *Proceedings of the IEEE International SOI Conference*, pages 1–2, 2012.
- [189] N. Rodriguez, C. Navarro, F. Gamiz, F. Andrieu, O. Faynot, and S. Cristoloveanu. Experimental Demonstration of Capacitorless A2RAM Cells on Silicon-on-Insulator. *IEEE Electron Device Letters*, 33(12):1717–1719, 2012.
- [190] C. Rohde, B. J. Choi, D. S. Jeong, S. Choi, J.-S. Zhao, and C. S. Hwang. Identification of a Determining Parameter for Resistive Switching of TiO₂ Thin Films. *Applied Physics Letters*, 86(26):262907, 2005.
- [191] C. Rossel, G. I. Meijer, D. Brémaud, and D. Widmer. Electrical Current Distribution Across a Metal–Insulator–Metal Structure During Bistable Switching. *Journal of Applied Physics*, 90(6):2892–2898, 2001.
- [192] M. J. Rozenberg, I. H. Inoue, and M. J. Sánchez. Nonvolatile Memory with Multilevel Switching: A Basic Model. *Physical Review Letters*, 92:178302, 2004.
- [193] M. J. Rozenberg, M. J. Sánchez, R. Weht, C. Acha, F. Gomez-Marlasca, and P. Levy. Mechanism for Bipolar Resistive Switching in Transition-Metal Oxides. *Physical Review B*, 81:115101, 2010.
- [194] U. Russo, D. Ielmini, C. Cagli, and A. Lacaíta. Filament Conduction and Reset Mechanism in NiO-Based Resistive-Switching Memory (RRAM) Devices. *IEEE Transactions on Electron Devices*, 56(2):186–192, 2009.
- [195] U. Russo, D. Ielmini, C. Cagli, and A. Lacaíta. Self-Accelerated Thermal Dissolution Model for Reset Programming in Unipolar Resistive-Switching Memory (RRAM) Devices. *IEEE Transactions on Electron Devices*, 56(2):193–200, 2009.
- [196] U. Russo, D. Ielmini, C. Cagli, A. Lacaíta, S. Spiga, C. Wiemer, M. Perego, and M. Fanciulli. Conductive-Filament Switching Analysis and Self-Accelerated Thermal Dissolution Model for Reset in NiO-based RRAM. In *Proceedings of the IEEE International Electron Devices Meeting (IEDM)*, pages 775–778, 2007.
- [197] M. Sasaki. An Electron Conduction Model of Resistive Memory for Resistance Dispersion, Fluctuation, Filament Structures, and Set/Reset Mechanism. *Journal of Applied Physics*, 112(1):014501, 2012.

- [198] H. Sato, M. Yamanouchi, S. Ikeda, S. Fukami, F. Matsukura, and H. Ohno. Perpendicular-Anisotropy CoFeB-MgO Magnetic Tunnel Junctions with a MgO/CoFeB/Ta/CoFeB/MgO Recording Structure. *Applied Physics Letters*, 101(2):022414, 2012.
- [199] H. Sato, M. Yamanouchi, K. Miura, S. Ikeda, H. D. Gan, K. Mizunuma, R. Koizumi, F. Matsukura, and H. Ohno. Junction Size Effect on Switching Current and Thermal Stability in CoFeB/MgO Perpendicular Magnetic Tunnel Junctions. *Applied Physics Letters*, 99(4):042501, 2011.
- [200] Y. Sato, K. Kinoshita, M. Aoki, and Y. Sugiyama. Consideration of Switching Mechanism of Binary Metal Oxide Resistive Junctions Using a Thermal Reaction Model. *Applied Physics Letters*, 90(3):033503, 2007.
- [201] A. Sawa. Resistive Switching in Transition Metal Oxides. *Materials Today*, 11(6):28–36, 2008.
- [202] A. Sawa, T. Fujii, M. Kawasaki, and Y. Tokura. Hysteretic Current–Voltage Characteristics and Resistance Switching at a Rectifying Ti/Pr_{0.7}Ca_{0.3}MnO₃ Interface. *Applied Physics Letters*, 85(18):4073–4075, 2004.
- [203] R. Sbiaa, S. Y. H. Lua, R. Law, H. Meng, R. Lye, and H. K. Tan. Reduction of Switching Current by Spin Transfer Torque Effect in Perpendicular Anisotropy Magnetoresistive Devices (Invited). *Journal of Applied Physics*, 109(7):07C707, 2011.
- [204] R. Sbiaa, H. Meng, and S. N. Piramanayagam. Materials with Perpendicular Magnetic Anisotropy for Magnetic Random Access Memory. *physica status solidi (RRL) – Rapid Research Letters*, 5(12):413–419, 2011.
- [205] S. Seo, M. J. Lee, D. C. Kim, S. E. Ahn, B.-H. Park, Y. S. Kim, I. K. Yoo, I. S. Byun, I. R. Hwang, S. H. Kim, J.-S. Kim, J. S. Choi, J. H. Lee, S. H. Jeon, S. H. Hong, and B. H. Park. Electrode Dependence of Resistance Switching in Polycrystalline NiO Films. *Applied Physics Letters*, 87(26):263507, 2005.
- [206] S. Seo, M. J. Lee, D. H. Seo, S. K. Choi, D.-S. Suh, Y. S. Joung, I. K. Yoo, I. S. Byun, I. R. Hwang, S. H. Kim, and B. H. Park. Conductivity Switching Characteristics and Reset Currents in NiO Films. *Applied Physics Letters*, 86(9):093509, 2005.
- [207] S. Seo, M. J. Lee, D. H. Seo, E. J. Jeoung, D.-S. Suh, Y. S. Joung, I. K. Yoo, I. R. Hwang, S. H. Kim, I. S. Byun, J.-S. Kim, J. S. Choi, and B. H. Park. Reproducible Resistance Switching in Polycrystalline NiO Films. *Applied Physics Letters*, 85(23):5655–5657, 2004.
- [208] H. Shima, F. Takano, H. Akinaga, Y. Tamai, I. H. Inoue, and H. Takagi. Resistance Switching in the Metal Deficient-Type Oxides: NiO and CoO. *Applied Physics Letters*, 91(1):012901, 2007.

- [209] H. Shima, N. Zhong, and H. Akinaga. Switchable Rectifier Built with Pt/TiO_x/Pt Trilayer. *Applied Physics Letters*, 94(8):082905, 2009.
- [210] T. Shino, N. Kusunoki, T. Higashi, T. Ohsawa, K. Fujita, K. Hatsuda, N. Ikumi, F. Matsuoka, Y. Kajitani, R. Fukuda, Y. Watanabe, Y. Minami, A. Sakamoto, J. Nishimura, H. Nakajima, M. Morikado, K. Inoh, T. Hamamoto, and A. Nitayama. Floating Body RAM Technology and its Scalability to 32 nm Node and Beyond. In *Proceedings of the IEEE International Electron Devices Meeting (IEDM)*, pages 1–4, 2006.
- [211] K. Shiraishi, M. Yang, S. Kato, M. Araidai, K. Kamiya, T. Yamamoto, T. Ohyanagi, N. Takaura, M. Niwa, B. Magyari-Köpe, and Y. Nishi. Physics in Charge Injection Induced On-Off Switching Mechanism of Oxide-Based Resistive Random Access Memory (ReRAM) and Superlattice GeTe/Sb₂Te₃ Phase Change Memory (PCM). In *Extended Abstracts of the 2013 International Conference on Solid State Devices and Materials (SSDM)*, pages 574–575, 2013.
- [212] C. H. Sim, M. Moneck, T. Liew, and J.-G. Zhu. Frequency-Tunable Perpendicular Spin Torque Oscillator. *Journal of Applied Physics*, 111(7):07C914, 2012.
- [213] H. Sim, D. Choi, D. Lee, M. Hasan, C. B. Samantaray, and H. Hwang. Reproducible Resistance Switching Characteristics of Pulsed Laserdeposited Polycrystalline Nb₂O₅. *Microelectronic Engineering*, 80(0):260–263, 2005.
- [214] H. Sim, D. Choi, D. Lee, S. Seo, M.-J. Lee, I.-K. Yoo, and H. Hwang. Resistance-Switching Characteristics of Polycrystalline Nb₂O₅ for Nonvolatile Memory Application. *IEEE Electron Device Letters*, 26(5):292–294, 2005.
- [215] H. Sim, H. Choi, D. Lee, M. Chang, D. Choi, Y. Son, E.-H. Lee, W. Kim, Y. Park, I.-K. Yoo, and H. Hwang. Excellent Resistance Switching Characteristics of Pt/SrTiO₃ Schottky Junction for Multi-bit Nonvolatile Memory Application. In *Proceedings of the IEEE International Electron Devices Meeting (IEDM)*, pages 758–761, 2005.
- [216] J. G. Simmons and R. R. Verderber. New Conduction and Reversible Memory Phenomena in Thin Insulating Films. *Proceedings of the Royal Society of London. Series A, Mathematical and Physical Sciences*, 301(1464):pp. 77–102, 1967.
- [217] J. Slonczewski. Current-Driven Excitation of Magnetic Multilayers. *Journal of Magnetism and Magnetic Materials*, 159(1–2):L1–L7, 1996.
- [218] J. C. Slonczewski. Currents, Torques, and Polarization Factors in Magnetic Tunnel Junctions. *Physical Review B*, 71:024411, 2005.
- [219] J. Sun. Current-Driven Magnetic Switching in Manganite Trilayer Junctions. *Journal of Magnetism and Magnetic Materials*, 202(1):157–162, 1999.

- [220] J. Z. Sun, M. C. Gaidis, E. J. O'Sullivan, E. A. Joseph, G. Hu, D. W. Abraham, J. J. Nowak, P. L. Trouilloud, Y. Lu, S. L. Brown, D. C. Worledge, and W. J. Gallagher. A Three-Terminal Spin-Torque-Driven Magnetic Switch. *Applied Physics Letters*, 95(8):083506, 2009.
- [221] R. R. Sutherland. A Theory for Negative Resistance and Memory Effects in Thin Insulating Films and its Application to Au-ZnS-Au Devices. *Journal of Physics D: Applied Physics*, 4(3):468, 1971.
- [222] R. Suzuki. Recent Development in Magnetic-Bubble Memory. *Proceedings of the IEEE*, 74(11):1582–1590, 1986.
- [223] V. Sverdlov and S. Selberherr. Modeling Floating Body Z-RAM Storage Cells. In *Proceedings of the International Conference on Microelectronics (MIEL)*, pages 45–50, 2010.
- [224] V. A. Sverdlov, A. N. Korotkov, and K. K. Likharev. Shot-Noise Suppression at Two-Dimensional Hopping. *Physical Review B*, 63:081302, 2001.
- [225] Y.-E. Syu, T.-C. Chang, T.-M. Tsai, G.-W. Chang, K.-C. Chang, Y.-H. Tai, M.-J. Tsai, Y.-L. Wang, and S. M. Sze. Silicon Introduced Effect on Resistive Switching Characteristics of WO_x Thin Films. *Applied Physics Letters*, 100(2):022904, 2012.
- [226] K. Szot, W. Speier, G. Bihlmayer, and R. Waser. Switching the Electrical Resistance of Individual Dislocations in Single-Crystalline SrTiO_3 . *Nature Materials*, 5(4):312–320, 2006.
- [227] S. Tehrani, J. M. Slaughter, M. DeHerrera, B. Engel, N. Rizzo, J. Salter, M. Durlam, R. Dave, J. Janesky, B. Butcher, K. Smith, and G. Grynkewich. Magnetoresistive Random Access Memory Using Magnetic Tunnel Junctions. *Proceedings of the IEEE*, 91(5):703–714, 2003.
- [228] D. Tomáš. *Modelling of Micromagnetic Structures*. PhD thesis, Paris-Sud University, Orsay and Charles University, Prague, 1999.
- [229] L. Torres, L. Lopez-Diaz, E. Martinez, M. Carpentieri, and G. Finocchio. Micromagnetic Computations of Spin Polarized Current-Driven Magnetization Processes. *Journal of Magnetism and Magnetic Materials*, 286(0):381–385, 2005.
- [230] M. Tsoi, A. G. M. Jansen, J. Bass, W.-C. Chiang, M. Seck, V. Tsoi, and P. Wyder. Excitation of a Magnetic Multilayer by an Electric Current. *Physical Review Letters*, 80:4281–4284, 1998.
- [231] S. Tsui, A. Baikalov, J. Cmaidalka, Y. Y. Sun, Y. Q. Wang, Y. Y. Xue, C. W. Chu, L. Chen, and A. J. Jacobson. Field-Induced Resistive Switching in Metal-Oxide Interfaces. *Applied Physics Letters*, 85(2):317–319, 2004.

- [232] L. Vandelli, A. Padovani, L. Larcher, G. Bersuker, D. Gilmer, and P. Pavan. Modeling of the Forming Operation in HfO₂-Based Resistive Switching Memories. In *Proceedings of the IEEE International Memory Workshop (IMW)*, pages 1–4, 2011.
- [233] L. Vandelli, A. Padovani, L. Larcher, G. Bersuker, J. Yum, and P. Pavan. A Physics-Based Model of the Dielectric Breakdown in HfO₂ for Statistical Reliability Prediction. In *Proceedings of the IEEE International Reliability Physics Symposium (IRPS)*, pages GD.5.1–GD.5.4, 2011.
- [234] L. Vandelli, A. Padovani, L. Larcher, G. Broglia, G. Ori, M. Montorsi, G. Bersuker, and P. Pavan. Comprehensive Physical Modeling of Forming and Switching Operations in HfO₂ RRAM Devices. In *Proceedings of the IEEE International Electron Devices Meeting (IEDM)*, pages 17.5.1–17.5.4, 2011.
- [235] J. Wan, C. Le Royer, A. Zaslavsky, and S. Cristoloveanu. A Compact Capacitor-Less High-Speed DRAM Using Field Effect-Controlled Charge Regeneration. *IEEE Electron Device Letters*, 33(2):179–181, 2012.
- [236] J. Wan, C. Le Royer, A. Zaslavsky, and S. Cristoloveanu. Z²-FET: A Zero-Slope Switching Device with Gate-Controlled Hysteresis. In *Proceedings of the International Symposium on VLSI Technology, Systems, and Applications (VLSI-TSA)*, pages 1–4, 2012.
- [237] J. Wan, C. Le Royer, A. Zaslavsky, and S. Cristoloveanu. Z²-FET Used as 1-Transistor High-Speed DRAM. In *Proceedings of the European Solid-State Device Research Conference (ESSDERC)*, pages 197–200, 2012.
- [238] J. Wan, C. Le Royer, A. Zaslavsky, and S. Cristoloveanu. A Systematic Study of the Sharp-Switching Z²-FET Device: From Mechanism to Modeling and Compact Memory Applications. *Solid-State Electronics*, 90(0):2–11, 2013.
- [239] J. Wan, C. Le Royer, A. Zaslavsky, and S. Cristoloveanu. Progress in Z²-FET 1T-DRAM: Retention Time, Writing Modes, Selective Array Operation, and Dual Bit Storage. *Solid-State Electronics*, 84(0):147–154, 2013.
- [240] D. Wang, C. Nordman, J. Daughton, Z. Qian, and J. Fink. 70% TMR at Room Temperature for SDT Sandwich Junctions with CoFeB as Free and Reference Layers. *IEEE Transactions on Magnetics*, 40(4):2269–2271, 2004.
- [241] R. Waser. Electrochemical and Thermochemical Memories. In *Proceedings of the IEEE International Electron Devices Meeting (IEDM)*, pages 1–4, 2008.
- [242] R. Waser, R. Dittmann, G. Staikov, and K. Szot. Redox-Based Resistive Switching Memories – Nanoionic Mechanisms, Prospects, and Challenges. *Advanced Materials*, 21(25-26):2632–2663, 2009.

- [243] Y. Watanabe, J. G. Bednorz, A. Bietsch, C. Gerber, D. Widmer, A. Beck, and S. J. Wind. Current-Driven Insulator-Conductor Transition and Nonvolatile Memory in Chromium-Doped SrTiO₃ Single Crystals. *Applied Physics Letters*, 78(23):3738–3740, 2001.
- [244] H.-S. P. Wong, H.-Y. Lee, S. Yu, Y.-S. Chen, Y. Wu, P.-S. Chen, B. Lee, F. T. Chen, and M.-J. Tsai. Metal-Oxide RRAM. *Proceedings of the IEEE*, 100(6):1951–1970, 2012.
- [245] H. S. P. Wong, S. Raoux, S. Kim, J. Liang, J. P. Reifenberg, B. Rajendran, M. Asheghi, and K. E. Goodson. Phase Change Memory. *Proceedings of the IEEE*, 98(12):2201–2227, 2010.
- [246] J. Woo, W. Lee, S. Park, S. Kim, D. Lee, G. Choi, E. Cha, J. H. Lee, W. Y. Jung, C. G. Park, and H. Hwang. Multi-layer Tunnel Barrier (Ta₂O₅/TaO_x/TiO₂) Engineering for Bipolar RRAM Selector Applications. In *Proceedings of the Symposium on VLSI Technology (VLSIT)*, pages T168–T169, 2013.
- [247] J. Xiao, A. Zangwill, and M. D. Stiles. Macrospin Models of Spin Transfer Dynamics. *Physical Review B*, 72:014446, 2005.
- [248] Z. H. Xiao, X. Q. Ma, P. P. Wu, J. X. Zhang, L. Q. Chen, and S. Q. Shi. Micromagnetic Simulations of Current-Induced Magnetization Switching in Co/Cu/Co Nanopillars. *Journal of Applied Physics*, 102(9):093907, 2007.
- [249] N. Xu, B. Gao, L. Liu, B. Sun, X. Liu, R. Han, J. Kang, and B. Yu. A Unified Physical Model of Switching Behavior in Oxide-Based RRAM. In *Proceedings of the Symposium on VLSI Technology (VLSIT)*, pages 100–101, 2008.
- [250] N. Xu, L. F. Liu, X. Sun, C. Chen, Y. Wang, D. D. Han, X. Y. Liu, R. Q. Han, J. F. Kang, and B. Yu. Bipolar Switching Behavior in TiN/ZnO/Pt Resistive Nonvolatile Memory with Fast Switching and Long Retention. *Semiconductor Science and Technology*, 23(7):075019, 2008.
- [251] K.-H. Xue, C. A. P. de Araujo, J. Celinska, and C. McWilliams. A Non-Filamentary Model for Unipolar Switching Transition Metal Oxide Resistance Random Access Memories. *Journal of Applied Physics*, 109(9):091602, 2011.
- [252] I. K. Yoo, B. S. Kang, S. E. Ahn, C. B. Lee, M.-J. Lee, G.-S. Park, and X.-S. Li. Fractal Dimension of Conducting Paths in Nickel Oxide (NiO) Thin Films During Resistance Switching. *IEEE Transactions on Nanotechnology*, 9(2):131–133, 2010.
- [253] C. Yoshida, Y. M. Lee, T. Ochiai, Y. Uehara, and T. Sugii. Micromagnetic Study of Current-Pulse-Induced Magnetization Switching in Magnetic Tunnel Junctions with Antiferromagnetically and Ferromagnetically Coupled Synthetic Free Layers. *Applied Physics Letters*, 99(22):222505, 2011.

- [254] C. Yoshida, K. Tsunoda, H. Noshiro, and Y. Sugiyama. High Speed Resistive Switching in Pt/TiO₂/TiN Film for Nonvolatile Memory Application. *Applied Physics Letters*, 91(22):223510, 2007.
- [255] E. Yoshida and T. Tanaka. A Capacitor-Less 1T-DRAM Technology Using Gate-Induced Drain-Leakage (GIDL) Current for Low-Power High-Speed Embedded Memory. *IEEE Transactions on Electron Devices*, 53(4):692–697, 2006.
- [256] S. Yu, Y. Y. Chen, X. Guan, H.-S. P. Wong, and J. A. Kittl. A Monte Carlo Study of the Low Resistance State Retention of HfO_x Based Resistive Switching Memory. *Applied Physics Letters*, 100(4):043507, 2012.
- [257] S. Yu, X. Guan, and H.-S. Wong. On the Stochastic Nature of Resistive Switching in Metal Oxide RRAM: Physical Modeling, Monte Carlo Simulation, and Experimental Characterization. In *Proceedings of the IEEE International Electron Devices Meeting (IEDM)*, pages 17.3.1–17.3.4, 2011.
- [258] S. Yu, X. Guan, and H.-S. P. Wong. Conduction Mechanism of TiN/HfO_x/Pt Resistive Switching Memory: A Trap-Assisted-Tunneling Model. *Applied Physics Letters*, 99(6):063507, 2011.
- [259] S. Yu and H.-S. Wong. A Phenomenological Model for the Reset Mechanism of Metal Oxide RRAM. *IEEE Electron Device Letters*, 31(12):1455–1457, 2010.
- [260] S. Yuasa, A. Fukushima, H. Kubota, Y. Suzuki, and K. Ando. Giant Tunneling Magnetoresistance Up to 410% at Room Temperature in Fully Epitaxial Co/MgO/Co Magnetic Tunnel Junctions with BCC Co(001) Electrodes. *Applied Physics Letters*, 89(4):042505, 2006.
- [261] S. Yuasa, T. Nagahama, A. Fukushima, Y. Suzuki, and K. Ando. Giant Room-Temperature Magnetoresistance in Single-Crystal Fe/MgO/Fe Magnetic Tunnel Junctions. *Nature Materials*, 3(12):868–871, 2004.
- [262] P. Zahn and I. Mertig. *Handbook of Magnetism and Advanced Magnetic Materials*, volume Fundamentals and Theory, chapter Enhanced Magnetoresistance. John Wiley & Sons, Ltd., 2007.
- [263] Z. Zeng, G. Finocchio, B. Zhang, P. Amiri, J. Katine, I. Krivorotov, Y. Huai, J. Langer, B. Azzerboni, K. Wang, and H. Jiang. Ultralow-Current-Density and Bias-Field-Free Spin-Transfer Nano-Oscillator. *Scientific Reports*, 3:1426, 2013.
- [264] Z. M. Zeng, P. Upadhyaya, P. Khalili Amiri, K. H. Cheung, J. A. Katine, J. Langer, K. L. Wang, and H. W. Jiang. Enhancement of Microwave Emission in Magnetic Tunnel Junction Oscillators Through In-Plane Field Orientation. *Applied Physics Letters*, 99(3):032503, 2011.
- [265] S. Zhang, P. M. Levy, and A. Fert. Mechanisms of Spin-Polarized Current-Driven Magnetization Switching. *Physical Review Letters*, 88:236601, 2002.

- [266] L. Zhao, J. Zhang, Y. He, X. Guan, H. Qian, and Z. Yu. Dynamic Modeling and Atomistic Simulations of SET and RESET Operations in TiO₂-Based Unipolar Resistive Memory. *IEEE Electron Device Letters*, 32(5):677–679, 2011.
- [267] Y. Zhou. *Spin Momentum Transfer Effects for Spintronic Device Applications*. PhD thesis, Stockholm-Kista, Sweden, 2009.

List of Publications

- [1] T. Windbacher, A. Makarov, H. Mahmoudi, V. Sverdlov, and S. Selberherr. Novel Bias-Field-Free Spin Transfer Oscillator. *Journal of Applied Physics*, 115(17):17C901–1–17C901–3, 2014.
- [2] A. Makarov, V. Sverdlov, D. Osintsev, and S. Selberherr. Simulation of Magnetic Oscillations in a System of Two MTJs with a Shared Free Layer. In *Abstracts Book of The 21st International Conference on Soft Magnetic Materials (SMM)*, page 101, Budapest, Hungary, 2013.
- [3] A. Makarov, V. Sverdlov, and S. Selberherr. Bias-Field-Free Spin-Torque Oscillator Based on Two MgO-MTJs with a Shared Free Layer: Micromagnetic Modeling. In *Abstracts International Symposium on Advanced Nanodevices and Nanotechnology (ISANN)*, Kauai, Hawaii, USA, 2013.
- [4] A. Makarov, V. Sverdlov, and S. Selberherr. Composite Magnetic Tunnel Junctions for Fast Memory Devices and Efficient Spin-Torque Nano-Oscillators. In *Abstracts International Conference on Information Engineering (ICIE)*, page 7, Hong Kong, 2013.
- [5] A. Makarov, V. Sverdlov, and S. Selberherr. Concept of a Bias-Field-Free Spin-Torque Oscillator Based on Two MgO-MTJs. In *Extended Abstracts of the 2013 International Conference on Solid State Devices and Materials (SSDM)*, pages 796–797, Fukuoka, Japan, 2013.
- [6] A. Makarov, V. Sverdlov, and S. Selberherr. Fast Switching STT-MRAM Cells for Future Universal Memory. In *Abstracts Advanced Workshop on Frontiers in Electronics (WOFE)*, San Juan, Puerto Rico, 2013.
- [7] A. Makarov, V. Sverdlov, and S. Selberherr. Geometry Optimization of Spin-Torque Oscillators Composed of Two MgO-MTJs with a Shared Free Layer. In *Proceedings of the International Conference on Nanoscale Magnetism (ICNM)*, page 69, Istanbul, Turkey, 2013.
- [8] A. Makarov, V. Sverdlov, and S. Selberherr. Magnetic Oscillation of the Transverse Domain Wall in a Penta-Layer MgO-MTJ. In *Proceedings of the 21st International Symposium Nanostructures*, pages 338–339, St. Petersburg, Russian Federation, 2013.

- [9] A. Makarov, V. Sverdlov, and S. Selberherr. Magnetic Tunnel Junctions with a Composite Free Layer: A New Concept for Future Universal Memory. In S. Luryi, J. Xu, and A. Zaslavsky, editors, *Future Trends in Microelectronics - Frontiers and Innovations*, pages 93–101. John Wiley & Sons, 2013.
- [10] A. Makarov, V. Sverdlov, and S. Selberherr. Structural Optimization of MTJs with a Composite Free Layer. In *Proceedings of the 16th International Workshop on Computational Electronics (IWCE)*, pages 74–75, Nara, Japan, 2013.
- [11] A. Makarov, V. Sverdlov, and S. Selberherr. Structural Optimization of MTJs with a Composite Free Layer. In *Abstracts SPIE NanoScience + Engineering Symposium*, page 1, San Diego, CA, USA, 2013.
- [12] A. Makarov, V. Sverdlov, and S. Selberherr. Transverse Domain Wall Formation in a Free Layer: A Mechanism for Switching Failure in a MTJ-Based STT-MRAM. In *Proceedings of the 20th International Symposium on the Physical & Failure Analysis of Integrated Circuits (IPFA)*, pages 267–270, Suzhou, China, 2013.
- [13] D. Osintsev, A. Makarov, V. Sverdlov, and S. Selberherr. Using Strain to Increase the Reliability of Scaled Spin MOSFETs. In *Proceedings of the 20th International Symposium on the Physical & Failure Analysis of Integrated Circuits (IPFA)*, pages 770–773, Suzhou, China, 2013.
- [14] D. Osintsev, V. Sverdlov, A. Makarov, and S. Selberherr. Current and Conductance Modulation at Elevated Temperature in Silicon and InAs-Based Spin Field-Effect Transistors. *Sains Malaysiana*, 42(2):205–211, 2013.
- [15] V. Sverdlov, H. Mahmoudi, A. Makarov, D. Osintsev, J. Weinbub, T. Windbacher, and S. Selberherr. Modeling Spin-Based Devices in Silicon. In *Proceedings of the 16th International Workshop on Computational Electronics (IWCE)*, pages 70–71, Nara, Japan, 2013.
- [16] T. Windbacher, H. Mahmoudi, A. Makarov, V. Sverdlov, and S. Selberherr. Multiple Purpose Spin Transfer Torque Operated Devices. *Facta Universitatis*, 36(3):227–238, 2013.
- [17] T. Windbacher, A. Makarov, H. Mahmoudi, V. Sverdlov, and S. Selberherr. Novel Bias-Field-Free Large Gain Spin-Transfer Oscillator. In *Abstract Book of 58th Annual Conference of Magnetism and Magnetic Materials (MMM)*, pages 456–457, Denver, CO, USA, 2013.
- [18] T. Windbacher, O. Triebel, D. Osintsev, A. Makarov, V. Sverdlov, and S. Selberherr. Simulation Study of an Electrically Read- and Writable Magnetic Logic Gate. *Microelectronic Engineering*, 112:188–192, 2013.

- [19] T. Windbacher, O. Triebel, D. Osintsev, A. Makarov, V. Sverdlov, and S. Selberherr. Switching Optimization of an Electrically Read- and Writable Magnetic Logic Gate. In *Proceedings of the 16th International Workshop on Computational Electronics (IWCE)*, pages 238–239, Nara, Japan, 2013.
- [20] A. Makarov, S. Selberherr, and V. Sverdlov. Emerging Non-Volatile Memories for Ultra-Low Power Applications. In *Tagungsband zur Informationstagung Mikroelektronik 12*, pages 21–24, Vienna, Austria, 2012.
- [21] A. Makarov, V. Sverdlov, D. Osintsev, and S. Selberherr. Fast Switching in Magnetic Tunnel Junctions with Two Pinned Layers: Micromagnetic Modeling. *IEEE Transactions on Magnetics*, 48(4):1289–1292, 2012.
- [22] A. Makarov, V. Sverdlov, and S. Selberherr. Emerging Memory Technologies: Trends, Challenges, and Modeling Methods. *Microelectronics Reliability*, 52(4):628–634, 2012.
- [23] A. Makarov, V. Sverdlov, and S. Selberherr. Geometry Dependence of the Switching Time in MTJs with a Composite Free Layer. In *Abstracts Workshop on Innovative Devices and Systems (WINDS)*, page 21, Kohala Coast, Hawaii, USA, 2012.
- [24] A. Makarov, V. Sverdlov, and S. Selberherr. High Thermal Stability and Low Switching Energy Barrier in Spin-Transfer Torque RAM with Composite Free Layer. In *Extended Abstracts of 2012 International Conference on Solid State Devices and Materials (SSDM)*, Kyoto, Japan, 2012.
- [25] A. Makarov, V. Sverdlov, and S. Selberherr. Micromagnetic Simulations of an MTJ with a Composite Free Layer for High-Speed Spin Transfer Torque RAM. In *Proceedings of the 15th International Workshop on Computational Electronics (IWCE)*, pages 225–226, Madison, WI, USA, 2012.
- [26] A. Makarov, V. Sverdlov, and S. Selberherr. Modeling Emerging Non-Volatile Memories: Current Trends and Challenges. In *Physics Procedia*, pages 99–104, Macao, China, 2012.
- [27] A. Makarov, V. Sverdlov, and S. Selberherr. MTJs with a Composite Free Layer for High-Speed Spin Transfer Torque RAM: Micromagnetic Simulations. In *The 15th International Workshop on Computational Electronics*, pages 1–4. IEEE Xplore, 2012.
- [28] A. Makarov, V. Sverdlov, and S. Selberherr. New Trends in Microelectronics: Towards an Ultimate Memory Concept. In *Proceedings of the 8th International Caribbean Conference on Devices, Circuits and Systems*, Playa del Carmen, Mexico, 2012.
- [29] A. Makarov, V. Sverdlov, and S. Selberherr. New Trends in Microelectronics: Towards an Ultimate Memory Concept. In *The 8th International Caribbean Conference on Devices, Circuits and Systems*, pages 1–4. IEEE Xplore, 2012.

- [30] A. Makarov, V. Sverdlov, and S. Selberherr. Recent Developments in Advanced Memory Modeling. In *Proceedings of the 28th International Conference on Microelectronics*, pages 49–52, Nis, Serbia, 2012.
- [31] A. Makarov, V. Sverdlov, and S. Selberherr. Reduction of the Switching Current in Spin Transfer Torque Random Access Memory. In *Abstracts Advanced Research Workshop on Future Trends in Microelectronics: Into the Cross Currents*, page 49, Corsica, France, 2012.
- [32] A. Makarov, V. Sverdlov, and S. Selberherr. STT-RAM with a Composite Free Layer: High Thermal Stability, Low Switching Barrier, and Sharp Switching Time Distribution. In *Abstract of Worldwide Universities Network 4th International Conference on Spintronics (WUN-SPIN)*, page H4, Sydney, Australia, 2012.
- [33] A. Makarov, V. Sverdlov, and S. Selberherr. Study of Self-Accelerating Switching in MTJs with Composite Free Layer by Micromagnetic Simulations. In *Proceedings of the 17th International Conference on Simulation of Semiconductor Processes and Devices (SISPAD)*, pages 229–232, Denver, CO, USA, 2012.
- [34] D. Osintsev, A. Makarov, V. Sverdlov, and S. Selberherr. Efficient Simulations of the Transport Properties of Spin Field-Effect Transistors Built on Silicon Fins. In I. Lirkov, S. Margenov, and J. Wasniewski, editors, *Lecture Notes in Computer Science, Vol. 7116*, pages 630–637. Springer, 2012.
- [35] D. Osintsev, V. Sverdlov, A. Makarov, and S. Selberherr. Surface Roughness Induced Spin Scattering and Relaxation in Silicon SOI MOSFETs. In *Abstract of Worldwide Universities Network 4th International Conference on Spintronics (WUN-SPIN)*, page B3, Sydney, Australia, 2012.
- [36] D. Osintsev, V. Sverdlov, Z. Stanojevic, A. Makarov, and S. Selberherr. Temperature Dependence of the Transport Properties of Spin Field-Effect Transistors Built with InAs and Si Channels. *Solid-State Electronics*, 71:25–29, 2012.
- [37] V. Sverdlov, A. Makarov, and S. Selberherr. Fast Switching in MTJs with a Composite Free Layer. In *Abstracts of BIT's 2nd Annual World Congress of Nanoscience and Nanotechnology 2012*, page 291, Qingdao, China, 2012.
- [38] V. Sverdlov, A. Makarov, and S. Selberherr. Switching Energy Barrier and Current Reduction in MTJs with Composite Free Layer. In *Bulletin American Physical Society (APS March Meeting 2012)*, Boston, MA, USA, 2012.
- [39] J. Weinbub, K. Rupp, L. Filipovic, A. Makarov, and S. Selberherr. Towards a Free Open Source Process and Device Simulation Framework. In *Proceedings of the 15th International Workshop on Computational Electronics (IWCE)*, pages 141–142, Madison, WI, USA, 2012.

- [40] J. Weinbub, K. Rupp, L. Filipovic, A. Makarov, and S. Selberherr. Towards a Free Open Source Process and Device Simulation Framework. In *The 15th International Workshop on Computational Electronics*, pages 1–4. IEEE Xplore, 2012.
- [41] T. Windbacher, A. Makarov, V. Sverdlov, and S. Selberherr. Simulations of an Electrical Read-Write Operation of a Magnetic XOR Gate. In *Abstract of Worldwide Universities Network 4th International Conference on Spintronics (WUN-SPIN)*, page J3, Sydney, Australia, 2012.
- [42] T. Windbacher, D. Osintsev, A. Makarov, V. Sverdlov, and S. Selberherr. Fully Electrically Read-Write Magneto Logic Gates. In *Book of Abstracts: The 5th International Conference on Micro-Nanoelectronics, Nanotechnologies & MEMS*, Crete, Greece, 2012.
- [43] A. Makarov, S. Selberherr, and V. Sverdlov. Modeling of Advanced Memories. In *Proceedings of the Conference on Electron Devices and Solid-State Circuits (EDSSC)*, Tianjin, China, 2011.
- [44] A. Makarov, V. Sverdlov, D. Kryzhanovsky, M. Girkin, and S. Selberherr. Modeling of Non-Volatile Memory Cells of RRAM Type on High Performance Computer Systems with the Monte-Carlo Method. In *Book of Abstracts: Parallel Computing Technologies (PaVT)*, Moscow, Russian Federation, 2011.
- [45] A. Makarov, V. Sverdlov, D. Osintsev, and S. Selberherr. About the Switching Process in Magnetic Tunnel Junctions with Two Fixed Layers and One Soft Magnetic Layer. In *Abstracts Book of The 20th International Conference on Soft Magnetic Materials (SMM)*, page 444, Kos, Greece, 2011.
- [46] A. Makarov, V. Sverdlov, D. Osintsev, and S. Selberherr. Fast Switching in Magnetic Tunnel Junctions with Double Barrier Layer. In *Extended Abstracts of 2011 International Conference on Solid State Devices and Materials (SSDM)*, Nagoya, Japan, 2011.
- [47] A. Makarov, V. Sverdlov, D. Osintsev, and S. Selberherr. Micromagnetic Modeling of Penta-Layer Magnetic Tunnel Junctions with a Composite Soft Layer. In *Abstracts of Advanced Workshop on Spin and Charge Properties of Low Dimensional Systems*, Brasov, Romania, 2011.
- [48] A. Makarov, V. Sverdlov, D. Osintsev, and S. Selberherr. Modeling of the Switching Process in Multi-Layered Magnetic Tunnel Junctions. In *Proceedings of International School and Conference on Spintronics and Quantum Information Technology (SPINTECH)*, page 238, Matsue, Japan, 2011.
- [49] A. Makarov, V. Sverdlov, D. Osintsev, and S. Selberherr. Optimization of the Penta-Layer Magnetic Tunnel Junction for Fast STTRAM Switching. In *Abstracts International Symposium on Advanced Nanostructures and Nano-Devices (ISANN)*, Kaanapali, Hawaii, USA, 2011.

- [50] A. Makarov, V. Sverdlov, D. Osintsev, and S. Selberherr. Reduction of Switching Time in Pentalayer Magnetic Tunnel Junctions with a Composite-Free Layer. *Physica Status Solidi - Rapid Research Letters*, 5(12):420–422, 2011.
- [51] A. Makarov, V. Sverdlov, D. Osintsev, and S. Selberherr. Switching Time and Current Reduction Using a Composite Free Layer in Magnetic Tunnel Junctions. In *Proceedings of the International Semiconductor Device Research Symposium (ISDRS)*, Washington DC, USA, 2011.
- [52] A. Makarov, V. Sverdlov, D. Osintsev, J. Weinbub, and S. Selberherr. Modeling of the Advanced Spin Transfer Torque Memory: Macro- and Micromagnetic Simulations. In *Proceedings of the 25th European Simulation and Modelling Conference (ESM)*, pages 177–181, Guimaraes, Portugal, 2011.
- [53] A. Makarov, V. Sverdlov, and S. Selberherr. Modeling of the SET and RESET Process in Bipolar Resistive Oxide-Based Memory Using Monte Carlo Simulations. In I. Dimov, S. Dimova, and N. T. Kolkovska, editors, *Lecture Notes in Computer Science, Vol. 6046*, pages 87–94. Springer, 2011.
- [54] A. Makarov, V. Sverdlov, and S. Selberherr. Stochastic Model of the Resistive Switching Mechanism in Bipolar Resistive Random Access Memory: Monte Carlo Simulations. *Journal of Vacuum Science & Technology B*, 29(1):01AD03–1–01AD03–5, 2011.
- [55] D. Osintsev, A. Makarov, S. Selberherr, and V. Sverdlov. An InAs-Based Spin Field-Effect Transistor: A Path to Room Temperature Operation. In *Abstracts International Symposium on Advanced Nanostructures and Nano-Devices (ISANN)*, Kaanapali, Hawaii, USA, 2011.
- [56] D. Osintsev, A. Makarov, V. Sverdlov, and S. Selberherr. Transport Modeling in Spin Field-Effect Transistors Built on Silicon Fins. In *Abstracts International Conference on Large-Scale Scientific Computations*, page 64, Sozopol, Bulgaria, 2011.
- [57] D. Osintsev, V. Sverdlov, A. Makarov, and S. Selberherr. Ballistic Transport in Spin Field-Effect Transistors Built on Si and InAs. In *Proceedings of International School and Conference on Spintronics and Quantum Information Technology (SPINTECH)*, page 229, Matsue, Japan, 2011.
- [58] D. Osintsev, V. Sverdlov, A. Makarov, and S. Selberherr. Ballistic Transport in Spin Field-Effect Transistors Built on Silicon. In *Abstracts of Advanced Workshop on Spin and Charge Properties of Low Dimensional Systems*, Brasov, Romania, 2011.
- [59] D. Osintsev, V. Sverdlov, A. Makarov, and S. Selberherr. Ballistic Transport Properties of Spin Field-Effect Transistors Built on Silicon and InAs Fins. In *ECS Transactions*, pages 155–162, Joao Pessoa, Brazil, 2011.

- [60] D. Osintsev, V. Sverdlov, A. Makarov, and S. Selberherr. Properties of InAs- and Silicon-Based Ballistic Spin Field-Effect Transistors Operated at Elevated Temperature. In *Proceedings of the International Semiconductor Device Research Symposium (ISDRS)*, Washington DC, USA, 2011.
- [61] D. Osintsev, V. Sverdlov, A. Makarov, and S. Selberherr. Properties of InAs- and Silicon-Based Ballistic Spin Field-Effect Transistors. In *Proceedings of the 16th International Conference on Simulation of Semiconductor Processes and Devices*, pages 59–62, Osaka, Japan, 2011.
- [62] D. Osintsev, V. Sverdlov, Z. Stanojevic, A. Makarov, and S. Selberherr. Ballistic Spin Field-Effect Transistors Built on Silicon Fins. In *Conference Proceedings of the VII Workshop of the Thematic Network on Silicon-On-Insulator Technology, Devices and Circuits*, pages 59–60, Granada, Spain, 2011.
- [63] D. Osintsev, V. Sverdlov, Z. Stanojevic, A. Makarov, and S. Selberherr. Transport Properties of Spin Field-Effect Transistors Built on Si and InAs. In *Proceedings of the 12th International Conference on Ultimate Integration on Silicon (ULIS)*, pages 210–213, Cork, Ireland, 2011.
- [64] D. Osintsev, V. Sverdlov, Z. Stanojevic, A. Makarov, J. Weinbub, and S. Selberherr. Properties of Silicon Ballistic Spin Fin-Based Field-Effect Transistors. In *219th ECS Meeting*, pages 277–282, Montreal, Canada, 2011.
- [65] A. Makarov, V. Sverdlov, and S. Selberherr. A Monte Carlo Simulation of Reproducible Hysteresis in RRAM. In *Proceedings of the 14th International Workshop on Computational Electronics (IWCE)*, pages 35–38, Pisa, Italy, 2010.
- [66] A. Makarov, V. Sverdlov, and S. Selberherr. A Stochastic Model of Bipolar Resistive Switching in Metal-Oxide-Based Memory. In *Proceedings of the 40th European Solid-State Device Research Conference (ESSDERC)*, pages 396–399, Sevilla, Spain, 2010.
- [67] A. Makarov, V. Sverdlov, and S. Selberherr. Modeling of Resistive Switching in RRAM Using Monte Carlo Simulations. In *Book of Abstracts: Workshop on Dielectrics in Microelectronics (WODIM)*, page 141, Bratislava, Slovakia, 2010.
- [68] A. Makarov, V. Sverdlov, and S. Selberherr. Modelling of the SET and RESET Process in Bipolar Resistive Oxide-Based Memory Using Monte Carlo Simulations. In *Abstracts of the International Conference on Numerical Methods and Applications (NM&A)*, pages B–39, Borovets, Bulgaria, 2010.
- [69] A. Makarov, V. Sverdlov, and S. Selberherr. Monte Carlo Simulation of Bipolar Resistive Switching Memories. In *Proceedings of the Nanoelectronics Days 2010*, page 22, Aachen, Germany, 2010.

- [70] A. Makarov, V. Sverdlov, and S. Selberherr. Stochastic Modeling Hysteresis and Resistive Switching in Bipolar Oxide-Based Memory. In *Proceedings of the 15th International Conference on Simulation of Semiconductor Processes and Devices (SISPAD)*, pages 237–240, Bologna, Italy, 2010.
- [71] A. Makarov, V. Sverdlov, and S. Selberherr. Stochastic Modeling of Bipolar Resistive Switching in Metal-Oxide Based Memory by Monte Carlo Technique. *Journal of Computational Electronics*, 9(3-4):146–152, 2010.
- [72] A. Makarov, V. Sverdlov, and S. Selberherr. Stochastic Modeling of the Resistive Switching Mechanism in Oxide-Based Memory. In *Proceedings of the 17th International Symposium on the Physics & Failure Analysis of Integrated Circuits (IPFA)*, pages 309–312, Singapore, 2010.
- [73] A. Makarov, J. Weinbub, V. Sverdlov, and S. Selberherr. First-Principles Modeling of Bipolar Resistive Switching in Metal-Oxide Based Memory. In *Proceedings of the 24th European Simulation and Modelling Conference (ESM)*, pages 181–186, Hasselt, Belgium, 2010.

Curriculum Vitae

Date of birth April 4th, 1985
Place of birth Volgograd, USSR (Russia)
Citizenship Russia

June 2002

High school graduation at the comprehensive secondary school (with honors)
Volzhsky, Russia

Sept. 2002

Enrolled at Volgograd State Technical University, Volgograd, Russia

June 2006

Received Bachelor degree in Computer Science (with honors) from the
Volgograd State Technical University, Volgograd, Russia

June 2008

Received Master's degree in Computer Science (with honors) from the
Volgograd State Technical University, Volgograd, Russia

since October 2009

Entered doctoral program at the Institute for Microelectronics,
Vienna University of Technology, Austria

July 2012

“Bursary award” at the Worldwide Universities Network 4th International Conference on Spintronics (WUN-SPIN 2012), Sydney, Australia

June 2013

“Outstanding student award” at the International Workshop on Computational Electronics (IWCE), Nara, Japan